DIRECTION FINDING AND POLARIZATION ESTIMATION, USING ELECTRICALLY LONG DIPOLES OR ELECTRICALLY LARGE LOOPS

SALMAN KHAN

Ph.D

The Hong Kong Polytechnic University

2018

The Hong Kong Polytechnic University

Department of Electronic and Information Engineering

Direction Finding and Polarization Estimation, Using Electrically Long Dipoles or Electrically Large Loops

Salman KHAN

A thesis submitted in partial fulfilment of the requirements for the degree of Doctor of Philosophy

February 2018

Certificate Of Originality

I hereby declare that this thesis is my own work and that, to the best of my knowledge and belief, it reproduces no material previously published or written, nor material that has been accepted for the award of any other degree or diploma, except where due acknowledgement has been made in the text.

______________________________ (Signed)

Salman KHAN ______________________________ (Name of Student)

Abstract

In antenna array signal-processing algorithm development, research has focused on electrically "short" dipoles with physical lengths (L) under $1/10$ of a wavelength λ. Such "short" dipoles have very small input impedances, rendering them to be poor radiators. Practical dipoles, with an electrical length of $\frac{L}{\lambda} \in [0.1, 1]$, have notably larger input impedances, hence making them better radiators. This thesis will first present the measurement model (i.e. array manifold) of such practical dipoles, as a triad that is collocated in space and orthogonal in orientation. Using such a triad to estimate incident sources' bivariate azimuth-elevation directions-of-arrival and bivariate polarizations, closed-form algorithms will be pioneered.

The triad's collocation gives a point-like spatial aperture, limiting the dipole-array's spatial resolution. To realize a large spatial aperture, electrically long dipoles can be positioned sparsely on a circular circumference, with each dipole oriented radially (or tangentially), to allow a rotational invariance with respect to the circle's origin. For such a circular array of sparsely spaced and differently oriented dipoles, this thesis will also develop the measurement model and will pioneer closed-form algorithms to estimate incident sources' bivariate azimuth-elevation directions-of-arrival and bivariate polarizations.

For two electrically long dipoles, this thesis also pioneers signal-processing algorithms in closed forms, to estimate the polarizations of impinging sources. This is unlike the vast literature on crossed-dipoles polarimetry, restricted to electrically short dipoles. In this thesis, the two long dipoles are perpendicularly oriented, but may be collocated or may be separated by a known displacement. Using such a pair of electrically long dipoles for polarization estimation, this thesis proposes new closed-form formulas, and derives the associated Cramér-Rao bounds.

Besides electrically long dipoles, electrically "large" loops with circumference ($2\pi R$) over $1/10$ of a wavelength λ have likewise been neglected in the literature on antenna signal processing. This thesis will formulate the array manifold for a triad of electrically "large" loops, collocated and orthogonal. Then for such a triad of large loops, this thesis will pioneer closed-form signal processing algorithms to estimate the incident signals azimuth-elevation directions-of-arrival and polarizations.

List of Publications

Journal papers: (published/accepted)

1. S. Khan, K. T. Wong, Y. Song and W. Y. Tam, “Electrically large circular loops in the estimation of an incident emitter’s direction-of-arrival or polarization,” *IEEE Transactions on Antennas and Propagation*, vol. 66, no. 6, pp. 3046-3055, June 2018.

2. K. T. Wong, Y. Song, C. J. Fulton, S. Khan, and W. Y. Tam, “Electrically “long” dipoles in a collocated/orthogonal triad – for direction finding and polarization estimation,” *IEEE Transactions on Antennas and Propagation*, vol. 65, no. 11, pp. 6057-6067, Nov. 2017.

Journal papers: (under peer review)

3. S. Khan and K. T. Wong, “Electrically long dipoles in a crossed pair for closed-form estimation of an incident source’s polarization”, under review by the *IEEE Transactions on Antennas and Propagation*.

4. K. T. Wong, Y. I. Wu, G. P. Arada, W.-Y. Tam, S. Khan, and C. J. Fulton, “How two crossed dipoles’ self/mutual impedance varies with their non-orthogonality, length & separation”, under review by the *IEEE Transactions on Antennas and Propagation*.

Conference presentation:

1. Y. Song, K. Wong, S. Khan, and M. Khan, “Azimuth-elevation direction finding, using three uni-axial velocity sensors as an arbitrarily sparse linear array”, presented at *175th meeting of the Acoustical Society of America*, Minneapolis, Minnesota, USA, May 2018.

Acknowledgement

I am grateful to Almighty Allah for giving me strength and ability to continue this course of study.

I would like to express my sincere gratitude to my honorable advisor Professor Kainam Thomas Wong for his continuous support throughout my PhD study and related research, for his patience, motivation, and immense knowledge. His guidance helped me in conducting the research and writing of this thesis. I could not have imagined having a better advisor and mentor for my PhD study. Professor Wong dedicated a lot of his precious time to nurture my academic knowledge and intellectual ability with patience. Besides the study, Professor Wong has given me a lot of moral support to overcome all the difficulties I faced during my entire study period.

Besides my advisor, I would like to thank my co-advisor Dr. Wai-Yip Tam for his admirable guidance. I would also like to express my sincere appreciation and gratitude to all faculty members of the Department of Electronic and Information Engineering who shared their wide knowledge and wisdom with me throughout my PhD study.

I am also thankful to Professor Caleb J. Fulton for his valuable time and intellectual suggestions in explaining the behavior of various antenna configurations.

I thank my fellow labmates for the stimulating discussions. I also thank my friends in the Hong Kong Polytechnic University.

Last but not the least, I would like to thank my family: my parents, my fiancée, and my brothers and sisters for supporting me spiritually throughout writing this thesis and my life in general.

Table of Contents

List of Figures

List of Tables

1 Introduction

This thesis is composed of four research projects, undertaken during my doctorate study. These projects describe new methods for the estimation of Direction-of-Arrival (DoA) and/or polarization of the signals impinging upon different configurations of electrically long dipoles or electrically large loops.

1.1 Motivation

1.1.1 Direction-of-Arrival Estimation

Information on direction-of-arrival can be quite useful in mobile communications, radar, and localization. In mobile communication systems, there is an increased demand of higher data rate and mobile communication services. Frequency reuse concept as shown pictorially in Figure 1.1 was designed to re-use the available spectrum multiple times to enhance the capacity [1]. The total capacity C of such a cellular system is given by

$$C = MS \tag{1.1}$$

where M denotes replication of the cluster which is combination of cells where whole spectrum is used once and S denotes the total number of available channels within a cluster. If the cluster size is reduced keeping the same cell size, then the capacity would increase as more number of clusters would be required to provide coverage. However, different types of interference would increase as a result of reduction in cluster size. There is a lower limit beyond which the cluster size cannot be further reduced to simultaneously achieve optimum performance.

Spatial filtering and beamforming at the base station is presented as a solution to reduce the lower limit of cluster size and achieve optimum performance at the same time [2]. Spatial filtering is performed to isolate desired signal from other interfering signals [3] and beamforming is the

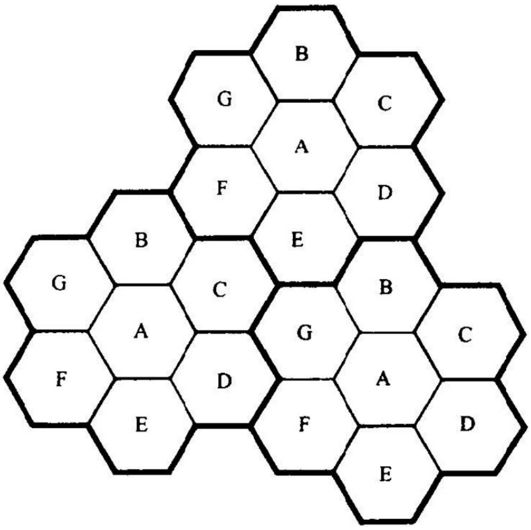

Fig. 1.1.: Graphical demonstration of frequency reuse [1].

array processing to direct independent beams toward different mobile stations [2], [4]. Both spatial filtering and beamforming require information on direction-of-arrival of signals received from mobile stations making direction finding important in significantly mitigating interferences and achieving higher capacity in mobile communication systems. In some other applications of wireless communication, it maybe useful for both the transmitter and receiver to share the knowledge of their respective positions for which estimation of the arrival angles become important [5].

Direction-of-arrival estimation is a primary feature of smart antennas which can provide increased robustness against multipath, higher signal-to-noise ratio, and enhanced system capacity in wireless communications [6, 123]. Mobile multi-hop relay systems have also received increased attention for their better quality of service over large coverage area with higher signal-to-noise ratio, reduced interference, and hence enhanced system capacity. The mobile multi-hop relay system in turn requires the direction-of-arrival estimation for beamforming [7].

Channel characterization can also be performed in mobile communication systems using direction-of-arrival estimation. A transmitted signal normally arrives at the receiver after getting reflected through multiple paths. Estimated angle of arrival and time of arrival statistics of different multipaths can provide useful information about multipath radio channel [8].

Direction of arrival estimation is also very useful in telemedicine systems [10]. In hospitals or sanitarium, body sensors can be implanted on patients which can send the signal through mobile device in case of emergency conditions such as high blood pressure or heart attack. The direction-of-arrival estimation can become very useful in exactly locating the patient to reduce the rescue time. Such wearable sensor devices can also help constantly monitoring and localizing population group with high risks, e.g. elderly people, who may suffer from abnormality or involuntary falls any time.

Real-time monitoring of inventory and identification of asset are also possible with the aid of direction-of-arrival estimation [9]. Direction finding is also quite important in defense radars. It can be used to determine the angle of arrival of an aircraft or a missile. In radar, generally a known signal is transmitted by an antenna which after reflection from the target gets received by an array of antennas as shown in Figure 1.2. The received signal is processed for direction finding to locate the target. The location of radar can also be determined at the target side. That is, the target can estimate location of the radar from direction finding of the received signal sent by radar to encounter them.

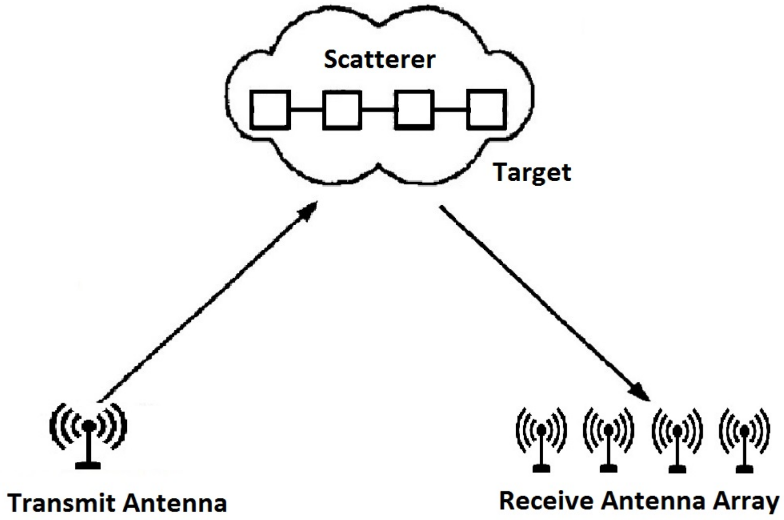

Fig. 1.2.: Signal received by an array of antennas after reflection from target.

1.1.2 Polarization Estimation

Polarization is the property of a wave which shows trace of the electric field vector. The measurement and interpretation of polarization is called as polarimetry. As there is an increased demand of higher data rate in telecommunication networks where the spectrum is limited, different solutions are presented to mitigate this issue. Polarization diversity is regarded as one solution in providing higher data rate with limited available spectrum [11], [12]. That is, two signals at a certain frequency sent with different polarizations can be distinguished from each other and hence can effectively double up the available spectrum.

Polarimetry can also be utilized in post-processing of wave in radar to provide details about structure of the target [13]. A signal when transmitted by the radar is having a known polarization. After reflection from the target, its polarization can be compared with that of the transmitted signal which can reveal important features about details of the target.

Polarimetry is also performed in weather radars which can be useful in weather forecasting. Such radars can detect rain and hail/snow by transmitting a radio wave and receiving it back after reflection from water particles present in clouds. Polarization information of transmitted and received waves can reveal information about whether the wave got reflected from rain, hail, or snow and also it can estimate water drop shape and size. The time taken between one round trip of a radio wave between transmission and reception can be used to measure the distance of the clouds. Precipitation in the clouds can also be determined from the received energy. Polarimetry is also used in other remote sensing applications like astronomy and planetary science.

The best known parameter estimation techniques, though not exhaustive, are categorized in [14] and discussed briefly in the following sub-sections.

Spectral-based Methods

Consider the case of direction finding, a spectral-like function is made in these methods and the points at which the maximum peaks of the function lie show the estimated directions-of-arrival. The location of the peaks must be separated enough from each other in order to perform estimation correctly. That is, there is a lower bound on the resolution that can be achieved with the spectral-based methods which further depends on the methodology adopted. These methods can further be categorized into two methods. The first one is probably the oldest method used to determine the directions-of-arrival called as beamforming techniques where as the second one is known as subspace-based methods [14].

1 *Beamforming Techniques*

In beamforming techniques, the radiation pattern of an antenna array with narrow beamwidth and hence more gain in a specific direction is developed. Furthermore, the direction of the main beam can be controlled and moved across the space by providing a phase difference between the elements of the array. If the main beam is directed towards the source, then maximum power is received and vice versa. Therefore, the main beam can be steered across the space to look for the maximum received power and the locations of the maximum power are considered as the directions-of-arrival [14]. This idea is implemented in a variety of ways where the well known methods are Barlett Beamformer [15] and Capon's Beamformer [16].

2 *Subspace-Based Methods*

Different subspace-based methods are briefly introduced as following.

a. *MUSIC Algorithm*

Multiple signal classification algorithm, which in short is called as MUSIC algorithm, is a very well known eigenstructure approach to locate signals with high resolution capability developed first by Schmidt [17]. The drawback of MUSIC is to resolve coherent signals.

b. *Improvement to MUSIC Algorithm*

Different variants of the MUSIC algorithm have been chalked out to improve its capabilities. Root-MUSIC [18] and Cyclic MUSIC [19] are amongst the more popular improvements to MUSIC algorithm.

c. *ESPRIT*

Estimation of Signal Parameters via Rotational Invariance Techniques, ESPRIT, uses the rotational invariance which is generated in the signal subspace by two identical arrays [20]. The two identical arrays are made such that each element in first array makes a pair with the corresponding element in the second array such that there is a constant displacement in the same direction with respect to the first element for each pair. Based on how the criteria is achieved, many versions of ESPRIT algorithm have been developed including Least-Square-Sense-ESPRIT and Total-Least-Square-ESPRIT [21]

Maximum Likelihood Method

Again consider direction finding, maxima of the log-likelihood function are determined in these methods from the data collected by the antenna array which give the estimated directions-of-arrival. The log-likelihood function is basically the sampled data's joint probability density function provided the directions-of-arrival and observed as a function of the directions-of-arrival. For estimation, directions are searched which give the maximum of the log-likelihood function and these values signify that these directions are most likely to be the reason to generate such sampled data [22,23].

Electrically short/small [1] dipoles and loops are quite often used for direction finding and polarization-estimation. If such a dipole is aligned in parallel with any Cartesian axis, it would provide value of electric-field vector component in that direction. Similarly if a loop axis gets aligned with any Cartesian axis, it would measure the corresponding magnetic-field

---

[1] Dipole with overall length smaller than one-tenth of a wavelength is considered as short dipole, loop with circumference smaller than one-tenth of a wavelength is regarded as small loop

vector component along that direction. These concepts are reviewed in next section.

1.2 Review of Electric and Magnetic Field Vectors

Figure 1.3 graphically defines various spatial angles for the exposition in following Chapters:

1. $\theta_x \in [0, \pi]$ is the angle measured between the propagation vector $\mathbf{r}$ and the positive x-axis,
2. $\theta_y \in [0, \pi]$ is the angle measured between the propagation vector $\mathbf{r}$ and the positive y-axis,
3. $\theta_z = \theta \in [0, \pi]$ is the (polar) angle measured between the propagation vector $\mathbf{r}$ and the positive z-axis,
4. $\phi_y \in [-\pi, \pi)$ is the angle measured between projection of the propagation vector $\mathbf{r}$ onto the y-o-z plane and the positive y-axis,
5. $\phi_z \in [-\pi, \pi)$ is the angle measured between projection of the propagation vector $\mathbf{r}$ on the x-o-z plane and the positive z-axis, and
6. $\phi_x = \phi \in [-\pi, \pi)$ is the (azimuth) angle measured between projection of the propagation vector $\mathbf{r}$ on the x-o-y plane and the positive x-axis.

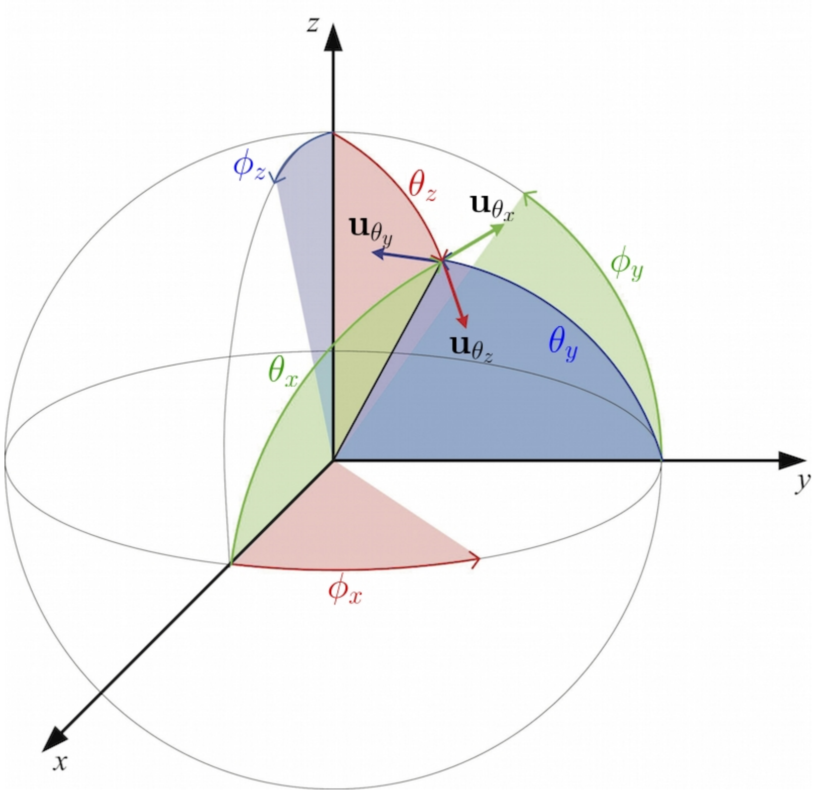

Fig. 1.3.: Different spatial angles inter-relationship.

The above angles are interrelated through the following trigonometric relationships:

$$\sin(\theta_x) = \sqrt{\sin^2(\theta_z)\sin^2(\phi_x) + \cos^2(\theta_z)}$$

$$\cos(\theta_x) = \sin(\theta_z)\cos(\phi_x)$$

$$\sin(\theta_y) = \sqrt{\sin^2(\theta_z)\cos^2(\phi_x) + \cos^2(\theta_z)}$$

$$\cos(\theta_y) = \sin(\theta_z)\sin(\phi_x)$$

$$\sin(\phi_y) = \frac{\cos(\theta_z)}{\sqrt{\sin^2(\theta_z)\sin^2(\phi_x) + \cos^2(\theta_z)}}$$

$$
\begin{aligned}
\cos(\phi_y) &= \frac{\sin(\theta_z)\sin(\phi_x)}{\sqrt{\sin^2(\theta_z)\sin^2(\phi_x)+\cos^2(\theta_z)}} \\
\sin(\phi_z) &= \frac{\sin(\theta_z)\cos(\phi_x)}{\sqrt{\sin^2(\theta_z)\cos^2(\phi_x)+\cos^2(\theta_z)}} \\
\cos(\phi_z) &= \frac{\cos(\theta_z)}{\sqrt{\sin^2(\theta_z)\cos^2(\phi_x)+\cos^2(\theta_z)}}.
\end{aligned}
$$

Furthermore, define the unit vector ($\mathbf{u}_{\theta_x}$, $\mathbf{u}_{\theta_y}$, $\mathbf{u}_{\theta_z}$, $\mathbf{u}_{\phi_x}$, $\mathbf{u}_{\phi_y}$, $\mathbf{u}_{\phi_z}$) along the (θ_x, θ_y, θ_z, ϕ_x, ϕ_y, ϕ_z) direction as follows:

$$\mathbf{u}_{\theta_x} := [\ -\sin(\theta_x),\ \cos(\theta_x)\cos(\phi_y),\ \cos(\theta_x)\sin(\phi_y)]^T \tag{1.2}$$

$$\mathbf{u}_{\theta_y} := [\ \cos(\theta_y)\sin(\phi_z),\ -\sin(\theta_y),\ \cos(\theta_y)\cos(\phi_z)]^T \tag{1.3}$$

$$\mathbf{u}_{\theta_z} := [\ \cos(\theta_z)\cos(\phi_x),\ \cos(\theta_z)\sin(\phi_x),\ -\sin(\theta_z)]^T \tag{1.4}$$

$$\mathbf{u}_{\phi_x} := [\ -\sin(\phi_x),\ \cos(\phi_x),\ 0]^T. \tag{1.5}$$

$$\mathbf{u}_{\phi_y} := [\ 0,\ -\sin(\phi_y),\ \cos(\phi_y)]^T \tag{1.6}$$

$$\mathbf{u}_{\phi_z} := [\ \cos(\phi_z),\ 0,\ -\sin(\phi_z)]^T \tag{1.7}$$

In the above, the superscript ^{T} refers to transposition.

Keeping in mind the spatial coordinates defined in Figure 1.3, consider a plane wave of unit power per unit area , incident upon the Cartesian origin from a polar angle (a.k.a. a zenith angle) of $\theta_z \in [0, \pi]$ and an azimuth angle of $\phi_x \in [0, 2\pi)$, with an auxiliary polarization angle of $\gamma \in [0, \pi/2)$ and a polarization phase difference of $\eta \in [-\pi, \pi)$. This electromagnetic wavefield thus has

(i) a component of $e_{\phi_x}\mathbf{u}_{\phi_x}$ with amplitude $e_{\phi_x} = \cos(\gamma)$ along the horizontal transverse axis $\mathbf{u}_{\phi_x}$, and

(ii) a component of $e_\theta \mathbf{u}_{\theta_z}$ with complex-value amplitude $e_\theta = e^{j\eta}\sin(\gamma)$ along the vertical transverse axis $\mathbf{u}_{\theta_z}$.

In Cartesian coordinates, this electric-field vector e may be represented as

$$\begin{aligned}
\mathbf{e} &= e_x \overbrace{\begin{bmatrix} 1 \\ 0 \\ 0 \end{bmatrix}}^{\mathbf{u}_x :=} + e_y \overbrace{\begin{bmatrix} 0 \\ 1 \\ 0 \end{bmatrix}}^{\mathbf{u}_y :=} + e_z \overbrace{\begin{bmatrix} 0 \\ 0 \\ 1 \end{bmatrix}}^{\mathbf{u}_z :=} = \begin{bmatrix} e_x \\ e_y \\ e_z \end{bmatrix} \\
&= \underbrace{\sin(\gamma)e^{j\eta}}_{e_{\theta_z}=} \overbrace{\begin{bmatrix} \cos(\phi_x)\cos(\theta_z) \\ \sin(\phi_x)\cos(\theta_z) \\ -\sin(\theta_z) \end{bmatrix}}^{\mathbf{u}_{\theta_z} :=} + \underbrace{\cos(\gamma)}_{e_{\phi_x}=} \overbrace{\begin{bmatrix} -\sin(\phi_x) \\ \cos(\phi_x) \\ 0 \end{bmatrix}}^{\mathbf{u}_{\phi_x} :=} \\
&= \begin{bmatrix} \cos(\phi_x)\cos(\theta_z) & -\sin(\phi_x) \\ \sin(\phi_x)\cos(\theta_z) & \cos(\phi_x) \\ -\sin(\theta_z) & 0 \end{bmatrix} \begin{bmatrix} e_{\theta_z} \\ e_{\phi_x} \end{bmatrix}. \qquad (1.8)
\end{aligned}$$

In the above, the unit vectors $\mathbf{u}_x, \mathbf{u}_y$ and $\mathbf{u}_z$ point along x, y, and z-axes, respectively, of the Cartesian coordinate system. If a triad of short dipoles orthogonally oriented and spatially collocated is placed at Cartesian origin, then each dipole in the triad would measure component of electric-field vector along that dipole.

Similarly a fully polarized transverse electromagnetic wave has a 3×1 normalized magnetic-field vector,

$$\begin{aligned}
\mathbf{h} &= \begin{bmatrix} h_x \\ h_y \\ h_z \end{bmatrix} = \begin{bmatrix} -\sin(\phi_x) & -\cos(\phi_x)\cos(\theta_z) \\ \cos(\phi_x) & -\sin(\phi_x)\cos(\theta_z) \\ 0 & \sin(\theta_z) \end{bmatrix} \begin{bmatrix} e_{\theta_z} \\ e_{\phi_x} \end{bmatrix}, \\
&\overset{\text{def}}{=} \begin{bmatrix} -\sin(\phi_x) & -\cos(\phi_x)\cos(\theta_z) \\ \cos(\phi_x) & -\sin(\phi_x)\cos(\theta_z) \\ 0 & \sin(\theta_z) \end{bmatrix} \begin{bmatrix} \sin(\gamma)\, e^{j\eta} \\ \cos(\gamma) \end{bmatrix}, \qquad (1.9)
\end{aligned}$$

Likewise if a triad of small loops orthogonally oriented and spatially collocated in a point-like geometry is placed, then each loop in the triad would measure component of the magnetic-field vector along axis of that loop.

However, it should be noted that such “short" dipoles and “small” loops are very poor radiators and receptors because of their small input impedances. There is a need to develop estimators for “long” dipoles and “large” loops for pragmatic use with practical dipoles and loops of effective radiation efficiencies.

1.3 Eigen-based Parameter Estimation

Recall that the Cramér-Rao bound lower-bounds the estimation error variance of any unbiased estimator; and the Cramér-Rao bound itself is independent of the specific estimator employed. The maximum-likelihood estimator can reach the Cramér-Rao lower bound. However, the maximum-likelihood estimator

(i) would require a perfect prior knowledge of the signal-and-noise statistics, and

(ii) would require the iterative optimization of a likelihood function, hence

  (ii-a) would be computationally intensive, and

  (ii-b) would presume the availability of a good estimate (which is often unavailable) to direct the iteration to converge toward the global optimum.

Hence, this thesis will develop eigen-based estimators, using non-small dipole/loops, that are non-iterative and that need no prior knowledge of any signal-and-noise statistics. In most eigen-based estimation algorithms, an intermediate step determines the sources' steering vector $\mathbf{a}$ multiplied by a complex-scalar c which is unknown. In other words, the intermediate step provides an estimate $\hat{\mathbf{a}} \approx c\mathbf{a}$ [62].

Imagine a signal $s(t)$ is received by an N elements antenna array which is corrupted by an additive thermal noise vector $\mathbf{n}(t)$. The data collected by the array at every sample time $t = t_m$ can therefore be written as

$$\mathbf{z}(t) = s(t)\mathbf{a} + \mathbf{n}(t). \tag{1.10}$$

If we consider a simple example where the random processes $s(t)$ and $\mathbf{n}(t)$ are each zero-mean complex-value Gaussian and spatio-temporally uncorrelated over time and across antennas, while statistically independent from all other entities. Then it can be found that the data covariance matrix of all M time-samples collected by the triad can be written as

$$\begin{aligned}\hat{\mathbf{C}} &= \frac{1}{M}\sum_{m=1}^{M}\mathbf{z}(t_m)[\mathbf{z}(t_m)]^H \quad (1.11)\\ &\approx \sigma_s^2\mathbf{a}\mathbf{a}^H + \sigma_n^2\mathbf{I}_N. \quad (1.12)\end{aligned}$$

where σ_s^2 denotes the incident signal power and σ_n^2 refers to antenna thermal noise power and $\mathbf{I}_N$ denotes an identity matrix of order $N \times N$. This data covariance matrix $\hat{\mathbf{C}}$ has a principal eigenvector which approximately equates to $c\mathbf{a}$ and this approximation asymptotically becomes equality in the noiseless case or as $M \to \infty$. To sum up, sample-data covariance matrix has a principal eigenvector which is approximately equal to $c\mathbf{a}$ from which closed-form estimators for estimation of direction-of-arrival and polarization can be developed.

Literature Review

2

2.1 Dipole and Loop Triads

Direction finding and polarization estimation are of practical importance in a variety of systems including radars, sensor networks, mobile communications, and target localization. For simultaneous eigen-based estimation of the polarization and direction-of-arrival, at least three antennas of diverse polarizations are required, because a minimum of three complex-value equations (resulting from measurement of three antennas) are required for the solution of five unknown parameters (i.e., $\gamma, \eta, \theta_z, \phi_x, c$) where γ, η are related to polarization, θ_z, ϕ_x are polar-azimuth direction-of-arrival parameters, and complex-value c results from eigen-based source's steering vector estimation. It can be versatile and convenient to use a triad of dipoles (a.k.a. a "tripole") or a triad of loops. The three constituent dipoles or loops would be identical, orthogonally oriented among themselves, and spatially co-centered. Such a triad offers notable advantages:

(i) polarization diversity – incident signals may be resolved by the receiver on account of their distinct polarizations, in addition to their different arrival directions;

(ii) decoupling the incident signal's frequency dimension from the signal's azimuth-elevation directional dimensions, because no spatial phase factor exists across the triad's constituent dipoles.

Advantages (i)-(ii) mentioned above have motivated many innovative signal processing algorithms in recent decades for direction finding and polarization estimation using either a dipole triad or a loop triad. They can classified into closed-form and open-form estimators where the former have following advantages over the latter:

1. Generally computationally simpler.

2. Avoid problem of iterations converging to a local optimum, instead of the global optimum.

3. Avoid the need of an initial estimate to start off the iteration

A brief summary of these algorithms using such triads of “short” dipoles or “small” loops, illustrated in detail in [62], is presented here.

1. Dipole triad has been used for both closed-form and open-form direction-of-arrival estimation [24–34,36,37,39–41,141,144]. Among these references, only [28, 37, 40] presented closed-form estimation formulas. The tripole has also been utilized for closed-form polarization estimation in [28, 37]. For the dipole triad, Cramér-Rao bound expressions in closed-form are presented in [43]. Such a tripole is also used experimentally in [32].

2. Similarly both closed-form and open-form direction-of-arrival estimation using loop triad can be found in [28, 37, 42, 141] where only [28, 37] presented closed-form estimation formulas. Closed-form polarization estimation formulas are also established using loop triad in [28, 37]. For the loop triad, Cramér-Rao bound expressions in closed-form are presented in [43]. Such a triad is experimentally used in [42].

Nonetheless, this open literature of signal-processing algorithm development has focused on “short" dipoles (i.e., dipoles with physical lengths (L) under about a tenth of a wavelength λ) and “small” loops (i.e., loops with physical circumference ($2\pi R$) under about one tenth of a wavelength). However, it should be noted that both “short" dipole and “small” loop have input impedances that are very small, rendering them poor radiators.

“Long" dipoles also have had *open*-form or *iterative* algorithms designed for their use in direction finding in [50, 51, 56], but there only as a linear array of uniformly displaced of antennas in identical orientation.[1] In contrast, this thesis offers *closed*-form algorithms, for a collocated triad of orthogonal oriented “long" dipoles, to estimate the polar-azimuth bivariate direction-of-arrival or the bivariate polarization. For such a triad of “long”

---

[1] For such a linear array of identically oriented “long" dipoles, the direction finding’s Cramér-Rao bound is plotted in [50, 51, 56, 61].

dipoles, [58] discusses its steering vectors' linear independence but offers no estimation algorithm. On the other hand, [59] proposes an *open*-form *iterative* algorithm for polarization estimation and not for direction finding where *closed*-form are presented here for both polarization estimation and direction finding.

For the case of "large" loop triad, this thesis is first to the best of knowledge to present *closed*-form polarization estimation and direction finding algorithms.

2.2 Uniform Circular Array of Dipoles

Dipole arrays have been much studied for direction finding and polarization estimation. The antennas can either be collocated or spatially separated where the former is limited by a point-like spatial aperture, which leads to low spatial resolution over the azimuth-elevation dimensions.

Both the collocated and spatially separated direction finding literature is much investigated which are briefly described here.

1. Collocated dipoles has been studied thoroughly in literature, however, the focus has been on "electrically short" dipoles, i.e. dipoles with a physical length (L) under a tenth of a wavelength — strangely so, because such "short dipoles" are *in*efficient electromagnetic radiators. For example, see [125–152]. For a practical electromagnetic efficiency for electromagnetic reception, real-world dipoles should be "electrically long" – i.e. with $\frac{L}{\lambda} \in \left[\frac{1}{10}, 1\right]$.

   Electrically long dipole signal processing is for the first time investigated in Chapter 3. Nonetheless, that pioneering investigation focuses exclusively on a *spatially co-centered* unit of "electrically long" dipoles in orthogonal orientation relative to each other.

2. Similarly the extended-aperture sensor-array direction-finding literature is vast, but (unlike the present investigation of uniform circular array of electrically long dipoles in this thesis) that literature is almost always limited to:

  - (a) short dipoles, e.g., see [99–102, 105–110, 125], or
  - (b) electrically long dipoles that are all identically oriented, for example, [103, 104, 111–124].

For this thesis to achieve *closed*-form direction finding with an extended aperture, despite the diverse orientation of the dipoles that are electrically long – this achievement is unprecedented in the open literature (to the best of knowledge).

2.3 Dipole-Dipole Pair

Polarimetry measures and interprets the polarization of transverse waves [94]. Two antennas of diverse polarizations would suffice to estimate bivariate polarization of a fully polarized wave using eigen-based estimation because a minimum of two complex-value equations are required for the solution of three unknown parameters (γ, η, c) which can be obtained from the measurement of two antennas.

Polarimetry via orthogonally oriented electric dipoles – this has been much investigated. Please refer to [62, 93, 125] for surveys of this literature. A brief description of the use of dipole-dipole pair is presented here.

1. For orthogonal dipole-dipole pair, either both the antennas would lie horizontally or one of the antenna would be horizontal and the other one vertical.
   - (a) [11-13, 18, 25, 26, 28, 31, 38, 45, 64, 66, 78, 108, 122, 125, 126, 129, 138, 142, 152, 157, 159] investigated the case of dipole-dipole pair orthogonal to each other and lying horizontally and used for direction finding and/or polarization estimation.
   - (b) Similarly [35, 54, 55, 70, 115, 130, 158] investigated the case where one dipole is vertical and one dipole horizontal and used for direction finding and/or polarization estimation.

2. Likewise, other dipole-pairs with different but orthogonal orientations are investigated in [16, 19, 22, 39, 67, 70, 92, 148, 166].

3. Dipole-pair have also been tested experimentally in [84, 90, 121, 139, 140, 149, 160].

These references, however, focus on electrically short dipoles, which are inefficient antennas. At an electrical length of $\frac{L}{\lambda} = \frac{1}{10}$, an electrically short dipole's radiation efficiency is only 74%, whereas an electrically long half-wavelength dipole offers 95%.[2] For a perpendicular pair of such electrically long dipoles, this thesis is first (to the present authors' best knowledge) to advance any closed-form formula to estimate an incident wavefield's polarization.

2.4 Thesis Structure

This thesis is organized as following:

Chapter 3

In this chapter, *closed*-form algorithms for estimation of polar-azimuth bivariate direction-of-arrival and the bivariate polarization are presented using electrically "long" dipoles triad.

Chapter 4

Similar to Chapter 3, *closed*-form algorithms for estimation of polar-azimuth bivariate direction-of-arrival and the bivariate polarization are presented here but using uniform circular array of electrically "long" dipoles which may be oriented radially or tangentially.

Chapter 5

This chapter advances *closed*-form algorithms for estimation of bivariate po-

---

[2] These values are computed based on the radiation resistance equations and the loss resistance equations in [68, pp. 86, 177, 215], [95].

larization using a pair of orthogonally oriented but not necessarily spatially collocated electrically “long” dipoles.

Chapter 6

Similarly, *closed*-form algorithms for estimation of polar-azimuth bivariate direction-of-arrival and the bivariate polarization are presented here using electrically “large” loops triad.

Chapter 7

In the last, conclusions are drawn.

3

Electrically “Long" Dipoles in a Collocated/Orthogonal Triad – for Direction Finding and Polarization Estimation

3.1 Introduction

For a wireless receiver to estimate an incident emitter’s azimuth-elevation direction-of-arrival (DOA) and/or polarization, it can be versatile and convenient to use a triad of dipoles (a.k.a. a “tripole"). The three constituent dipoles would be identical, orthogonally oriented among themselves, and spatially co-centered as shown in Figure 3.1. Such a tripole offers notable advantages:

(i) polarization diversity – incident signals may be resolved by the receiver on account of their distinct polarizations, in addition to their different arrival directions;

(ii) decoupling the incident signal’s frequency dimension from the signal’s azimuth-elevation directional dimensions, because no spatial phase factor exists across the triad’s constituent dipoles.[1]

Advantages (i)-(ii) have motivated many innovative signal processing algorithms in recent decades for direction finding and polarization estimation, e.g. see the survey in Section I-1) of [62].

---

[1] This frequency-versus-direction decoupling is evidently advantageous, by considering this simply numerical example with N_F discrete-Fourier-transform (DFT) frequency-bins (i.e., DFT-frequency grid points), N_D distance-bins, and N_{DOA} azimuth-elevation angular bins. If these frequency-azimuth-elevation dimensions were coupled, the antenna-arrayÂŠs “array manifold" would be $N_F \times N_D \times N_{\text{DOA}}$ in size. If *un*coupled, this size shrinks to $N_F + N_D + N_{\text{DOA}}$. For $N_F = N_D = N_{\text{DOA}} = 1000$, this represents a reduction of $109/103/3 = 333,333$ folds in computation.

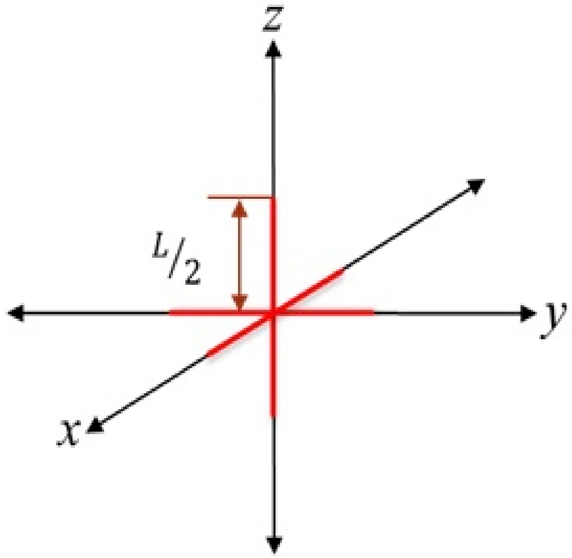

Fig. 3.1.: Collocated and orthogonally oriented dipole triad.

Nonetheless, this open literature of signal-processing algorithm development has focused on “short" dipoles (i.e., dipoles with physical lengths (L) under about a tenth of a wavelength λ). However, such a “short" dipole has an input impedance that is very small, rendering the “short" dipole an inefficient radiator. [2]On the other hand, very long dipoles with $L > \lambda$ would have sidelobe(s), hence seldom used in practice. Rather, practical dipoles typically have $L \leq \lambda$, such that the radiation pattern is like the character “8" in the polar coordinates with only one mainlobe but no sidelobe. All the above considerations together mean that the “electrical length" (a.k.a. “phase length") $\frac{L}{\lambda}$ of practical interest lies within the range of $[0.1, 1]$, in order to achieve radiation efficiency and to avoid sidelobes, simultaneously. This Chapter will investigate such “long" dipoles’ use for azimuth-elevation direction finding and for polarization estimation, when they are configured as a triad in spatial collocation but orthogonal orientation.

“Long" dipoles have had *open*-form or *iterative* algorithms designed for their use in direction finding in [50, 51, 56], but there only as a linear array

---

[2] As a dipole’s physical length $\frac{L}{\lambda}$ increases from $\frac{1}{100}$ to $\frac{1}{10}$ and then to $\frac{1}{2}$, the dipole’s corresponding radiation efficiency would improve from 36% to 74% and then to 95%. These numbers are calculated using the radiation resistance equations and the loss resistance equations in [68, pp. 86, 177, 215], [95].

of uniformly displaced of antennas in identical orientation.[3] In contrast, this present Chapter offers *closed*-form algorithms, for a collocated triad of orthogonal oriented “long" dipoles, to estimate the polar-azimuth bivariate direction-of-arrival and/or the bivariate polarization. Of such a triad: [58] discusses its steering vectors’ linear independence but offers no estimation algorithm; and [59] proposes an *open*-form *iterative* algorithm (not in *closed*-form as in this Chapter) for polarization estimation (not also for direction finding as in this Chapter).

Section 3.2 will review the concept of “effective length" to relate a “long" dipole’s directional-polarizational pattern to the incident electric field. Section 3.3 will then present the measurement model of a triad of collocated orthogonal “long" dipoles. Sections 3.4-3.5 will advance new closed-form algorithms to use such a triad to estimate any incident emitter’s azimuth-elevation direction and/or polarization. Section 3.6 will conclude this work.

3.2 The “Effective Length" of a Dipole Antenna

Keeping in mind the spatial coordinates defined in Section 1.2 of Chapter 1, consider a plane wave of unit power per unit area [4], incident upon the Cartesian origin from a polar angle (a.k.a. a zenith angle) of $\theta_z \in [0,\pi]$ and an azimuth angle of $\phi_x \in [0,2\pi)$, with an auxiliary polarization angle of $\gamma \in [0,\pi/2)$ and a polarization phase difference of $\eta \in [-\pi,\pi)$. The electric field for such a wave is given by equation (1.8). Suppose this electromagnetic wave impinges upon a center-driven dipole antenna of physical length L at a polar angle of θ with the dipole antenna’s axis. The dipole antenna’s open-circuit voltage would equal

$$v \quad = \quad \mathbf{e}\cdot\boldsymbol{\ell}_{\theta}^{(L)}, \tag{3.1}$$

---

[3] For such a linear array of identically oriented “long" dipoles, the direction finding’s Cramér-Rao bound is plotted in [50, 51, 56, 61].

[4] The definitions here are consistent with the notion of a “unit power per unit area" in the electromagnetic wave, if a) the units of electric field are volts per meter, b) a unit area is one square meter, and c) the free space impedance is normalized to 1 ohm.

where the vector $\boldsymbol{\ell}_\theta^{(L)}$ denotes the antenna's “effective length" (a.k.a the “effective height"). Please see equation (4-20) of [46], or equation (2-93) of [68]. Suppose the dipole has an electrical length $\frac{L}{\lambda} < 1$ and not near unity, then [5]

$$\boldsymbol{\ell}_\theta^{(L)} = \overbrace{-\frac{\lambda}{\pi}\frac{1}{\sin\left(\pi\frac{L}{\lambda}\right)}\frac{\cos\left(\pi\frac{L}{\lambda}\cos(\theta)\right)-\cos\left(\pi\frac{L}{\lambda}\right)}{\sin(\theta)}}^{\ell_\theta^{(L)} :=}\mathbf{u}_\theta. \tag{3.2}$$

If the dipole antenna is oriented along the x-axis, set $\theta = \theta_x$ everywhere in (3.2) including in the subscripts, and similarly for the y-axis and the z-axis.

The scalar $\ell_\theta^{(L)}$ varies with the dipole's *physical* length L through the cosine function; hence, the effective length varies *non*-monotonically with the physical length L. This “effective length" expression, however, would break down for any $\frac{L}{\lambda}$ near an integer, as the expression would stipulate a current null at the feed point, which is not the case in actuality. In physical reality, the current null there is relatively low, but not zero.

The “effective length" varies with θ, hence depends on the incident emitter's direction-of-arrival. Within the range of $\frac{L}{\lambda} \in [10^{-2}, 1]$, a peak exists at $\theta = \frac{\pi}{2}$ and troughs exist at $\theta = 0, \pi$ in (3.2). Inside the trigonometric functions, L and λ always appear together as a ratio, $\frac{L}{\lambda}$, a geometric factor to shape the “long" dipole's radiation pattern. The leading λ factor in (3.2) scales the “long" dipole's overall sensitivity. Though the “effective length" has a unit of length, the “effective length" is not a “length" per se, but a “pattern" to be multiplied to the incident electric field to produce the antenna's voltage.

The scalar of $\ell_\theta^{(L)}$ could be positive, negative, or zero. The leading negative sign in (3.2) may be overlooked with no change in any subsequent analysis, because the negative sign can be a) wrapped up into the overall phase of

---

[5] This (3.2) may be obtained from equation (2-92) on p. 88 of [68] and equation (4-62a) on p. 172 of [68]) – except a multiplicative factor of $\csc\left(\pi\frac{L}{\lambda}\right)$. Because the current distribution in equation (4-56) of [68] actually has a current of $I_0 \sin\left(\pi\frac{L}{\lambda}\right)$ at the antenna terminals, a factor of $\csc\left(\pi\frac{L}{\lambda}\right)$ must be included for proper normalization of the effective length to reflect an open-circuit voltage at the antenna terminals. This is consistent with, for example, the normalization of the triangular current distribution in equation (4-33) of [68]. Incidentally, this (3.2) has appeared as equation (6) of [44] and as equation (2) of [50].

the incoming/emitted signal, and/or b) negated by changing the polarity of the voltage on the dipole's terminals.

3.2.1 The Special Case of an Half-Wave Dipole

The half-wavelength dipole (a.k.a. the “half-wave dipole") is often used because of these two advantages: (i) Its input impedance is around $73 + j42$ ohms, with a good radiation resistance ($\approx$ 53 ohms), thereby allowing the half-wavelength dipole to be an efficient radiator. (ii) It has a large beamwidth.

For the half-wavelength dipole, i.e. $L = \lambda/2$,

$$\boldsymbol{\ell}_\theta^{\left(\frac{1}{2}\right)} = \overbrace{-\frac{\lambda}{\pi}\frac{\cos\left(\frac{\pi}{2}\cos(\theta)\right)}{\sin(\theta)}}^{\ell_\theta^{(L)} \,:=} \mathbf{u}_\theta. \tag{3.3}$$

The above has drawn upon the fact that $\sin^{-1}\left(\pi\frac{L}{\lambda}\right) = 1$ at $L = \frac{\lambda}{2}$.

Incidentally, an half-wavelength folded dipole has an effective length that equals twice that of an half-wavelength dipole's. Please see page 4-24 of [46].

3.2.2 The Special Case of a “Short" Dipole (a.k.a. “Small" Dipole)

The phrase “short dipoles" is used by [68] (in Section 4.3 and on p. 549) for $\frac{L}{\lambda} \in \left(\frac{1}{50}, \frac{1}{10}\right]$, Such a dipole antenna experiences a current that is triangular along the dipole's length (and linear along each half of the dipole). [6][7]

---

[6] Dipoles shorter than the half-wave dipole would admittedly be less effective as a radiator, but are still used, especially in a portable device, for their small sizes.

[7] For “long" dipoles, i.e. for $\frac{L}{\lambda} \in \left(\frac{1}{10}, 1\right]$, the current is sinusoidal along the length of the dipole.

The following approximation hold: [47,126],

$$\boldsymbol{\ell}_{\theta}^{(L)} \quad = \quad -\frac{L}{2}\sin(\theta)\mathbf{u}_{\theta}. \tag{3.4}$$

See also equation (4-22) of [46]. The above (3.4) is obtained by applying $\cos(\beta) \approx 1 - \frac{\beta^2}{2}$ to the first and the third cosines in (3.2) with $\beta = \pi\frac{L}{\lambda}\cos(\theta_z)$ in the first cosine but with $\beta = \pi\frac{L}{\lambda}$ in the third cosine, then by normalizing the current's maximum magnitude of $\pi\frac{L}{\lambda}$ to unity. Please see equations (4-33) and (4-56) of [68] as well as page 4-24 of [46].

The applicable range of $\frac{L}{\lambda} \in \left(\frac{1}{50}, \frac{1}{10}\right]$ is itself approximate and debatable, depending on the level of precision required. In any case, for dipoles this small, cables and feed networks would likely dominate any “effective length" approximation error.

3.2.3 The Special Case of Infinitesimal Dipoles

The phrase “infinitesimal dipoles" is applied by [68] (p. 162) for $\frac{L}{\lambda} \leq \frac{1}{50}$, although such dipoles are rarely built because of their poor performance on account of their tiny radiation resistance.

Nonetheless, even such an infinitesimal dipole would still be considered to have a “pattern", i.e. an “effective length". At such an infinitesimal electrical length, the electric current has a constant magnitude along the length of the dipole, thereby causing the general expression in (3.2) to degenerate to an “effective length" of $-L\sin(\theta)$.

For a wider perspective: The infinitesimal dipole's “effective length" of $-L\sin(\theta)$ applies for the asymptotic case where $\frac{L}{\lambda} \to 0$, whereas the small dipole's “effective length" of $-\frac{L}{2}\sin(\theta)$ applies for $\frac{L}{\lambda} \to 0.1$. In between 0 and 0.1, the multiplicative factor drops from 1 toward 0.5.

Incidentally, for the physically impractical case of $\frac{L}{\lambda} \to 0$, the dipole's “effective length" would degenerate toward zero, with a vanishing response to an incident electromagnetic wave.

3.3 A Finite-Length Tripole's Array Manifold

Suppose the dipole antenna is oriented along the z-axis:

$$\begin{aligned} v^{(L)} &= \mathbf{e} \cdot \boldsymbol{\ell}_{\theta_z}^{(L)} \\ &= \ell_{\theta_z}^{(L)} \, \mathbf{e} \cdot \mathbf{u}_{\theta_z}^{(L)} \\ &= \ell_{\theta_z}^{(L)} \, \mathbf{e} \cdot \boldsymbol{\ell}_{\theta_z}^{(\text{short})} \, \frac{-1}{\sin(\theta_z)} \frac{2}{L} \\ &= \frac{L}{2} \, e_z \, \ell_{\theta_z}^{(L)} \frac{-1}{\sin(\theta_z)} \frac{2}{L} \;=\; e_z \ell_{\theta_z}^{(L)} \frac{-1}{\sin(\theta_z)}. \end{aligned} \tag{3.5}$$

Similar analysis holds for a dipole antenna oriented along the x-axis or the y-axis.

Consequentially, [8]

$$\mathbf{a}^{(L)} \;=\; - \begin{bmatrix} e_x \\ e_y \\ e_z \end{bmatrix} \circ \begin{bmatrix} \ell_{\theta_x}^{(L)} \\ \ell_{\theta_y}^{(L)} \\ \ell_{\theta_z}^{(L)} \end{bmatrix} \circ \begin{bmatrix} \csc(\theta_x) \\ \csc(\theta_y) \\ \csc(\theta_z) \end{bmatrix}. \tag{3.6}$$

where $\circ$ represents the Hadamard product (a.k.a. the Schur product, or the entrywise product).

3.3.1 The Special Case of Half-Wave Dipoles

For half-wavelength dipoles, the tripole's array manifold becomes

$$\mathbf{a}^{(\frac{\lambda}{2})} = -\frac{\lambda}{\pi} \begin{bmatrix} \frac{\cos\left(\frac{\pi}{2}\cos(\theta_x)\right)}{\sin^2(\theta_x)} \; e_x \\ \frac{\cos\left(\frac{\pi}{2}\cos(\theta_y)\right)}{\sin^2(\theta_y)} \; e_y \\ \frac{\cos\left(\frac{\pi}{2}\cos(\theta_z)\right)}{\sin^2(\theta_z)} \; e_z \end{bmatrix} = -\frac{\lambda}{\pi} \begin{bmatrix} \frac{\cos\left(\frac{\pi}{2}\sin(\theta_z)\cos(\phi_x)\right)}{\sin^2(\theta_z)\sin^2(\phi_x)+\cos^2(\theta_z)} \; e_x \\ \frac{\cos\left(\frac{\pi}{2}\sin(\theta_z)\sin(\phi_x)\right)}{\sin^2(\theta_z)\cos^2(\phi_x)+\cos^2(\theta_z)} \; e_y \\ \frac{\cos\left(\frac{\pi}{2}\cos(\theta_z)\right)}{\sin^2(\theta_z)} \; e_z \end{bmatrix}. \tag{3.7}$$

---

[8] The mutual coupling would be negligible among these three dipoles, if the three dipoles are orthogonally oriented, nearly collocated, and differentially-fed at their central feed points, on account of the symmetry in both the fields and currents/voltages involved in the feed structure. Here, "differential feeding" refers to the signals being fed to the dipoles' terminals in an equal and opposite manner.

3.3.2 The Special Case of Short Dipoles

If the dipole axis lies along the x-axis, its open-circuit voltage v would equal

$$\begin{aligned}
v_x^{(\text{short})} &= \mathbf{e} \cdot \boldsymbol{\ell}_{\theta_x}^{(\text{short})} \\
&= \frac{L}{2} \Big\{ \sin^2(\theta_x)\cos(\phi_x)\cos(\theta_z)\sin(\gamma)e^{j\eta} - \sin^2(\theta_x)\sin(\phi_x)\cos(\gamma) \\
&\quad - \sin(\theta_x)\cos(\theta_x)\cos(\phi_y)\sin(\phi_x)\cos(\theta_z)\sin(\gamma)e^{j\eta} \\
&\quad - \sin(\theta_x)\cos(\theta_x)\cos(\phi_y)\cos(\phi_x)\cos(\gamma) \\
&\quad + \sin(\theta_x)\cos(\theta_x)\sin(\phi_y)\sin(\theta_z)\sin(\gamma)e^{j\eta} \Big\}, \\
&= \underbrace{\{\cos(\theta_z)\cos(\phi_x)\sin(\gamma)e^{j\eta} - \sin(\phi_x)\cos(\gamma)\}}_{= e_x} \frac{L}{2}.
\end{aligned}$$

The second equality draws upon (1.2) and (1.8). The last equality has used some trigonometric identities in Section 1.2.

Similarly, for the dipole axis lies along the y-axis, its open-circuit voltage v would equal

$$\begin{aligned}
v_y^{(\text{short})} &= \mathbf{e} \cdot \boldsymbol{\ell}_{\theta_y}^{(\text{short})} \\
&= \underbrace{\{\cos(\theta_z)\sin(\phi_x)\sin(\gamma)e^{j\eta} + \cos(\phi_x)\cos(\gamma)\}}_{= e_y} \frac{L}{2}.
\end{aligned}$$

Likewise, for the “short" dipole lying along the z-axis, its open-circuit voltage v would equal

$$\begin{aligned}
v_z^{(\text{short})} &= \mathbf{e} \cdot \boldsymbol{\ell}_{\theta_z}^{(\text{short})} \\
&= \underbrace{-\sin(\theta_z)\sin(\gamma)e^{j\eta}}_{= e_z} \frac{L}{2}.
\end{aligned}$$

Therefore, for a triad of three short dipoles in spatial collocation and orthogonal orientation, its array manifold would equal

$$\mathbf{a}^{(\text{short})} = \frac{L}{2} \begin{bmatrix} e_x \\ e_y \\ e_z \end{bmatrix}. \tag{3.8}$$

The above equals the “short dipole" array manifold’s given in the first elements of the vector equation (6) in [47].

3.3.3 The Special Case of Infinitesimal Dipoles

For infinitesimal dipoles, the tripole’s array manifold equals

$$\mathbf{a}^{(\text{infinitesimal})} = L \begin{bmatrix} e_x \\ e_y \\ e_z \end{bmatrix}. \tag{3.9}$$

3.4 Estimation of an Incident Source’s Azimuth-Elevation Direction-of-Arrival or Polarization

Suppose $M > 1$ snapshots of data is collected by the triad, giving an $3 \times M$ space-time data-sample matrix of $\mathbf{Z}$. Form the 3×3 spatial correlation matrix of $\mathbf{Z}\mathbf{Z}^H$, where the superscript ^{H} denotes the Hermitian operator. If there exists only one source[9], the 3×1 principal eigenvector $\mathbf{e}_s$ of $\mathbf{Z}\mathbf{Z}^H$ would span the data’s signal subspace, and would converge toward $c\mathbf{a}$ as the signal-to-noise power ratio (SNR) approaches infinity, with some unknown complex-value scalar c. Therefore, eigen-based parameter estimation [10]has thus estimated the impinging emitter’s 3×1 steering vector, but accurate

---

[9] If more than one source exists, please see the methods in [28, 49, 52–55], among other references.

[10] The maximum-likelihood estimator can reach the Cramér-Rao lower bound (which will be derived in a later section). However, the maximum-likelihood estimator

(i) would require a perfect prior knowledge of the signal-and-noise statistics, and

((ii) would require the iterative optimization of a likelihood function, hence

  (ii-a) would be computationally intensive, and

  (ii-b) would presume the availability of a good estimate (which is often unavailable) to direct the iteration to converge toward the global optimum.

Hence, this section will advance an eigen-based estimator that is non-iterative and that needs no prior knowledge of any signal-and-noise statistics.

only to within a complex-value scalar c, which is unknown to the algorithm. In other words, the algorithm has available (for each incident emitter) a 3×1 estimate:

$$\hat{\mathbf{a}}^{(L)} \quad \approx \quad c\mathbf{a}^{(L)}. \tag{3.10}$$

The above approximation would become a equality, if noises were absent or if an infinite number of snapshots were available.

Toward deriving the estimation formulas for the incident source's azimuth-elevation direction-of-arrival and polarization, eliminate the complex phase from the third entry in (3.10), to give

$$\begin{aligned}
\bar{\mathbf{a}} \quad &:= \quad \hat{\mathbf{a}}^{(L)} \, e^{-j\angle\left[\hat{\mathbf{a}}^{(L)}\right]_3} \\
&\approx \quad |c| \begin{bmatrix} -\ell_{\theta_x}^{(L)} / \sin(\theta_x) \\ -\ell_{\theta_y}^{(L)} / \sin(\theta_y) \\ -\ell_{\theta_z}^{(L)} / \sin(\theta_z) \end{bmatrix} \\
&\qquad \circ \begin{bmatrix} \sin(\gamma)\cos\left(\theta_z\right)\cos\left(\phi_x\right) - \cos(\gamma)\sin\left(\phi_x\right)\cos(\eta) \\ \sin(\gamma)\cos\left(\theta_z\right)\sin\left(\phi_x\right) + \cos(\gamma)\cos\left(\phi_x\right)\cos(\eta) \\ -\sin(\gamma)\sin\left(\theta_z\right) \end{bmatrix} \\
&\qquad + j\,|c| \begin{bmatrix} -\ell_{\theta_x}^{(L)} / \sin(\theta_x) \\ -\ell_{\theta_y}^{(L)} / \sin(\theta_y) \\ -\ell_{\theta_z}^{(L)} / \sin(\theta_z) \end{bmatrix} \circ \begin{bmatrix} \cos(\gamma)\sin\left(\phi_x\right)\sin(\eta) \\ -\cos(\gamma)\cos\left(\phi_x\right)\sin(\eta) \\ 0 \end{bmatrix}.
\end{aligned} \tag{3.11}$$

Here, (3.11) offers 5 real-value constraints, with the 4 real-value unknowns of $|c|$, $\frac{-\ell_{\theta_x}^{(L)}}{\sin(\theta_x)}$, $\frac{-\ell_{\theta_y}^{(L)}}{\sin(\theta_y)}$, and $\frac{-\ell_{\theta_z}^{(L)}}{\sin(\theta_z)}$ as nuisance parameters, which may be removed subsequently by taking the ratio between real-value part and the imaginary part of $\left[\bar{\mathbf{a}}\right]_\ell$, for $\ell = 1, 2$.

Section 3.4.1 below will derive and will simulate new bivariate direction-finding formulas in close form, based on a prior knowledge of the polarization. Section 3.4.2 will do the same for the polarization estimation, assuming prior knowledge of the direction-of-arrival. [11]

---

[11] Simultaneous estimation of the polar-azimuth bivariate direction-of-arrival and the bivariate polarization is infeasible here under the above eigen-based pre-processing, because there would be 7 unknown real-value scalars, $\left(\text{namely}, \gamma, \eta, \phi_x, \theta_z, \frac{|c|\ell_x^{(L)}}{\sin(\theta_x)}, \frac{|c|\ell_y^{(L)}}{\sin(\theta_y)}, \frac{|c|\ell_z^{(L)}}{\sin(\theta_z)}\right)$ but only 5 constraints (3.11), leading to an under-determined situation. A non-eigen-based estimator simultaneously for all four parameters will be presented in Section 3.5.

3.4.1 Estimation of the Incident Source's Azimuth-Polar Direction-of-Arrival, (ϕ_x, θ_z)

Assume that the incident emitter's polarization (γ, η) is prior known. The only unknowns would then be θ_z, ϕ_x, $\frac{-\ell_{\theta_x}^{(L)}|c|}{\sin(\theta_x)}$, $\frac{-\ell_{\theta_y}^{(L)}|c|}{\sin(\theta_y)}$, and $\frac{-\ell_{\theta_z}^{(L)}|c|}{\sin(\theta_z)}$. [12]

To yield the direction-of-arrival estimates, $\hat{\theta}_z$ and $\hat{\phi}_x$, form the following ratios: Using the first row of the vector-equation in (3.11), define

$$\begin{aligned} \alpha_x \quad &:= \quad \frac{\Re\left\{[\bar{\mathbf{a}}]_1\right\}\sin(\eta) + \Im\left\{[\bar{\mathbf{a}}]_1\right\}\cos(\eta)}{\Im\left\{[\bar{\mathbf{a}}]_1\right\}} \\ &= \quad \tan(\gamma)\ \cot\left(\phi_x\right)\ \cos\left(\theta_z\right), \end{aligned} \tag{3.12}$$

where $\Re\{\cdot\}$ and $\Im\{\cdot\}$ respectively symbolize the real-value part and the imaginary part of the entity inside the curly brackets. Also, based on the second row of the vector-equation in (3.11), define

$$\begin{aligned} \alpha_y \quad &:= \quad \frac{\Re\left\{[\bar{\mathbf{a}}]_2\right\}\sin(\eta) + \Im\left\{[\bar{\mathbf{a}}]_2\right\}\cos(\eta)}{\Im\left\{[\bar{\mathbf{a}}]_2\right\}} \\ &= \quad -\tan\gamma\ \tan\left(\phi_x\right)\ \cos\left(\theta_z\right). \end{aligned} \tag{3.13}$$

From (3.12) and (3.13), the incident source's azimuth-polar direction-of-arrival may be estimated as

$$\hat{\phi}_x \quad := \quad \begin{cases} -\pi + \arctan\left|\frac{\alpha_y}{\alpha_x}\right|^{1/2}, & \text{if } \phi_x \in [-\pi, -\frac{\pi}{2}), \\ \arctan\left(-\left|\frac{\alpha_y}{\alpha_x}\right|^{1/2}\right), & \text{if } \phi_x \in [-\frac{\pi}{2}, 0), \\ \arctan\left|\frac{\alpha_y}{\alpha_x}\right|^{1/2}, & \text{if } \phi_x \in [0, \frac{\pi}{2}), \\ \pi + \arctan\left(-\left|\frac{\alpha_y}{\alpha_x}\right|^{1/2}\right), & \text{if } \phi_x \in [\frac{\pi}{2}, \pi); \end{cases} \tag{3.14}$$

$$\hat{\theta}_z \quad := \quad \arccos\left(\operatorname{sgn}\left(\alpha_x \frac{\tan\hat{\phi}_x}{\tan\gamma}\right)\frac{|\alpha_x\alpha_y|^{1/2}}{|\tan\gamma|}\right). \tag{3.15}$$

---

[12] One sample scenario whereby the polarization is prior known and only the DOA needs to be estimated is as follows. In certain types of sensor-network geolocation applications and in some RFID networks, the to-be-geolocated or the to-be-tracked mobile uses antennas at a polarization that is prior known to the sensors. E.g., a linearly polarization antenna is vertically/horizontally affixed on a mobile vehicle, or a circular polarized antenna is used by the mobile vehicle. The sensor network and the RFID sensors would thus have a prior knowledge of the mobile vehicle's signal polarization.

These estimators requires no prior knowledge of L, λ, nor the digital frequency. The estimator $\hat{\phi}_x$ has a support-range of $[-\pi, -\frac{\pi}{2})$ or $[-\frac{\pi}{2}, 0)$ or $[0, \frac{\pi}{2})$ or $[\frac{\pi}{2}, \pi)$. The estimator $\hat{\theta}_z$ has a support-range of $[0, \pi]$.

The new estimators proposed above in (3.14) and (3.15) have their efficacy verified below by Monte Carlo simulations, which are shown in Figures 3.2a-3.2b.

To focus on the influence of the electrical length $\frac{L}{\lambda}$, a simple data model will be used below: A zero-mean complex-value Gaussian noise signal $\mathbf{s}(m)$, impinges upon the triad. At the mth time-instant, the triad collects the 3×1 data-vector,

$$\mathbf{z}(m) \;\; = \;\; \mathbf{a}^{(L)} s(m) + \mathbf{n}(m). \tag{3.16}$$

Moreover, the additive noise $\mathbf{n}(m)$ denotes a 3×1 vector of zero-mean complex-value Gaussian additive noise, spatio-temporally uncorrelated over time and across the dipoles, while statistically independent from all other entities, hence with a deterministic covariance matrix of $\mathbf{\Gamma}_0 = \mathrm{diag}\left(\sigma_n^2, \sigma_n^2, \sigma_n^2\right)$, where σ_n^2 representing the noise variance at each dipole. With M number of time-samples, the $3M \times 1$ collected data-set equals

$$\boldsymbol{\zeta} \;\; = \;\; \left[(\mathbf{z}(1))^T, \cdots, (\mathbf{z}(M))^T\right]^T. \tag{3.17}$$

The corresponding Cramér-Rao bounds (CRB) are derived in Appendix A. (Recall that the Cramér-Rao bound lower-bounds the estimation error variance of any unbiased estimator; and the Cramér-Rao bound itself is independent of the specific estimator employed.)

In this Chapter's all subsequent numerical examples, $M = 90$, $\phi_x = 45^o$, $\theta_z = 80^o$, $\gamma = 80^o$, and $\eta = 75^o$. Each icon on every graph represents $1,000$ independent Monte Carlo experiments. These figures show $\frac{L}{\lambda}$ only up to 0.8, because the "effective length" expression of (3.2) is invalid when the physical length is near integer- multiples of the wavelength. As explained earlier, the electric current is actually not a null at the feed point, but only relatively small there.

Figures 3.2a-3.2b verify the proposed estimators' efficacy as well as the estimators' closeness to the Cramér-Rao bounds. These figures further suggest that the shorter the dipole, the less accurate the estimates would be, and the higher the SNR would be for the estimators to begin to break down. [13]

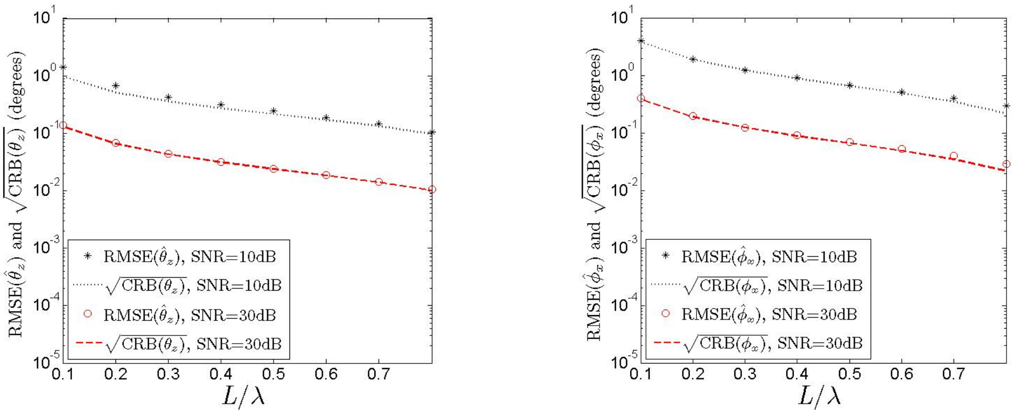

(a) RMSE and $\sqrt{\mathrm{CRB}}$ for $\hat{\theta}_z$, versus $\frac{L}{\lambda}$, at $\mathrm{SNR} = 10, 30\mathrm{dB}$.

(b) RMSE and $\sqrt{\mathrm{CRB}}$ for $\hat{\phi}_x$, versus $\frac{L}{\lambda}$, at $\mathrm{SNR} = 10, 30\mathrm{dB}$.

Fig. 3.2.: RMSE and $\sqrt{\mathrm{CRB}}$ for $\hat{\theta}_z$ and $\hat{\phi}_x$ versus $\frac{L}{\lambda}$ using dipole triad.

3.4.2 Estimation of the Incident Source's Polarization, (γ, η)

Assume that the incident emitter's direction-of-arrival (ϕ_x, θ_z) is prior known.[14] The only unknowns would then be γ, η, $\frac{-|c|\ell_{\theta_x}^{(L)}}{\sin(\theta_x)}$, $\frac{-|c|\ell_{\theta_y}^{(L)}}{\sin(\theta_y)}$, and $\frac{-|c|\ell_{\theta_z}^{(L)}}{\sin(\theta_z)}$. [15]

The last three unknowns are common to the real-value part and the imaginary part of the vector-equation in (3.11). Thus, these unknowns may be

---

[13] Recall that the "effective length" affects the dipole's gain, nonlinearly and non-monotonically in (3.2), through sinusoidal functions.

[14] The open-form polarization-estimation algorithm in [59] also requires the prior knowledge of the direction-of-arrival.

[15] One sample scenario whereby the incident signal's direction-of-arrival is prior known and only the incident signal's polarization needs to be estimated is as follows: After a high-resolution radar (HRR) system is in "locked-on" mode with regard to a target, the direction-of-arrival is already known (roughly) to the radar receiver. In that "locked-on" mode, the radar returns' polarization signature would facilitate the radar system (i) to classify the target into specific types (e.g. an F-16 jet versus an MiG jet versus others) based on a priori polarimetric "template" profiles, or (ii) to estimate the target's shape or materials construction.

removed by forming the ratio between the real-value part and the imaginary-value part of each element in (3.11), giving

$$\frac{\Re\{[\bar{\mathbf{a}}]_1\}}{\Im\{[\bar{\mathbf{a}}]_1\}} = \frac{\tan(\gamma)}{\tan(\phi_x)}\frac{\cos(\theta_z)}{\sin(\eta)} - \frac{1}{\tan(\eta)}, \tag{3.18}$$

$$\frac{\Re\{[\bar{\mathbf{a}}]_2\}}{\Im\{[\bar{\mathbf{a}}]_2\}} = -\tan(\gamma)\tan(\phi_x)\frac{\cos(\theta_z)}{\sin(\eta)} - \frac{1}{\tan(\eta)}. \tag{3.19}$$

The third element's imaginary-value part equals zero; hence, the ratio $\frac{\Re\{[\bar{\mathbf{a}}]_3\}}{\Im\{[\bar{\mathbf{a}}]_3\}}$ would not be useful. Nonetheless, the two constraints in (3.18)-(3.19) will be shown below to suffice to estimate the two unknowns of η and γ.

To estimate η from (3.18)-(3.19):

$$\frac{\Re\{[\bar{\mathbf{a}}]_1\}}{\Im\{[\bar{\mathbf{a}}]_1\}}\tan(\phi_x) + \frac{\Re\{[\bar{\mathbf{a}}]_2\}}{\Im\{[\bar{\mathbf{a}}]_2\}}\cot(\phi_x) = \frac{-1}{\tan(\eta)}(\tan(\phi_x) + \cot(\phi_x)), \tag{3.20}$$

which contains only one unknown, η. Hence,

$$\hat{\eta} := \arctan\left\{\frac{-\tan(\phi_x) - \cot(\phi_x)}{\frac{\Re\{[\bar{\mathbf{a}}]_1\}}{\Im\{[\bar{\mathbf{a}}]_1\}}\tan(\phi_x) + \frac{\Re\{[\bar{\mathbf{a}}]_2\}}{\Im\{[\bar{\mathbf{a}}]_2\}}\cot(\phi_x)}\right\}. \tag{3.21}$$

To estimate γ, subtract (3.19) from (3.18), giving

$$\frac{\Re\{[\bar{\mathbf{a}}]_1\}}{\Im\{[\bar{\mathbf{a}}]_1\}} - \frac{\Re\{[\bar{\mathbf{a}}]_2\}}{\Im\{[\bar{\mathbf{a}}]_2\}} = \frac{\tan(\gamma)}{\tan(\phi_x)}\frac{\cos(\theta_z)}{\sin(\eta)} + \tan(\gamma)\tan(\phi_x)\frac{\cos(\theta_z)}{\sin(\eta)}. \tag{3.22}$$

Multiply both sides of (3.22) by $\sin(\hat{\eta})$. Assuming that $\hat{\eta} \approx \eta$,

$$\sin(\hat{\eta})\left(\frac{\Re\{[\bar{\mathbf{a}}]_1\}}{\Im\{[\bar{\mathbf{a}}]_1\}} - \frac{\Re\{[\bar{\mathbf{a}}]_2\}}{\Im\{[\bar{\mathbf{a}}]_2\}}\right) \approx \tan(\gamma)\left(\cot(\phi_x)\cos(\theta_z) + \tan(\phi_x)\cos(\theta_z)\right). \tag{3.23}$$

Therefore,

$$\hat{\gamma} \quad := \quad \arctan\left\{ \frac{\sin(\hat{\eta})}{\cos(\theta_z)} \, \frac{\dfrac{\Re\left\{[\bar{\mathbf{a}}]_1\right\}}{\Im\left\{[\bar{\mathbf{a}}]_1\right\}} - \dfrac{\Re\left\{[\bar{\mathbf{a}}]_2\right\}}{\Im\left\{[\bar{\mathbf{a}}]_2\right\}}}{\cot(\phi_x) + \tan(\phi_x)} \right\}. \tag{3.24}$$

These estimation formulas proposed here in Section 3.4.2 do not require any prior knowledge of L, λ, or the digital frequency.

To verify the efficacy of the eigen-based estimators proposed above in (3.21) and (3.24), Monte Carlo simulations are conducted below using the same measurement model and the same numerical settings as in Section 3.4.1. These simulation results are shown in Figures 3.3a-3.3b, along with the corresponding Cramér-Rao bounds, which have been derived in Appendix B.

Figures 3.3a-3.3b verify the proposed estimators' efficacy and their closeness to the Cramér-Rao bounds. These figures further suggest that the shorter the dipole, the less accurate the estimates would be, and the higher the SNR would be for the estimators to begin to break down.

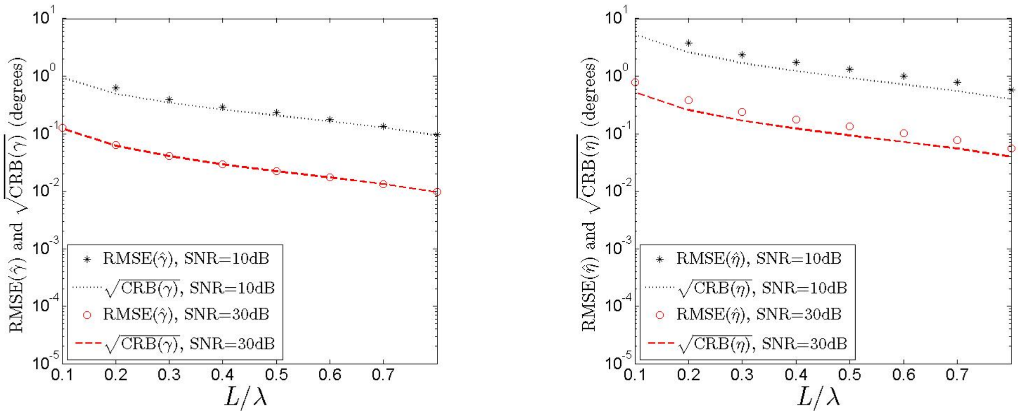

(a) RMSE and $\sqrt{\text{CRB}}$ for $\hat{\gamma}$, versus $\frac{L}{\lambda}$, at $\text{SNR} = 10, 30\text{dB}$.

(b) RMSE and $\sqrt{\text{CRB}}$ for $\hat{\eta}$, versus $\frac{L}{\lambda}$, at $\text{SNR} = 10, 30\text{dB}$.

Fig. 3.3.: RMSE and $\sqrt{\text{CRB}}$ for $\hat{\gamma}$ and $\hat{\eta}$ versus $\frac{L}{\lambda}$ using dipole triad.

3.5 Simultaneous Estimation of the Direction-of-Arrival and Polarization

Suppose the incident signal is a pure tone, $s(m) = e^{j2\pi f_d m}$, with a prior known digital frequency of f_d. [16]At the mth time-instant, the triad collects the 3×1 data-vector,

$$\mathbf{z}(m) \quad = \quad \mathbf{a}^{(L)} s(m) + \mathbf{n}(m). \tag{3.25}$$

3.5.1 To Estimate the Polarization Phase-difference, η

Define

$$\begin{aligned} \tilde{\mathbf{a}}^{(L)} &:= \frac{1}{M} \sum_{m=1}^{M} \mathbf{z}(m) e^{-j2\pi f_d m} \\ &\approx \mathbf{a}^{(L)}. \end{aligned} \tag{3.26}$$

Hence, $\left[\tilde{\mathbf{a}}^{(L)}\right]_3 \approx \left[\mathbf{a}^{(L)}\right]_3 = \sin(\gamma) \ell_{\theta_z}^{(L)} e^{j\eta}$. Recalling that $\ell_{\theta_z}^{(L)}$ is real-value,

$$\hat{\eta} \quad := \quad \angle \left[\tilde{\mathbf{a}}^{(L)}\right]_3 . \tag{3.27}$$

The estimation above needs no prior knowledge of L nor λ.

3.5.2 To Estimate the Azimuth Angle, ϕ_x

The following ratios are judiciously chosen to yield the direction-of-arrival estimate, $\hat{\phi}_x$. Using the first row of the vector-equation

$$\mathbf{b} \quad := \quad \tilde{\mathbf{a}}^{(L)} e^{-j\angle\left[\tilde{\mathbf{a}}^{(L)}\right]_3}, \tag{3.28}$$

---

[16] Alternatively, if the incident signal is not pure-tone: Apply a sliding time-window short-time digital Fourier transformation (ST-DFT) to the data sequence. This sliding-window ST-DFT will output $\{s(m)\}$ at the dth frequency-bin at a digital frequency of f_d.

define

$$\begin{aligned} \chi_x &:= \frac{\Re\left\{[\mathbf{b}]_1\right\}\sin(\hat{\eta}) + \Im\left\{[\mathbf{b}]_1\right\}\cos(\hat{\eta})}{\Im\left\{[\mathbf{b}]_1\right\}} \\ &\approx \tan(\gamma)\ \cot\left(\phi_x\right)\ \cos\left(\theta_z\right). \end{aligned} \tag{3.29}$$

Based on the second row of the vector-equation in (3.28), define

$$\begin{aligned} \chi_y &:= \frac{\Re\left\{[\mathbf{b}]_2\right\}\sin(\hat{\eta}) + \Im\left\{[\mathbf{b}]_2\right\}\cos(\hat{\eta})}{\Im\left\{[\mathbf{b}]_2\right\}} \\ &\approx -\tan(\gamma)\ \tan\left(\phi_x\right)\ \cos\left(\theta_z\right), \end{aligned} \tag{3.30}$$

where $\Re\{\cdot\}$ and $\Im\{\cdot\}$ respectively symbolize the real-value part and the imaginary part of the entity inside the curly brackets.

After computing (3.29) and (3.30), the emitter's azimuth direction-of-arrival may be estimated as

$$\hat{\phi}_x := \begin{cases} -\pi + \arctan\left(\left|\frac{\chi_y}{\chi_x}\right|^{1/2}\right), & \text{if } \phi_x \in [-\pi, -\frac{\pi}{2}), \\ \arctan\left(-\left|\frac{\chi_y}{\chi_x}\right|^{1/2}\right), & \text{if } \phi_x \in [-\frac{\pi}{2}, 0), \\ \arctan\left(\left|\frac{\chi_y}{\chi_x}\right|^{1/2}\right), & \text{if } \phi_x \in [0, \frac{\pi}{2}), \\ \pi + \arctan\left(-\left|\frac{\chi_y}{\chi_x}\right|^{1/2}\right), & \text{if } \phi_x \in [\frac{\pi}{2}, \pi). \end{cases} \tag{3.31}$$

This estimator has a support-range of $[-\pi, -\frac{\pi}{2})$, or $[-\frac{\pi}{2}, 0)$, or $[0, \frac{\pi}{2})$, or $[\frac{\pi}{2}, \pi)$.

3.5.3 To Estimate the Polar Angle, θ_z

With $\phi_x \approx \hat{\phi}_x$, re-write (3.29) as

$$\tan(\gamma) = \frac{\chi_x \tan(\hat{\phi}_x)}{\cos(\theta_z)}. \tag{3.32}$$

With $\eta \approx \hat{\eta}$, define

$$\begin{aligned} \alpha_z &:= \frac{\Re\{[\mathbf{b}]_3\} \sin(\hat{\phi}_x) \sin(\hat{\eta})}{\Im\{[\mathbf{b}]_1\}} \\ &\approx \underbrace{-\frac{\ell^{(L)}_{\theta_z}}{\ell^{(L)}_{\theta_x}} \tan(\gamma) \sin(\theta_x)}_{:=\alpha_h}. \end{aligned}$$

Using (3.32) in α_h gives

$$\alpha_h = \frac{-\chi_x \ell^{(L)}_{\theta_z} \tan \hat{\phi}_x \sin(\theta_x)}{\ell^{(L)}_{\theta_x} \cos(\theta_z)}. \tag{3.33}$$

Recall that θ_x above depends on only ϕ_x and θ_z.

With a prior knowledge of $\frac{L}{\lambda}$, the only unknown in (3.33) is θ_z. Hence,

$$\hat{\theta}_z = \arg\min_{\theta_z} |\alpha_z - \alpha_h|. \tag{3.34}$$

3.5.4 To Estimate the Auxiliary Polarization Angle, γ

From (3.28),

$$\frac{\Re\left\{[\mathbf{b}]_1\right\}}{\Im\left\{[\mathbf{b}]_1\right\}} = \frac{\tan(\gamma)}{\tan(\phi_x)}\frac{\cos(\theta_z)}{\sin(\eta)} - \frac{1}{\tan(\eta)}, \tag{3.35}$$

$$\frac{\Re\left\{[\mathbf{b}]_2\right\}}{\Im\left\{[\mathbf{b}]_2\right\}} = -\tan(\gamma)\tan(\phi_x)\frac{\cos(\theta_z)}{\sin(\eta)} - \frac{1}{\tan(\eta)}. \tag{3.36}$$

As $\Im\left\{[\mathbf{b}]_3\right\} = 0$, the ratio $\frac{\Re\left\{[\mathbf{b}]_3\right\}}{\Im\left\{[\mathbf{b}]_3\right\}}$ would not be useful.

Subtract (3.36) from (3.35) to give

$$\frac{\Re\left\{[\mathbf{b}]_1\right\}}{\Im\left\{[\mathbf{b}]_1\right\}} - \frac{\Re\left\{[\mathbf{b}]_2\right\}}{\Im\left\{[\mathbf{b}]_2\right\}} = \frac{\tan(\gamma)}{\tan(\phi_x)}\frac{\cos(\theta_z)}{\sin(\eta)} + \tan(\gamma)\tan(\phi_x)\frac{\cos(\theta_z)}{\sin(\eta)} \tag{3.37}$$

Multiply both sides of (3.37) by $\sin(\hat{\eta})$. With $\hat{\eta} \approx \eta$, $\phi_x \approx \hat{\phi}_x$, $\theta_z \approx \hat{\theta}_z$,

$$\sin(\hat{\eta})\left(\frac{\Re\left\{[\mathbf{b}]_1\right\}}{\Im\left\{[\mathbf{b}]_1\right\}} - \frac{\Re\left\{[\mathbf{b}]_2\right\}}{\Im\left\{[\mathbf{b}]_2\right\}}\right) \approx \tan(\gamma)\left(\cot(\hat{\phi}_x)\cos(\hat{\theta}_z) + \tan(\hat{\phi}_x)\cos(\hat{\theta}_z)\right). \tag{3.38}$$

Therefore,

$$\hat{\gamma} := \arctan\left\{\frac{\sin(\hat{\eta})}{\cos(\hat{\theta}_z)}\frac{\frac{\Re\left\{[\mathbf{b}]_1\right\}}{\Im\left\{[\mathbf{b}]_1\right\}} - \frac{\Re\left\{[\mathbf{b}]_2\right\}}{\Im\left\{[\mathbf{b}]_2\right\}}}{\cot(\hat{\phi}_x) + \tan(\hat{\phi}_x)}\right\}. \tag{3.39}$$

3.5.5 Monte Carlo Simulations

Monte Carlo simulations in Figures 3.4a-3.4d verify the efficacy of the estimators proposed in Sections 3.5.1-3.5.4 above. The additive noise $\{\mathbf{n}(m), \forall m\}$ is modeled as in Section 3.4.1; and the numerical settings are also same as in Section 3.4.1.

Moreover, Figures 3.4a-3.4d also show the proposed estimators to be close to the Cramér-Rao bounds derived in Appendix C.

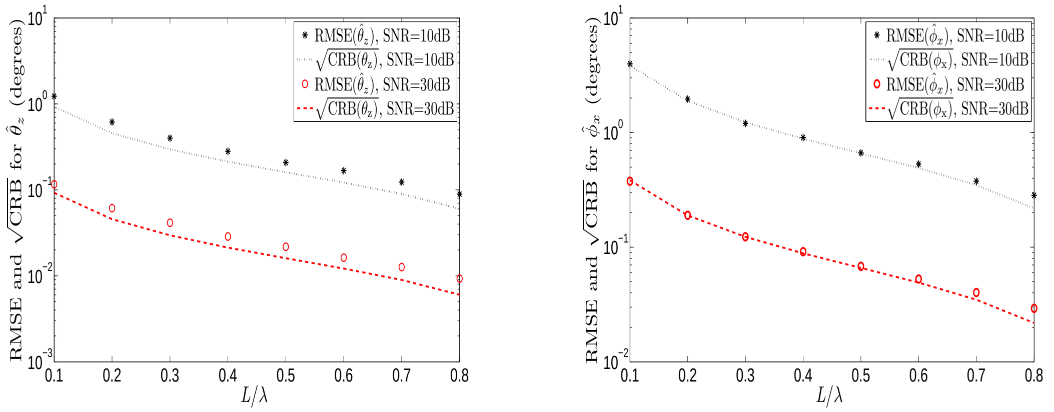

(a) RMSE and $\sqrt{\text{CRB}}$ for $\hat{\theta}_z$, versus $\frac{L}{\lambda}$, at SNR $= 10, 30$dB.

(b) RMSE and $\sqrt{\text{CRB}}$ for $\hat{\phi}_x$, versus $\frac{L}{\lambda}$, at SNR $= 10, 30$dB.

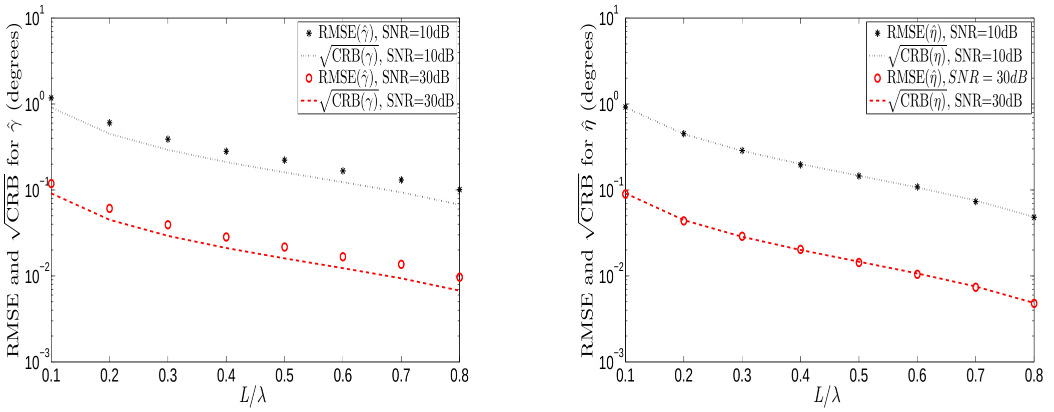

(c) RMSE and $\sqrt{\text{CRB}}$ for $\hat{\gamma}$, versus $\frac{L}{\lambda}$, at SNR $= 10, 30$dB.

(d) RMSE and $\sqrt{\text{CRB}}$ for $\hat{\eta}$, versus $\frac{L}{\lambda}$, at SNR $= 10, 30$dB.

Fig. 3.4.: RMSE and $\sqrt{\text{CRB}}$ for $(\hat{\theta}_z, \hat{\phi}_x, \hat{\gamma}, \hat{\eta})$ versus $\frac{L}{\lambda}$ using dipole triad.

3.6 Conclusion

For a triad of collocated and perpendicular “long" dipoles, this investigation is first in the open literature to propose closed-form algorithms to estimate an impinging signal’s the incident azimuth-elevation direction and/or the incident bivariate polarization. The proposed estimators – in (3.14), (3.15), (3.21), and (3.24) – can closely approach the Cramér-Rao bounds, as shown in the presented Monte Carlo simulations. These proposed estimators (developed for a collocated/perpendicular triad of “long" dipoles) may be substituted right into the dozens of schemes mentioned in Section I-1) of [62] for “short" dipole triads, thereby generalizing those established schemes for pragmatic use with practical dipoles of an effective radiation efficiency.

4

Electrically Long Dipoles – Positioned Sparsely on an Extended Circumference and Oriented Radially or Tangentially – for DoA and Polarization Estimation

4.1 Introduction

Electrically long dipole signal processing is for the first time investigated in Chapter 3. Nonetheless, that pioneering investigation focuses exclusively on a *spatially co-centered* unit of “electrically long" dipoles in orthogonal orientation relative to each other.

Though the extended-aperture sensor-array direction-finding literature is vast, but that literature is almost always limited to short dipoles [99–102, 105–110, 125] or limited to long dipoles that are all identically oriented [103, 104, 111–124]. Arbitrary directional sensors array with extended aperture is considered for direction finding in [153–169] and it is indicated that higher directivity can improve the performance [123]. However, for electrically long dipoles that are positioned over a spatial aperture with diverse orientation, for the purpose of estimating impinging electromagnetic signals' arrival directions and polarizations – this chapter pioneers the open literature's first signal-processing algorithm in closed form. The dipoles here may be electrically long, not electrically short as typically required in the dipole-array signal processing literature. The inter-dipole separation here may exceed half a wavelength, to realize an extended aperture to enhance the array's spatial resolution of incident sources. This proposed algorithm is verified via Monte Carlo simulations, to be efficacious and to approach the Cramer-Rao bound.

For this chapter to achieve *closed*-form direction finding with an extended aperture, despite the diverse orientation of the dipoles that are electrically long – this achievement is unprecedented in the open literature (to the best of knowledge).

4.1.1 A circular array of differently oriented dipoles

The electrically long dipole's voltage equals the incident electric-field vector multiplied (via an inner product) into the dipole's "effective length" vector. The "effective length" (a misnomer) is not a "length" per se, but a multivariate pattern. This pattern depends on the impinging source's direction-of-arrival relative to the dipole's axis. Hence, the dipole's "effective length" is not a univariate function of that dipole's electrical length $\frac{L}{\lambda}$.

This chapter considers a circular array of *radially* oriented dipoles, each dipole would have a different orientation and thus a different "effective length". The same holds for *tangentially* oriented dipoles positioned on a circle. In contrast, if the array's every dipole is oriented identically (e.g. if all vertically oriented), all dipoles' "effective lengths" (for an incident plane wave) would be all identical. Then, these "effective lengths" may be factored out into a factor common to all entries in the array manifold.

Each electrically long dipole's directional gain pattern varies nonlinearly with the incident source's unknown direction-of-arrival (θ_z, ϕ_x), unknown polarization (γ, η), and wavelength (λ). This penta-variate dependence is highly complicated, and differs for different dipoles (i.e. for different values of ℓ). Hence, the array manifold's every entry is a differently complicated nonlinear function of the concerned dipole's $\left\{\frac{L}{\lambda}, \tilde{\theta}_i\right\}$ and the incident source's $\{\theta_k, \phi_k, \gamma_k, \eta_k\}$ Nonetheless, Section 4.4 will develop a closed-form estimator of the bivariate direction-of-arrival and the bivariate polarization.

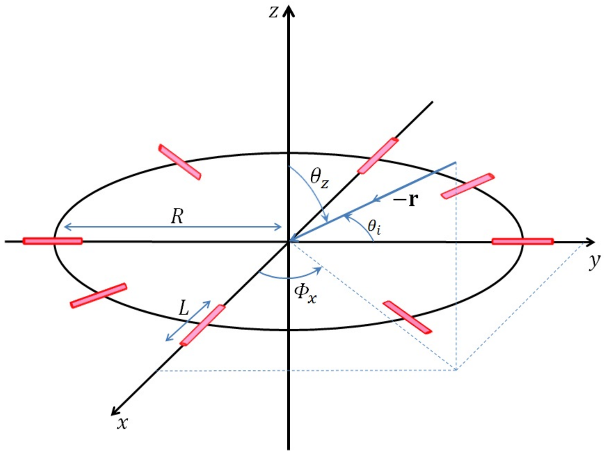

Fig. 4.1.: Uniform circular array of radially oriented dipoles.

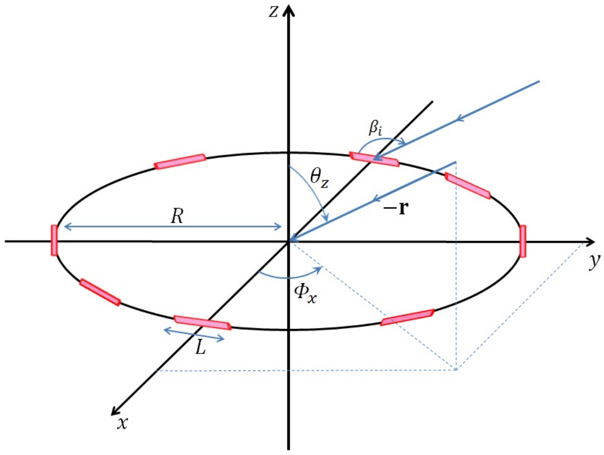

Fig. 4.2.: Uniform circular array of tangentially oriented dipoles.

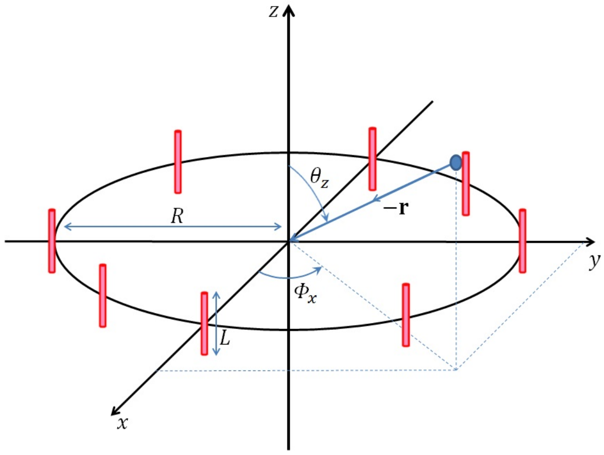

Fig. 4.3.: Uniform circular array of vertically oriented dipoles.

4.1.2 Aperture extension by sparsely spacing sensors on a circle

The circular array configurations mentioned above can realize an extended aperture (i.e. with an inter-sensor spacing exceeding half a wavelength), without incurring ambiguous direction-of-arrival estimates. This chapter will advance new estimation algorithms in closed forms, for use with a circular array of any even number (≥ 4) of "electrically long" dipoles, to form a two-dimensional circular spatial aperture to span many wavelengths.

This chapter will focus on two orientational configurations:

1) All dipoles are *radially* oriented with regard to the polar coordinates' origin.

2) All dipoles are *tangentially* oriented with regard to the circumference.

Not to be investigated in this chapter is the case of all dipoles being vertically oriented, because all dipoles' "effective lengths" can then be factored out as a multiplicative factor common to all entries of the array manifold, which then equals that of a circular array of *isotropic* sensors. Each incident source's azimuth-elevation arrival direction and polarization will be simultaneously estimated.

4.2 Derivation of the Array Manifold

Toward formulating the overall dipole-array's mathematical array manifold in Section 4.2.2 for radially oriented dipoles and in Section 4.2.3 for tangentially oriented dipoles, the next Section 4.2.1 will first develop each dipole's effective length as a function of that dipole's orientation.

4.2.1 Basics of Electrically Long Dipoles at Various Orientations

Consider an electromagnetic plane wave of unit power per unit area and of wavelength λ. Suppose this wave impinges from the far field upon the Cartesian origin, at an incident polar angle (a.k.a. a zenith angle) of $\theta_z \in [0, \pi]$, an azimuth angle of $\phi_x \in [-\pi, \pi)$, an auxiliary polarization angle of $\gamma \in [0, \pi/2)$, and a polarization phase difference of $\eta \in [-\pi, \pi)$. This wave's electric-field vector may be expressed in the Cartesian coordinates as

$$\mathbf{e} = \begin{bmatrix} e_x \\ e_y \\ e_z \end{bmatrix} = \begin{bmatrix} \cos(\phi_x)\cos(\theta_z) & -\sin(\phi_x) \\ \sin(\phi_x)\cos(\theta_z) & \cos(\phi_x) \\ -\sin(\theta_z) & 0 \end{bmatrix} \begin{bmatrix} \sin(\gamma)e^{j\eta} \\ \cos(\gamma) \end{bmatrix}. \tag{4.1}$$

Suppose the above-described incident wave impinges upon an electrically long dipole, of physical length L (i.e., with an electrical length of $\frac{L}{\lambda}$), and aligned along the x-axis. This would produce a voltage of $e_x \ell_{\theta_x}^{(L)} \csc(\theta_x)$ [97], where

$$\ell_{\theta_x}^{(L)} = \frac{\lambda}{\pi \sin(\pi \frac{L}{\lambda})} \frac{\cos\left(\pi \frac{L}{\lambda} \cos(\theta_x)\right) - \cos\left(\pi \frac{L}{\lambda}\right)}{\sin(\theta_x)}. \tag{4.2}$$

is labelled the "effective length" of the electrically long dipole. In the above, θ_x represents the spatial angle between the x-axis and the negative of the incident direction as in Figure 1.3; and

$$\begin{aligned}\sin\left(\theta_x\right) &= \sqrt{\sin^2\left(\theta_z\right)\sin^2\left(\phi_x\right)+\cos^2\left(\theta_z\right)} \\ \cos\left(\theta_x\right) &= \sin\left(\theta_z\right)\cos\left(\phi_x\right).\end{aligned}$$

On the other hand, if this same long dipole is aligned along the y-axis, its measured voltage [97] would instead equal $e_y \ell_{\theta_y}^{(L)} \csc(\theta_y)$, where

$$\ell_{\theta_y}^{(L)} = \frac{\lambda}{\pi\sin(\pi\frac{L}{\lambda})}\frac{\cos\left(\pi\frac{L}{\lambda}\cos\left(\theta_y\right)\right)-\cos\left(\pi\frac{L}{\lambda}\right)}{\sin\left(\theta_y\right)}, \tag{4.3}$$

symbolizes the effective length. Here, θ_y denotes the spatial angle between the y-axis and the negative of the incident direction as in Figure 1.3; and

$$\begin{aligned}\sin\left(\theta_y\right) &= \sqrt{\sin^2\left(\theta_z\right)\cos^2\left(\phi_x\right)+\cos^2\left(\theta_z\right)} \\ \cos\left(\theta_y\right) &= \sin\left(\theta_z\right)\sin\left(\phi_x\right).\end{aligned}$$

Lastly, if this long dipole is aligned at an azimuth angle of

$$\tilde{\theta}_i := (i-1)\frac{2\pi}{I} \tag{4.4}$$

counter-clockwise from the positive x-axis, its measured voltage would instead equal

$$v_i = e_i \ell_{\theta_i}\csc(\theta_i), \tag{4.5}$$

where θ_i represents the spatial angle between the ith dipole's axis and the negative of the incident direction; and

$$\begin{aligned}\cos\left(\theta_i\right) &= \cos\left(\tilde{\theta}_i\right)\cos\left(\theta_x\right)+\sin\left(\tilde{\theta}_i\right)\cos\left(\theta_y\right),\\ \sin\left(\theta_i\right) &= \sqrt{\frac{\cos^2(\theta_z)+\cos^2\left(\theta_x\right)\sin^2(\tilde{\theta}_i)+\cos^2\left(\theta_y\right)}{\cos^2(\tilde{\theta}_i)-2\cos\left(\theta_x\right)\cos\left(\theta_y\right)\cos(\tilde{\theta}_i)\sin(\tilde{\theta}_i)}}\,.\end{aligned}$$

Please note that $\tilde{\theta}_i$ and θ_i are two different symbols. Moreover,

i) $e_i = e_x \cos\left(\tilde{\theta}_i\right) + e_y \sin\left(\tilde{\theta}_i\right)$ represents the incident electric-field vector's projection onto the ith dipole's axis.

ii) $\ell_{\theta_i} \;=\; \frac{\lambda}{\pi}\frac{1}{\sin(\pi\frac{L}{\lambda})}\frac{\cos(\pi\frac{L}{\lambda}\cos(\theta_i))-\cos(\pi\frac{L}{\lambda})}{\sin(\theta_i)}$ refers to the ith electrically long dipole's "effective length.

4.2.2 To Derive Radially Oriented Dipoles' Array Manifold

Suppose that I number of such electrically long dipoles are spaced evenly on a circle, which has a radius of R, lies on the x-y horizontal plane, and is centered at the Cartesian origin. Suppose further that these electrically long dipoles are each oriented *radially* with respect to the circle's origin, as shown in Figure 4.1.

For this entire circular array of I radially oriented and equally spaced dipoles of electrical length $\frac{L}{\lambda}$, the $I \times 1$ array manifold may be represented as

$$\mathbf{a}_{\mathrm{r}} \;=\; \begin{bmatrix} e_1\ell_{\theta_1}\csc(\theta_1)e^{j2\pi\frac{R}{\lambda}\cos(\theta_1)}\\ e_2\ell_{\theta_2}\csc(\theta_2)e^{j2\pi\frac{R}{\lambda}\cos(\theta_2)}\\ \vdots\\ e_I\ell_{\theta_I}\csc(\theta_I)e^{j2\pi\frac{R}{\lambda}\cos(\theta_I)}\end{bmatrix}. \tag{4.6}$$

This array manifold expression is new to the open literature, to the best knowledge.

4.2.3 To Derive Tangentially Oriented Dipoles' Array Manifold

Suppose the circular array's electrically long dipoles are oriented *tangentially* with respect to the circumference, as shown in Figure 4.2.

The ith such dipole's voltage would equal

$$v_i \quad = \quad e_i \ell_{\beta_i} \csc(\beta_i) e^{j2\pi \frac{R}{\lambda}\cos(\theta_i)}, \tag{4.7}$$

where β_i denotes the spatial angle between the ith dipole axis and the incident source's direction of arrival. Moreover,

$$e_i \quad = \quad e_y \cos\left(\tilde{\theta}_i\right) - e_x \sin\left(\tilde{\theta}_i\right), \tag{4.8}$$

represents the incident electric-field component along the ith dipole's axis,

$$\ell_{\beta_i} \quad = \quad \frac{\lambda}{\pi}\frac{1}{\sin(\pi\frac{L}{\lambda})}\frac{\cos(\pi\frac{L}{\lambda}\cos(\beta_i)) - \cos(\pi\frac{L}{\lambda})}{\sin(\beta_i)}, \tag{4.9}$$

symbolizes the ith electrically long dipole's effective length, and

$$\cos(\beta_i) = \cos\left(\tilde{\theta}_i\right)\cos(\theta_y) - \sin\left(\tilde{\theta}_i\right)\cos(\theta_x), \tag{4.10}$$

$$\sin(\beta_i) = \sqrt{\frac{\cos^2(\theta_z) + \cos^2(\theta_y)\sin^2(\tilde{\theta}_i) + \cos^2(\theta_x)}{\cos^2(\tilde{\theta}_i) + 2\cos(\theta_x)\cos(\theta_y)\cos(\tilde{\theta}_i)\sin(\tilde{\theta}_i)}}. \tag{4.11}$$

For the entire circular array of I tangentially oriented and equally spaced dipoles of electrical length $\frac{L}{\lambda}$, the array manifold may be represented as

$$\mathbf{a}_{\mathrm{tn}} = \begin{bmatrix} e_1 \ell_{\beta_1} \csc(\beta_1) e^{j2\pi \frac{R}{\lambda} \cos(\theta_1)} \\ e_2 \ell_{\beta_2} \csc(\beta_2) e^{j2\pi \frac{R}{\lambda} \cos(\theta_2)} \\ \vdots \\ e_I \ell_{\beta_I} \csc(\beta_I) e^{j2\pi \frac{R}{\lambda} \cos(\theta_I)} \end{bmatrix}. \tag{4.12}$$

This array manifold expression is also new to open literature, to the best knowledge.

4.3 The Data's Statistical Model

A point-size source emits a narrowband $s(t)$ from the far field. This signal is modeled as complex-value Gaussian, zero-mean with a power of σ_s^2, and statistically uncorrelated over time.

At the mth time instant, the array collects a $I \times 1$ data-vector,

$$\mathbf{z}(m) = \mathbf{a}s(m) + \mathbf{n}(m) \tag{4.13}$$

where $\mathbf{n}(m)$ denotes a zero-mean complex-value Gaussian noise vector which is uncorrelated over time and across different dipoles, as well as statistically independent from $\{s(m), \forall m\}$. The noise variance at each dipole is represented by σ_n^2. Thus, this noise process has a covariance matrix of $\mathbf{\Gamma}_0 = \sigma_n^2 \mathbf{I}_I$, where $\mathbf{I}_I$ represents an $I \times I$ identity matrix. Suppose M number of time samples are collected by the UCA giving a $I \times M$ data matrix of $\mathbf{Z}$.

The principal eigenvector of the $I \times I$ data correlation matrix, $\mathbf{Z}\mathbf{Z}^H$, equals $\hat{\mathbf{a}} \approx c\mathbf{a}$ where c is an unknown complex-value scalar. In the above, the superscript ^{H} symbolizes the hermitian operator. This vector $\hat{\mathbf{a}}$ would be used in the following subsection for direction finding and polarization estimation.

4.4 The proposed algorithm – if the diameter $2R \leq \frac{\lambda}{2}$

4.4.1 To estimate the incident source's direction-of-arrival

This section will develop a closed-form estimator of the bivariate direction-of-arrival and the bivariate polarization. The new algorithm developed below is predicated on these following new insights on the array manifolds in (4.6) and (4.12):

(i) For the two collinear dipoles hypothetically lying on the x-axis: their orientations are the same; hence, their noiseless data would be identical except for a complex phase of $\pm 2\pi \frac{R}{\lambda} \sin(\theta_z) \cos(\phi_x)$, which arises due to these dipoles' different locations. This aforementioned complex phase depends on the incident source's Cartesian direction cosine of $u = \cos(\theta_1) = \sin(\theta_z) \cos(\phi_x)$ along the x-axis.

(ii) Similarly for the two collinear dipoles hypothetically lying on the y-axis: Those two long dipoles' noiseless data would be identical except for a complex phase of $\pm 2\pi \frac{R}{\lambda} \sin(\theta_z) \sin(\phi_x)$, containing the Cartesian direction cosine of $v = \sin(\theta_z) \sin(\phi_x)$ along the y-axis.

(iii) More generally for the two collinear dipoles lying on the radial axis at an angle of $\tilde{\theta}_i$ radians with the positive x-axis: Those two long dipoles' noiseless data would be identical except for a complex phase of $\pm 2\pi \frac{R}{\lambda} \left[u \cos\left(\tilde{\theta}_i\right) + v \sin\left(\tilde{\theta}_i\right)\right]$, which is a function of x-axis and y-axis Cartesian direction cosines and $\tilde{\theta}_i$ has been defined in (4.4).

Predicated on the above insights in (i)-(iii): For the entire circular array consisting of I long dipoles, their data can afford the estimation of the values of the $\frac{I}{2}$ number of different bivariate functions,

$$\left\{ \left[u \cos\left(\tilde{\theta}_i\right) + v \sin\left(\tilde{\theta}_i\right)\right], \ \forall i = 1, 2, \cdots, \frac{I}{2} \right\}.$$

More precisely, the data can be eigen-processed to yield an estimate $\hat{\mathbf{a}}_k$, of the kth incident source's $I \times 1$ steering vector $\mathbf{a}_k$. From $\hat{\mathbf{a}}_k$, define the following $\frac{I}{2} \times 1$ vector:

$$\hat{\mathbf{b}}_k \quad := \quad \begin{bmatrix} \angle \frac{-[\hat{\mathbf{a}}_k]_1}{[\hat{\mathbf{a}}_k]_{\frac{I}{2}+1}} \\ \vdots \\ \angle \frac{-[\hat{\mathbf{a}}_k]_i}{[\hat{\mathbf{a}}_k]_{\frac{I}{2}+i}} \\ \vdots \\ \angle \frac{-[\hat{\mathbf{a}}_k]_{\frac{I}{2}}}{[\hat{\mathbf{a}}_k]_I} \end{bmatrix}, \tag{4.14}$$

In the above, $\angle$ takes the complex phase of the ensuring entity, and $[\cdot]_\tau$ denotes the τth element of the vector inside the square brackets. For UCA of radially oriented dipoles

$$[\mathbf{a}_k]_i \quad = \quad e_{i,k}\ell_{\theta_{i,k}} \csc(\theta_{i,k}) e^{j2\pi\frac{R}{\lambda}\cos(\theta_{i,k})} \tag{4.15}$$

$$\begin{aligned} [\mathbf{a}_k]_{\frac{I}{2}+i} \quad &= \quad e_{\frac{I}{2}+i,k}\ell_{\theta_{\frac{I}{2}+i,k}} \csc(\theta_{\frac{I}{2}+i,k}) e^{j2\pi\frac{R}{\lambda}\cos\left(\theta_{\frac{I}{2}+i,k}\right)} \\ &= \quad -e_{i,k}\ell_{\theta_{i,k}} \csc(\theta_{i,k}) e^{-j2\pi\frac{R}{\lambda}\cos(\theta_{i,k})} \end{aligned} \tag{4.16}$$

The above equality in (4.16) is obtained by using the definition of e_i, $\ell_{\theta_i} \csc(\theta_i)$, and $\cos(\theta_i)$. Using equations (4.15) and (4.16) in (4.14) gives

$$\hat{\mathbf{b}}_k \quad \approx \quad 4\pi\frac{R}{\lambda} \begin{bmatrix} \cos(\theta_{1,k}) \\ \vdots \\ \cos(\theta_{i,k}) \\ \vdots \\ \cos(\theta_{\frac{I}{2},k}) \end{bmatrix} = 4\pi\frac{R}{\lambda} \begin{bmatrix} u_k \\ u_k \cos\left(\tilde{\theta}_2\right) + v_k \sin\left(\tilde{\theta}_2\right) \\ \vdots \\ u_k \cos\left(\tilde{\theta}_i\right) + v_k \sin\left(\tilde{\theta}_i\right) \\ \vdots \\ u_k \cos\left(\tilde{\theta}_{\frac{I}{2}}\right) + v_k \sin\left(\tilde{\theta}_{\frac{I}{2}}\right) \end{bmatrix} \tag{4.17}$$

The above approximation becomes exact, if noises are absent or if the snapshots are infinite in number. Same result in equation (4.17) would also be obtained for UCA of tangentially oriented dipoles.

From (4.14), the x-axis Cartesian direction cosine can be estimated as

$$\hat{u}_k \quad := \quad \frac{1}{4\pi}\frac{\lambda}{R}[\hat{\mathbf{b}}_k]_1, \tag{4.18}$$

assuming that $\frac{R}{\lambda}$ is prior known.

Then, using $\hat{u}_k$ and the values from the last $\frac{I}{2}-1$ entries of (4.14), the y-axis Cartesian direction cosine can be estimated as

$$\hat{v}_k := \frac{2}{I-2}\sum_{i=2}^{I/2}\frac{\frac{1}{4\pi}\frac{\lambda}{R}[\hat{\mathbf{b}}_k]_i - \hat{u}_k\cos\left(\tilde{\theta}_i\right)}{\sin\left(\tilde{\theta}_i\right)} \tag{4.19}$$

The direction-of-arrival can be estimated using (4.18) and (4.19) as

$$\hat{\theta}_{z,k} \quad := \begin{cases} \arcsin\left(\sqrt{\hat{u}_k^2+\hat{v}_k^2}\right), & \text{if } \theta_{z,k} \in [0, \frac{\pi}{2}), \\ \pi - \arcsin\left(\sqrt{\hat{u}_k^2+\hat{v}_k^2}\right), & \text{if } \theta_{z,k} \in [\pi/2, \pi]; \end{cases} \tag{4.20}$$

$$\hat{\phi}_{x,k} \quad := \begin{cases} \arctan\left(\frac{|\hat{v}_k|}{|\hat{u}_k|}\right), & \text{if } g > 0 \ \& \ h > 0, \\ \pi - \arctan\left(\frac{|\hat{v}_k|}{|\hat{u}_k|}\right), & \text{if } g \le 0 \ \& \ h > 0, \\ \pi + \arctan\left(\frac{|\hat{v}_k|}{|\hat{u}_k|}\right), & \text{if } g \le 0 \ \& \ h \le 0, \\ 2\pi - \arctan\left(\frac{|\hat{v}_k|}{|\hat{u}_k|}\right), & \text{if } g > 0 \ \& \ h \le 0. \end{cases} \tag{4.21}$$

where $g := \operatorname{sgn}(\hat{u}_k)$ and $h := \operatorname{sgn}(\hat{v}_k)$.

The steps above have not required any prior knowledge of $\frac{L}{\lambda}$.

4.4.2 To estimate the incident source's polarization

As the dipoles' gain and spatial phase responses are independent of incident signal's polarization, they can be side-stepped for polarization estimation as follows. Define an $I \times 1$ vector

$$\hat{\mathbf{d}}_k \quad := \quad \hat{\mathbf{a}}_k \circ \begin{bmatrix} e^{-j2\pi \frac{R}{\lambda} \cos(\hat{\theta}_{1,k})} \\ \vdots \\ e^{-j2\pi \frac{R}{\lambda} \cos(\hat{\theta}_{i,k})} \\ \vdots \\ e^{-j2\pi \frac{R}{\lambda} \cos(\hat{\theta}_{I,k})} \end{bmatrix} \tag{4.22}$$

where

$$\cos(\hat{\theta}_{i,k}) \;=\; \cos\left(\tilde{\theta}_i\right) \sin(\hat{\theta}_{z,k}) \cos(\hat{\phi}_{x,k}) + \sin\left(\tilde{\theta}_i\right) \sin(\hat{\theta}_{z,k}) \sin(\hat{\phi}_{x,k}), \tag{4.23}$$

and $\circ$ denotes an element-wise multiplication.

The algorithms in Section 4.4.2 and 4.4.2 will require a prior knowledge of only $\frac{L}{\lambda}$ and $\frac{R}{\lambda}$.

For $\mathbf{a} = \mathbf{a}_{\mathrm{r}}$

Using the estimated $\hat{\theta}_{i,k}$,

$$\hat{\ell}_{\theta_{i,k}} \;=\; \frac{\cos\left(\pi \frac{L}{\lambda} \cos(\hat{\theta}_{i,k})\right) - \cos(\pi \frac{L}{\lambda})}{\sin(\hat{\theta}_{i,k})}, \tag{4.24}$$

where

$$\sin\left(\hat{\theta}_{i,k}\right) \;=\; \sqrt{\begin{array}{c} \cos^2(\hat{\theta}_{z,k}) + (\sin(\hat{\theta}_{z,k}) \cos(\hat{\phi}_{x,k}))^2 \sin^2(\tilde{\theta}_i) \\ +(\sin(\hat{\theta}_{z,k}) \sin(\hat{\phi}_{x,k}) \cos(\tilde{\theta}_i))^2 \\ -2 \sin^2(\hat{\theta}_{z,k}) \sin(\hat{\phi}_{x,k}) \cos(\hat{\phi}_{x,k}) \cos(\tilde{\theta}_i) \sin(\tilde{\theta}_i) \end{array}}\,. \tag{4.25}$$

The following algorithmic steps aim to bypass the dipoles' gain responses, in order to estimate the incident source's polarization:

$$\hat{\mathbf{g}}_{\mathrm{r}_k} \quad := \quad \hat{\mathbf{d}}_k \circ \begin{bmatrix} \sin(\hat{\theta}_{1,k})/\hat{\ell}_{\theta_{1,k}} \\ \vdots \\ \sin(\hat{\theta}_{i,k})/\hat{\ell}_{\theta_{i,k}} \\ \vdots \\ \sin(\hat{\theta}_{I,k})/\hat{\ell}_{\theta_{I,k}} \end{bmatrix} \approx \bar{c} \begin{bmatrix} e_x \\ e_x \cos\left(\tilde{\theta}_2\right) + e_y \sin\left(\tilde{\theta}_2\right) \\ \vdots \\ e_x \cos\left(\tilde{\theta}_i\right) + e_y \sin\left(\tilde{\theta}_i\right) \\ \vdots \\ e_x \cos\left(\tilde{\theta}_I\right) + e_y \sin\left(\tilde{\theta}_I\right) \end{bmatrix} \tag{4.26}$$

where

$$\bar{c} \quad := \quad \frac{\lambda}{\pi} \frac{c}{\sin(\pi \frac{L}{\lambda})}. \tag{4.27}$$

From (4.26), define

$$\begin{aligned} \alpha_1 \quad &:= \quad [\hat{\mathbf{g}}_{\mathrm{r}_k}]_1 \\ &\approx \quad \bar{c} e_x \end{aligned} \tag{4.28}$$

and

$$\begin{aligned} \alpha_2 \quad &:= \frac{1}{I-1} \sum_{i=2}^{I} \frac{\left([\hat{\mathbf{g}}_{\mathrm{r}_k}]_i - [\hat{\mathbf{g}}_{\mathrm{r}_k}]_1 \cos\left(\tilde{\theta}_i\right)\right)}{\sin\left(\tilde{\theta}_i\right)} \\ &\approx \quad \bar{c} e_y. \end{aligned} \tag{4.29}$$

The polarization can be estimated by using (4.28) and (4.29) in [125]

$$\hat{\gamma}_k \quad = \quad \arctan\left\{|\kappa|\right\}, \tag{4.30}$$

$$\hat{\eta}_k \quad = \quad \angle \kappa. \tag{4.31}$$

where

$$\kappa \quad := \quad \frac{1}{\cos(\hat{\theta}_{z,k})} \frac{\alpha_1 \cos(\hat{\phi}_{x,k}) + \alpha_2 \sin(\hat{\phi}_{x,k})}{\alpha_2 \cos(\hat{\phi}_{x,k}) - \alpha_1 \sin(\hat{\phi}_{x,k})} \tag{4.32}$$

For $\mathbf{a} = \mathbf{a}_{\mathrm{tn}}$

Using the estimated $\hat{\beta}_{i,k}$,

$$\hat{\ell}_{\beta_{i,k}} = \frac{\cos(\pi\frac{L}{\lambda}\cos(\hat{\beta}_{i,k})) - \cos(\pi\frac{L}{\lambda})}{\sin(\hat{\beta}_{i,k})}, \tag{4.33}$$

where

$$\cos(\hat{\beta}_{i,k}) = \cos\left(\tilde{\theta}_i\right)\sin(\hat{\theta}_{z,k})\sin(\hat{\phi}_{x,k}) - \sin\left(\tilde{\theta}_i\right)\sin(\hat{\theta}_{z,k})\cos(\hat{\phi}_{x,k}), \tag{4.34}$$

$$\sin(\hat{\beta}_{i,k}) = \sqrt{\begin{array}{c} \cos^2(\hat{\theta}_{z,k}) + (\sin(\hat{\theta}_{z,k})\cos(\hat{\phi}_{x,k}))^2\cos^2(\tilde{\theta}_i) \\ +(\sin(\hat{\theta}_{z,k})\sin(\hat{\phi}_{x,k})\sin(\tilde{\theta}_i))^2 \\ +2\sin^2(\hat{\theta}_{z,k})\sin(\hat{\phi}_{x,k})\cos(\hat{\phi}_{x,k})\cos(\tilde{\theta}_i)\sin(\tilde{\theta}_i) \end{array}}. \tag{4.35}$$

The following algorithmic steps aim to bypass the dipoles' gain responses, in order to estimate the incident source's polarization:

$$\hat{\mathbf{g}}_{\mathrm{tn}_k} = \hat{\mathbf{d}}_k \circ \begin{bmatrix} \sin(\hat{\beta}_{1,k})/\hat{\ell}_{\beta_{1,k}} \\ \vdots \\ \sin(\hat{\beta}_{i,k})/\hat{\ell}_{\beta_{i,k}} \\ \vdots \\ \sin(\hat{\beta}_{I,k})/\hat{\ell}_{\beta_{I,k}} \end{bmatrix} = \bar{c}\begin{bmatrix} e_y \\ e_y\cos\left(\tilde{\theta}_2\right) - e_x\sin\left(\tilde{\theta}_2\right) \\ \vdots \\ e_y\cos\left(\tilde{\theta}_i\right) - e_x\sin\left(\tilde{\theta}_i\right) \\ \vdots \\ e_y\cos\left(\tilde{\theta}_I\right) - e_x\sin\left(\tilde{\theta}_I\right) \end{bmatrix} \tag{4.36}$$

From (4.36),

$$\alpha_2 := [\hat{\mathbf{g}}_{\mathrm{tn}_k}]_1 \approx \bar{c}e_y \tag{4.37}$$

and

$$\begin{aligned} \alpha_1 &:= -\frac{1}{I-1}\sum_{i=2}^{I}\frac{\left([\hat{\mathbf{g}}_{\mathrm{tn}_k}]_i - [\hat{\mathbf{g}}_{\mathrm{tn}_k}]_1\cos\left(\tilde{\theta}_i\right)\right)}{\sin\left(\tilde{\theta}_i\right)} \\ &\approx \bar{c}e_x. \end{aligned} \tag{4.38}$$

The polarization can similarly be estimated by using (4.37) and (4.38) in (4.30) and (4.31) [125].

4.5 The proposed algorithm – the extended-aperture case of the diameter $2R > \frac{\lambda}{2}$

Consider an ith collinear pair, consisting of the ith dipole and the $\left(i + \frac{I}{2}\right)$th dipole. Their measurements (in response to kth signal incident from the Cartesian direction cosines of (u_k, v_k) and if without noise) are inter-related by a complex phase difference, which is given by the ith entry of (4.14). Under noiseless condition, the complex phase difference would become [1]

$$[\hat{\mathbf{b}}_k]_i = 4\pi \frac{R}{\lambda} \cos(\theta_{i,k}) \tag{4.39}$$

which is dependent only on $\frac{R}{\lambda}$ and $\cos(\theta_{i,k})$. As $\cos(\theta_{i,k})$ would be constant for the signal arriving through a circle around dipole axis (because all these points on circle would have same angle of $\theta_{i,k}$ between dipole axis and direction-of-arrival), therefore, the complex phase difference would remain same for signal arriving through any point on this circle for a specific value of $\frac{R}{\lambda}$. Therefore, the set of all pairs of Cartesian direction cosines $\{(u_k, v_k)\}$ giving the same complex phase difference: That set would form a circle perpendicular to the two dipoles' collinear axis.

Now, please refer to Figure 4.4. As the complex phase difference changes in value, the circle's origin would move along that collinear axis. If $2R \leq \frac{\lambda}{2}$, each of these circles would correspond to a different complex phase difference. However, as $\cos(\theta_{i,k}) \in [-1, 1]$, if $2R > \frac{\lambda}{2}$, then $[\hat{\mathbf{b}}_k]_i > |\pi|$ which would lead to cyclic ambiguity. Therefore, under sparse spacing where $2R > \frac{\lambda}{2}$, two or more circles may give the same complex phase difference as shown in Figure 4.4.

The cyclic ambiguous candidates can be written as

---

[1] $\theta_{i,k} = \arccos\left(u \cos\left(\tilde{\theta}_i\right) + v \sin\left(\tilde{\theta}_i\right)\right)$, which (by definition) equals the spatial angle between the source's direction-of-arrival and the ith dipole pair axis.

$$[\hat{\mathbf{b}}_k]_i \pm 2\pi p = 4\pi \frac{R}{\lambda} \cos(\theta_{i,k}) \tag{4.40}$$

where p is a whole integer such that $|\frac{1}{4\pi}\frac{\lambda}{R}\left(\left[\hat{\mathbf{b}}_k\right]_i \pm 2\pi p\right)| \leq 1$.

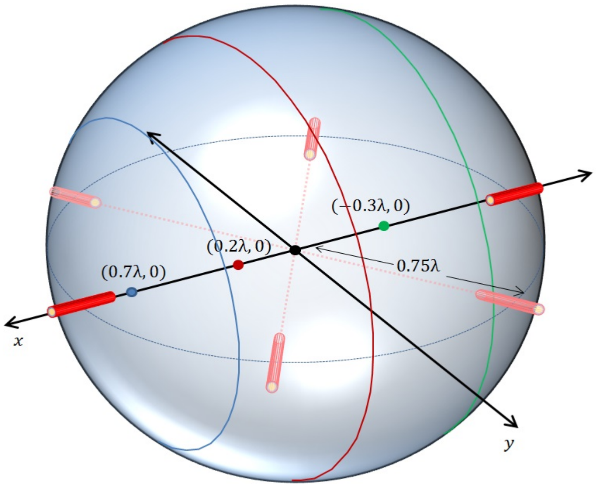

Fig. 4.4.: UCA of $M = 6$ radially oriented electrically long dipoles with small circles shown for only first dipole pair along x-axis. Here, $R/\lambda = 0.75$. The signal coming through any point on any of these three small circles would give the same complex phase difference for dipole pair along x-axis.

Once the circles centered at each collinear dipole pair are drawn, then the point of intersection of these small circles would be the arrival direction that would satisfy the complex phase difference of all dipole pairs simultaneously.

As an example, consider a UCA of six electrically long dipoles as shown in Figure 4.5. The complex phase difference of first dipole pair would be obtained for signal coming through any point on any of the two small circles centered at x-axis as shown in Figure 4.5. Similarly, the complex phase difference of second dipole pair would be obtained for signal impinging through any point on any of the two small circles centered at axis of second dipole pair. Similar trend is followed for third dipole pair as well. The actual direction-of-arrival can be determined from the point of intersection of all dipole pairs' small circles where the complex phase difference of all the dipole pairs are satisfied simultaneously.

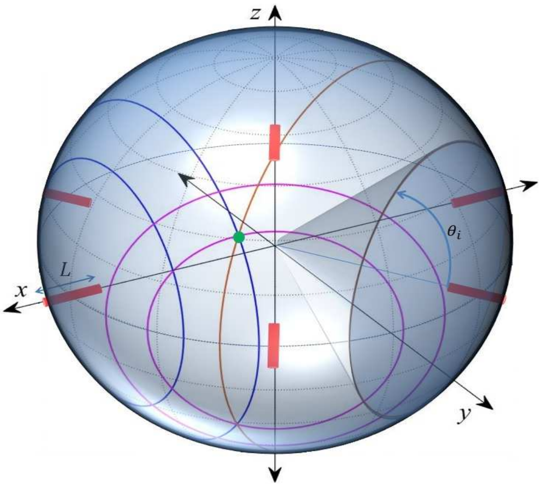

Fig. 4.5.: UCA of $M = 6$ radially oriented electrically long dipoles with small circles shown for each collinear dipole pair. Intersection point of the all the dipole pairs' circles corresponds to the actual direction of arrival.

For estimating the direction-of-arrival as mentioned above, consider the ambiguous values obtained using equation (4.40) for first entry of equation (4.14) where each value correspond to a different small circle, the corresponding Cartesian direction cosine along x-axis are obtained as

$$u_k^{(p)} \;:=\; \frac{1}{4\pi}\frac{\lambda}{R}\left(\left[\hat{\mathbf{b}}_k\right]_1 \pm 2\pi p\right). \tag{4.41}$$

Then using $u_k^{(p)}$ and ambiguous values from the second entry of (4.14), determine

$$v_k^{(p,q)} := \frac{\frac{1}{4\pi}\frac{\lambda}{R}([\hat{\mathbf{b}}_k]_2 \pm 2\pi q) - u_k^{(p)}\cos(\tilde{\theta}_2)}{\sin(\tilde{\theta}_2)} \tag{4.42}$$

where q is an integer such that $|\frac{1}{4\pi}\frac{\lambda}{R}(\left[\hat{\mathbf{b}}_k\right]_2 \pm 2\pi q)| \leq 1$.

The PQ entries in $\left\{\left(u_k^{(p)}, v_k^{(p,q)}\right)\right\}$ constitute all candidates giving the complex phase difference of first two collinear dipole pair and these candidates correspond to the points of intersection of the small circles centered at

x-axis and radial line at an angle of $\frac{2\pi}{I}$ counterclockwise with respect to positive x-axis.

It can be seen from (4.17) that

$$\hat{\mathbf{b}}_k(3:\frac{I}{2}) \approx \angle \begin{bmatrix} e^{j4\pi\frac{R}{\lambda}\left(u_k\cos\left(\tilde{\theta}_3\right)+v_k\sin\left(\tilde{\theta}_3\right)\right)} \\ \vdots \\ e^{j4\pi\frac{R}{\lambda}\left(u_k\cos\left(\tilde{\theta}_i\right)+v_k\sin\left(\tilde{\theta}_i\right)\right)} \\ \vdots \\ e^{j4\pi\frac{R}{\lambda}\left(u_k\cos\left(\tilde{\theta}_{\frac{I}{2}}\right)+v_k\sin\left(\tilde{\theta}_{\frac{I}{2}}\right)\right)} \end{bmatrix}$$

$$= 4\pi\frac{R}{\lambda}\begin{bmatrix} u_k\cos\left(\tilde{\theta}_3\right)+v_k\sin\left(\tilde{\theta}_3\right) \\ \vdots \\ u_k\cos\left(\tilde{\theta}_i\right)+v_k\sin\left(\tilde{\theta}_i\right) \\ \vdots \\ u_k\cos\left(\tilde{\theta}_{\frac{I}{2}}\right)+v_k\sin\left(\tilde{\theta}_{\frac{I}{2}}\right) \end{bmatrix}. \tag{4.43}$$

where $(3:\frac{I}{2})$ denotes 3rd to $\frac{I}{2}$th entries of the vector $\hat{\mathbf{b}}_k$. In order to see if $u_k^{(p)}$ and $v_k^{(p,q)}$ satisfy the above equation (4.43), define

$$\mathbf{w}^{(p,q)} := \angle \begin{bmatrix} e^{j4\pi\frac{R}{\lambda}\left(u_k^{(p)}\cos\left(\tilde{\theta}_3\right)+v_k^{(p,q)}\sin\left(\tilde{\theta}_3\right)\right)} \\ \vdots \\ e^{j4\pi\frac{R}{\lambda}\left(u_k^{(p)}\cos\left(\tilde{\theta}_i\right)+v_k^{(p,q)}\sin\left(\tilde{\theta}_i\right)\right)} \\ \vdots \\ e^{j4\pi\frac{R}{\lambda}\left(u_k^{(p)}\cos\left(\tilde{\theta}_{\frac{I}{2}}\right)+v_k^{(p,q)}\sin\left(\tilde{\theta}_{\frac{I}{2}}\right)\right)} \end{bmatrix} \tag{4.44}$$

If the two vectors $\hat{\mathbf{b}}(3:\frac{I}{2})$ and $\mathbf{w}^{(p,q)}$ are parallel at the value of $u_k^{(p)}$ and $v_k^{(p,q)}$, then the direction cosines $u_k^{(p)}$ and $v_k^{(p,q)}$ satisfy the complex phase difference of all the $\frac{I}{2}$ dipole pairs which can be established mathematically using

$$\left(\hat{u}_k^{(p)}, \hat{v}_k^{(p,q)}\right) \quad := \quad \underset{(u^{(p)},v^{(p,q)})}{\arg} \; \max \left(\frac{|\hat{\mathbf{b}}_k(3:\frac{I}{2}) \cdot \mathbf{w}^{(p,q)}|}{\left\|\hat{\mathbf{b}}_k(3:\frac{I}{2})\right\| \cdot \|\mathbf{w}^{(p,q)}\|} \right) \tag{4.45}$$

where $\|\cdot\|$ denotes the Frobenius norm of the vector inside.

The set of Cartesian direction cosine pairs obtained from (4.45) can be used to determine the ambiguous directions-of-arrival as

$$\hat{\theta}_{z,k}^{(p,q)} \quad := \quad \begin{cases} \arcsin\left(\sqrt{\left(\hat{u}_k^{(p)}\right)^2 + \left(\hat{v}_k^{(p,q)}\right)^2}\right), & \text{if } \theta_{z,k} \in [0, \frac{\pi}{2}), \\ \pi - \arcsin\left(\sqrt{\left(\hat{u}_k^{(p)}\right)^2 + \left(\hat{v}_k^{(p,q)}\right)^2}\right), & \text{if } \theta_{z,k} \in [\pi/2, \pi]; \end{cases} \tag{4.46}$$

$$\hat{\phi}_{x,k}^{(p,q)} \quad := \quad \begin{cases} \arctan\left(\frac{|\hat{v}_k^{(p,q)}|}{|\hat{u}_k^{(p)}|}\right), & \text{if } g > 0 \;\&\; h > 0, \\ \pi - \arctan\left(\frac{|\hat{v}_k^{(p,q)}|}{|\hat{u}_k^{(p)}|}\right), & \text{if } g \leq 0 \;\&\; h > 0, \\ \pi + \arctan\left(\frac{|\hat{v}_k^{(p,q)}|}{|\hat{u}_k^{(p)}|}\right), & \text{if } g \leq 0 \;\&\; h \leq 0, \\ 2\pi - \arctan\left(\frac{|\hat{v}_k^{(p,q)}|}{|\hat{u}_k^{(p)}|}\right), & \text{if } g > 0 \;\&\; h \leq 0. \end{cases} \tag{4.47}$$

where $g := \operatorname{sgn}(\hat{u}_k^{(p)})$ and $h := \operatorname{sgn}(\hat{v}_k^{(p,q)})$.

The dipoles' gain/phase responses contain no information on the incident signal's polarization; hence, they may be side-stepped in the subsequent estimators of the incident source's polarization. In order to get rid of the dipoles' gain/phase responses, define $\cos(\hat{\theta}_{i,k}^{(p,q)})$ similar to (4.23) and form an $I \times 1$ vector of

$$\hat{\mathbf{d}}_k \quad := \quad \hat{\mathbf{a}}_k \circ \begin{bmatrix} e^{-j2\pi\frac{R}{\lambda}\cos(\hat{\theta}_{1,k}^{(p,q)})} \\ \vdots \\ e^{-j2\pi\frac{R}{\lambda}\cos(\hat{\theta}_{i,k}^{(p,q)})} \\ \vdots \\ e^{-j2\pi\frac{R}{\lambda}\cos(\hat{\theta}_{I,k}^{(p,q)})} \end{bmatrix}. \tag{4.48}$$

For $\mathbf{a} = \mathbf{a}_{\mathrm{r}}$

Define $\hat{\ell}^{(p,q)}_{\theta_{i,k}}$ similar to (4.24).

In order to algorithmically bypass the dipoles' gain responses, define

$$\hat{\mathbf{g}}_{\mathrm{r}_k} := \hat{\mathbf{d}}_k \circ \begin{bmatrix} \sin(\hat{\theta}^{(p,q)}_{1,k})/\hat{\ell}^{(p,q)}_{\theta_{1,k}} \\ \vdots \\ \sin(\hat{\theta}^{(p,q)}_{i,k})/\hat{\ell}^{(p,q)}_{\theta_{i,k}} \\ \vdots \\ \sin(\hat{\theta}^{(p,q)}_{I,k})/\hat{\ell}^{(p,q)}_{\theta_{I,k}} \end{bmatrix} \approx \bar{c} \begin{bmatrix} e_x \\ e_x \cos\left(\tilde{\theta}_2\right) + e_y \sin\left(\tilde{\theta}_2\right) \\ \vdots \\ e_x \cos\left(\tilde{\theta}_i\right) + e_y \sin\left(\tilde{\theta}_i\right) \\ \vdots \\ e_x \cos\left(\tilde{\theta}_I\right) + e_y \sin\left(\tilde{\theta}_I\right) \end{bmatrix}. \tag{4.49}$$

From (4.49), define

$$\alpha_1 \quad := \quad [\hat{\mathbf{g}}_{\mathrm{r}_k}]_1 \approx \bar{c} e_x \tag{4.50}$$

and

$$\alpha_2 \quad := \frac{1}{I-1} \sum_{i=2}^{I} \frac{[\hat{\mathbf{g}}_{\mathrm{r}_k}]_i - [\hat{\mathbf{g}}_{\mathrm{r}_k}]_1 \cos\left(\tilde{\theta}_i\right)}{\sin\left(\tilde{\theta}_i\right)} \approx \bar{c} e_y. \tag{4.51}$$

The polarization can be estimated by substituting (4.50) and (4.51) in [125]

$$\hat{\gamma}^{(p,q)}_k = \arctan\left\{|\kappa|\right\}, \tag{4.52}$$

$$\hat{\eta}^{(p,q)}_k \quad = \quad \angle\left\{\kappa\right\}. \tag{4.53}$$

where

$$\kappa = \frac{1}{\cos(\theta_{z,k}^{(p,q)})} \frac{\alpha_1 \cos(\phi_{x,k}^{(p,q)}) + \alpha_2 \sin(\phi_{x,k}^{(p,q)})}{\alpha_2 \cos(\phi_{x,k}^{(p,q)}) - \alpha_1 \sin(\phi_{x,k}^{(p,q)})} \tag{4.54}$$

To disambiguate among the quadruplets in $\left\{\left(\hat{\theta}_{z,k}^{(p,q)}, \hat{\phi}_{x,k}^{(p,q)}, \hat{\gamma}_k^{(p,q)}, \hat{\eta}_k^{(p,q)}\right), \forall p, q\right\}$, define

$$\begin{aligned}
(p^\circ, q^\circ) &= \underset{(p,q)}{\arg\max} \left(\frac{|\hat{\mathbf{a}}_k \cdot \bar{\mathbf{a}}^{(p,q)}|}{\|\hat{\mathbf{a}}_k\| \cdot \|\bar{\mathbf{a}}^{(p,q)}\|} \right) && (4.55)\\
(\hat{\theta}_z, \hat{\phi}_x, \hat{\gamma}, \hat{\eta}) &= (\hat{\theta}_{z,k}^{(p^\circ,q^\circ)}, \hat{\phi}_{x,k}^{(p^\circ,q^\circ)}, \hat{\gamma}_k^{(p^\circ,q^\circ)}, \hat{\eta}_k^{(p^\circ,q^\circ)}) && (4.56)
\end{aligned}$$

where $\bar{\mathbf{a}}^{(p,q)}$ is the ambiguous array manifold at values of $(\theta_{z,k}, \phi_{x,k}, \gamma_k, \eta_k) = (\hat{\theta}_{z,k}^{(p,q)}, \hat{\phi}_{x,k}^{(p,q)}, \hat{\gamma}_k^{(p,q)}, \hat{\eta}_k^{(p,q)})$ obtained from (4.6) for UCA of radially outward directed dipoles. The entity inside brackets in (4.55) would be maximized if the two vectors $\hat{\mathbf{a}}_k$ and $\bar{\mathbf{a}}$ are parallel.

For $\mathbf{a} = \mathbf{a}_{\text{tn}}$

Define $\hat{\ell}_{\beta_{i,k}}^{(p,q)}$ similar to (4.33). To cancel the effect of dipoles' gain response

$$\hat{\mathbf{g}}_{\text{tn}_k} = \hat{\mathbf{d}}_k \circ \begin{bmatrix} \sin(\hat{\beta}_{1,k}^{(p,q)})/\hat{\ell}_{\beta_{1,k}}^{(p,q)} \\ \vdots \\ \sin(\hat{\beta}_{i,k}^{(p,q)})/\hat{\ell}_{\beta_{i,k}}^{(p,q)} \\ \vdots \\ \sin(\hat{\beta}_{I,k}^{(p,q)})/\hat{\ell}_{\beta_{I,k}}^{(p,q)} \end{bmatrix} = \bar{c} \begin{bmatrix} e_y \\ e_y \cos\left(\tilde{\theta}_2\right) - e_x \sin\left(\tilde{\theta}_2\right) \\ \vdots \\ e_y \cos\left(\tilde{\theta}_i\right) - e_x \sin\left(\tilde{\theta}_i\right) \\ \vdots \\ e_y \cos\left(\tilde{\theta}_I\right) - e_x \sin\left(\tilde{\theta}_I\right) \end{bmatrix} \tag{4.57}$$

From (4.57),

$$\alpha_2 \quad := \quad \left[\hat{\mathbf{g}}_{\mathrm{tn}_k}\right]_1 \approx \bar{c}e_y \tag{4.58}$$

and

$$\begin{aligned}\alpha_1 \quad &:= \quad -\frac{1}{I-1}\sum_{i=2}^{I}\frac{\left(\left[\hat{\mathbf{g}}_{\mathrm{tn}_k}\right]_i - \left[\hat{\mathbf{g}}_{\mathrm{tn}_k}\right]_1 \cos\left(\tilde{\theta}_i\right)\right)}{\sin\left(\tilde{\theta}_i\right)} \\ &\approx \quad \bar{c}e_x. \end{aligned} \tag{4.59}$$

The polarization can similarly be estimated by using (4.58) and (4.59) in (4.52) and (4.53).

To disambiguate among the quadruplets in $\left\{\left(\theta_{z,k}^{(p,q)}, \phi_{x,k}^{(p,q)}, \gamma_k^{(p,q)}, \eta_k^{(p,q)}\right), \forall p, q\right\}$, define

$$(p^\circ, q^\circ) \quad = \quad \underset{(p,q)}{\arg\max}\left(\frac{\left|\hat{\mathbf{a}}_k \cdot \bar{\mathbf{a}}^{(p,q)}\right|}{\|\hat{\mathbf{a}}_k\| \cdot \|\bar{\mathbf{a}}^{(p,q)}\|}\right) \tag{4.60}$$

$$(\hat{\theta}_{z,k}, \hat{\phi}_{x,k}, \hat{\gamma}_k, \hat{\eta}_k) \quad = \quad (\hat{\theta}_{z,k}^{(p^\circ,q^\circ)}, \hat{\phi}_{x,k}^{(p^\circ,q^\circ)}, \hat{\gamma}_k^{(p^\circ,q^\circ)}, \hat{\eta}_k^{(p^\circ,q^\circ)}) \tag{4.61}$$

where $\bar{\mathbf{a}}^{(p,q)}$ is the ambiguous array manifold at values of $(\theta_{z,k}, \phi_{x,k}, \gamma_k, \eta_k) = (\hat{\theta}_{z,k}^{(p,q)}, \hat{\phi}_{x,k}^{(p,q)}, \hat{\gamma}_k^{(p,q)}, \hat{\eta}_k^{(p,q)})$ obtained from (4.12) for UCA of tangential horizontally oriented dipoles. The entity inside brackets in (4.60) would be maximized if the two vectors $\hat{\mathbf{a}}_k$ and $\bar{\mathbf{a}}$ are parallel.

4.6 Monte Carlo Simulations, with the Dipoles Oriented Radially

Monte Carlo experiments are conducted here for case of the electrically long dipoles oriented radially, in order to verify efficacy of the estimators in Section 4.4.

The results are shown in Figures 4.6-4.7 and compared against the Cramér-Rao bound (CRB), which has been derived in Appendix D.

These experiments show influences of electrical length $\frac{L}{\lambda}$ and the circular aperture $\frac{R}{\lambda}$ on the performance of estimators. In these numerical examples, $\theta_z = 30°$, $\phi_x = 40°$, $\gamma = 80°$, $\eta = 75°$, $I = 8$, $M = 90$, and SNR$=20$dB. Each icon on every graph represents $1,000$ independent Monte Carlo experiments. It can be seen that the performance improves by increasing the dipoles' electrical length $\frac{L}{\lambda}$ and/or the circular aperture $\frac{2R}{\lambda}$.

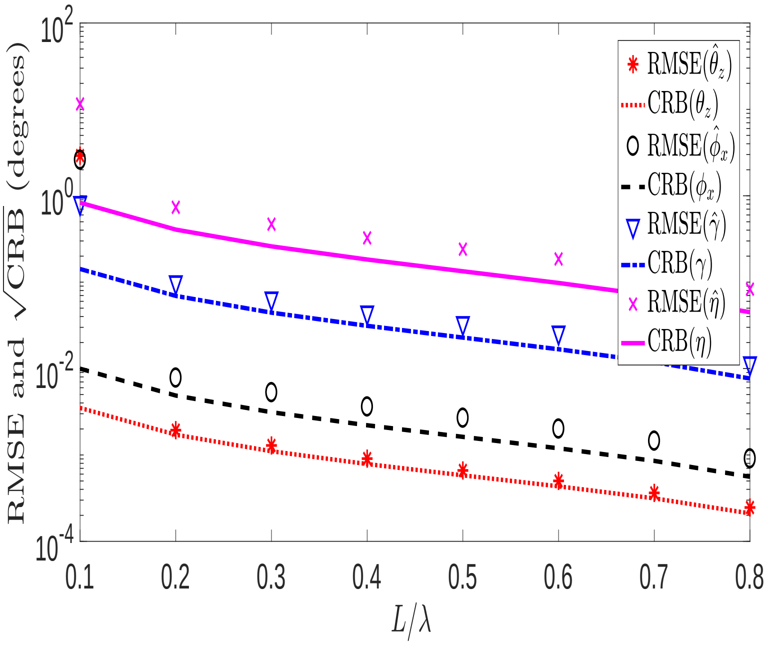

Fig. 4.6.: The proposed estimator's RMSE and $\sqrt{\text{CRB}}$, versus $\frac{L}{\lambda}$, at $\frac{R}{\lambda} = 10$.

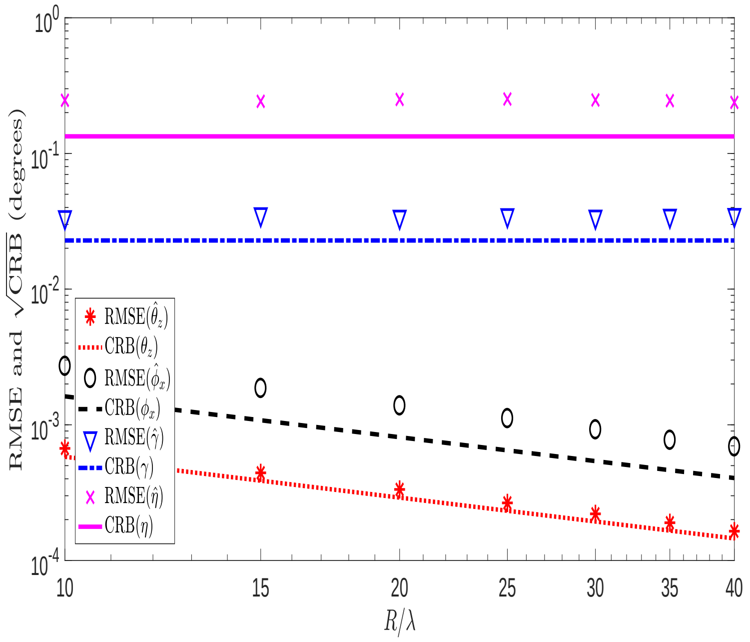

Fig. 4.7.: The proposed estimator's RMSE and $\sqrt{\text{CRB}}$, versus $\frac{R}{\lambda}$, at $\frac{L}{\lambda} = \frac{1}{2}$.

4.7 Monte Carlo Simulations for Direction Finding using Tangentially Oriented UCA

Monte Carlo experiments are performed using tangentially oriented UCA of electrically long dipoles to verify efficacy of estimators proposed in Section 4.4. The results are shown in Figures 4.8-4.9 and compared against the Cramér-Rao Bounds (CRB) as derived in Appendix D.

These experiments show influences of electrical length $\frac{L}{\lambda}$ and UCA aperture $\frac{R}{\lambda}$ on the performance of estimators. In these numerical examples, $\theta_z = 30^\circ$, $\phi_x = 60^\circ$, $\gamma = 45^\circ$, $\eta = 50^\circ$, $I = 8$, $M = 90$, and SNR$= 20$dB. Each icon on every graph represents $1,000$ independent Monte Carlo experiments. It can be seen that the performance improves by increasing dipoles' electrical length and/or UCA aperture.

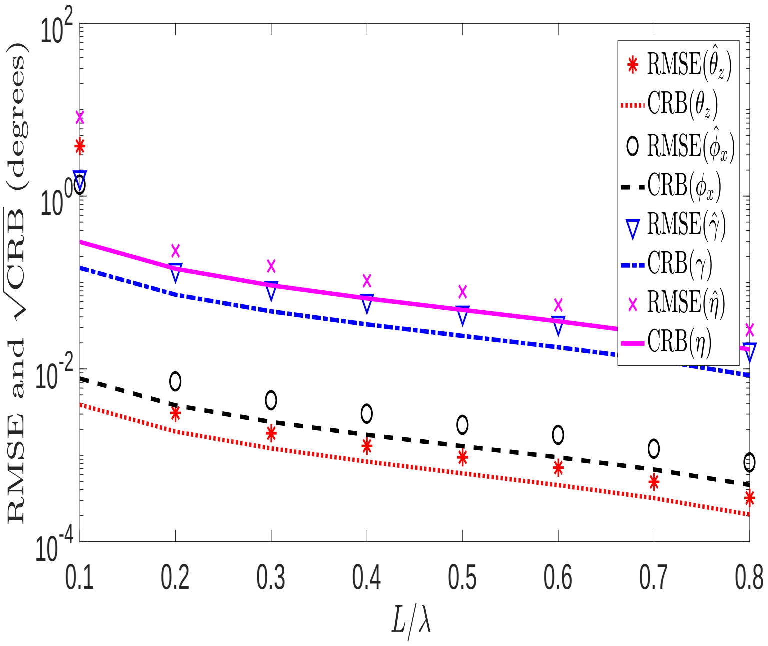

Fig. 4.8.: The proposed estimator's RMSE and $\sqrt{\text{CRB}}$, versus $\frac{L}{\lambda}$, at $\frac{R}{\lambda} = 10$.

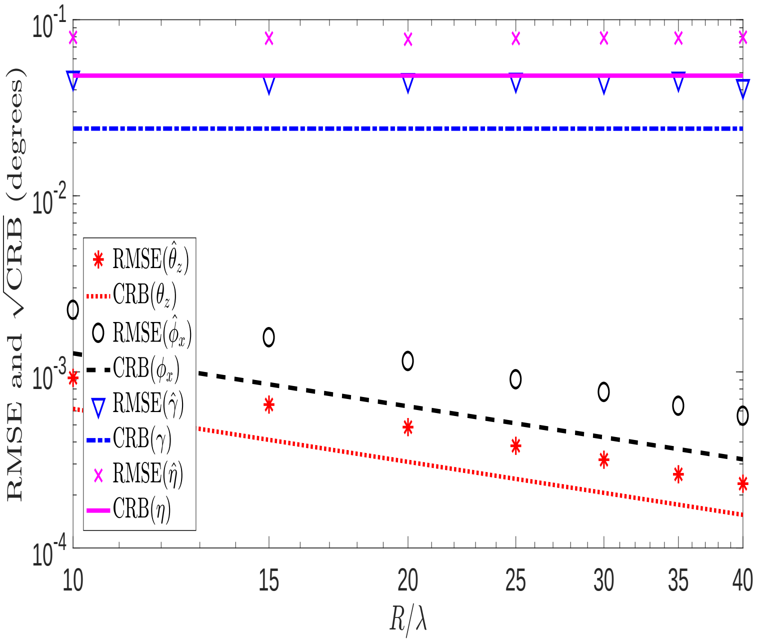

Fig. 4.9.: The proposed estimator's RMSE and $\sqrt{\text{CRB}}$, versus $\frac{R}{\lambda}$, at $\frac{L}{\lambda} = \frac{1}{2}$.

4.8 Conclusion

For a uniform circular array of electrically “long" dipoles that can realize an extended aperture to enhance the array’s spatial resolution of incident sources, this investigation is first in the open literature to propose closed-form algorithms to estimate an impinging signal’s azimuth-elevation direction and the incident bivariate polarization despite the diverse orientation of the dipoles. The proposed estimators in this chapter can closely approach the Cramér-Rao bounds, as shown in the presented Monte Carlo simulations.

5

Electrically Long Dipoles in a Crossed Pair for Closed-Form Estimation of an Incident Source's Polarization

5.1 Introduction

Polarimetry measures and interprets the polarization of transverse waves [94]. The polarization of an impinging wave may reveal the emitter's intrinsic attributes. Polarization is bivariate; therefore, at least two differently polarized antennas are required for polarimetry of any wavefield that is fully polarized.

Polarimetry via orthogonally oriented electric dipoles – this has been much investigated. Please refer to [62, 93, 125] for surveys of this literature. These references, however, focus on electrically short dipoles, which are inefficient antennas. At an electrical length of $\frac{L}{\lambda} = \frac{1}{10}$, an electrically short dipole's radiation efficiency is only 74%, whereas an electrically long half-wavelength dipole offers 95%.[1] For a perpendicular pair of such electrically long dipoles, this Chapter is first to advance any closed-form formula to estimate an incident wavefield's polarization.

Section 5.3 will provide closed-form formulas for polarization estimation. Section 5.4 will derive and will compare the corresponding Cramér-Rao lower bounds in polarization-estimation for these three dipole-orientations.

---

[1] These values are computed based on the radiation resistance equations and the loss resistance equations in [68, pp. 86, 177, 215], [95].

5.2 The Two Electrically Long Dipoles' Array Manifold

Consider a fully polarized electromagnetic wave. Its electric-field vector may be characterized (equations (2.5)-(2.8) and (2.11)-(2.12) in [96]) in the Cartesian coordinates as

$$\begin{aligned}\mathbf{e} &= \begin{bmatrix} e_x \\ e_y \\ e_z \end{bmatrix} \\ &= \underbrace{\begin{bmatrix} \cos(\phi_x)\cos(\theta_z) & -\sin(\phi_x) \\ \sin(\phi_x)\cos(\theta_z) & \cos(\phi_x) \\ -\sin(\theta_z) & 0 \end{bmatrix}}_{\overset{\text{def}}{=}\boldsymbol{\Theta}} \underbrace{\begin{bmatrix} \sin(\gamma)\, e^{j\eta} \\ \cos(\gamma) \end{bmatrix}}_{\overset{\text{def}}{=}\mathbf{p}}, \end{aligned} \tag{5.1}$$

where $\theta_z \in [0, \pi]$ denotes the transmitter's polar angle measured from the positive z-axis, $\phi_x \in [0, 2\pi)$ signifies the azimuth angle measured from the positive x-axis, $\eta \in [-\pi, \pi)$ refers to the polarization phase difference, and $\gamma \in [0, \pi/2)$ symbolizes the auxiliary polarization angle. Note that the vector $\mathbf{p}$ depends only on the polarization state of incident source, whereas the matrix $\boldsymbol{\Theta}$ depends only on the direction-of-arrival of incident source.

Consider an electrically long dipole of physical length L but an "electrical length" of $\frac{L}{\lambda} > \frac{1}{10}$, If this dipole is aligned along the z-axis, its measurement would *not* be e_z, but $e_z \ell_z^{(L)} \csc(\theta_z)$. Here, the scalar $\ell_z^{(L)}$ symbolizes the amplitude of "effective length" (a.k.a. the "effective height") and is given in [68] (equation (2-92) on p. 88, and equation (4-62a) on p. 153):

$$\ell_z^{(L)} = \frac{\lambda}{\pi} \frac{\cos\left(\pi \frac{L}{\lambda} \cos\left(\theta_z\right)\right) - \cos\left(\pi \frac{L}{\lambda}\right)}{\sin\left(\theta_z\right) \sin(\pi \frac{L}{\lambda})}. \tag{5.2}$$

Likewise, the x-oriented long dipole's measured voltage equals $e_x \ell_x^{(L)} \csc(\theta_x)$, where the scalar

$$\ell_x^{(L)} = \frac{\lambda}{\pi} \frac{\cos\left(\pi \frac{L}{\lambda} \cos\left(\theta_x\right)\right) - \cos\left(\pi \frac{L}{\lambda}\right)}{\sin\left(\theta_x\right) \sin(\pi \frac{L}{\lambda})}, \tag{5.3}$$

with $\theta_x \in [0, \pi]$ denoting the angle measured between the positive x-axis and negative of the impinging wave's propagation direction.

Similarly for a y-oriented long dipole, its voltage equals $e_y \ell_y^{(L)} \csc(\theta_y)$, with the scalar

$$\ell_y^{(L)} = \frac{\lambda}{\pi} \frac{\cos\left(\pi \frac{L}{\lambda} \cos\left(\theta_y\right)\right) - \cos\left(\pi \frac{L}{\lambda}\right)}{\sin\left(\theta_y\right) \sin(\pi \frac{L}{\lambda})}, \tag{5.4}$$

where $\theta_y \in [0, \pi]$ denotes the angle measured between the positive y-axis and negative of the incident wave's propagation direction.

The above-defined spatial angles are shown in Figure 1.3. The trigonometric relationships among the spatial angles are given in Section 1.2.

If a pair of orthogonally crossed dipoles are oriented along any two of the three Cartesian coordinates, there would exist $\begin{pmatrix} 3 \\ 2 \end{pmatrix} = 3$ possible spatial configurations: an x-y biaxial pair, an x-z biaxial pair, or an y-z biaxial pair. Their spatial geometries are shown in Figure 5.1. A proper choice of orientation could critically determine the effectiveness of polarimetry. These 3 configurations will be analytically compared in this Chapter.

Within each pair of dipoles: Suppose that the first dipole is located at the Cartesian origin (without loss of generality). Suppose also that the other dipole is placed at a known location of $(\Delta_x, \Delta_y, \Delta_z)$. Then, a spatial phase-factor of $e^{j\chi}$ would exist between these two antennas, where $\chi := 2\pi \left[\frac{\Delta_x}{\lambda} \sin(\theta_z) \sin(\phi_x) + \frac{\Delta_y}{\lambda} \sin(\theta_z) \cos(\phi_x) + \frac{\Delta_z}{\lambda} \cos(\theta_z)\right]$. Spatial collocation occurs if $(\Delta_x, \Delta_y, \Delta_z) = (0, 0, 0)$, obviously. [2]

---

[2] If the location of two dipoles are switched, $e^{j\chi}$ need to be replaced by $e^{-j\chi}$ in the array manifold; and the estimators may be modified accordingly. However, the Cramér-Rao bounds would remain unaffected.

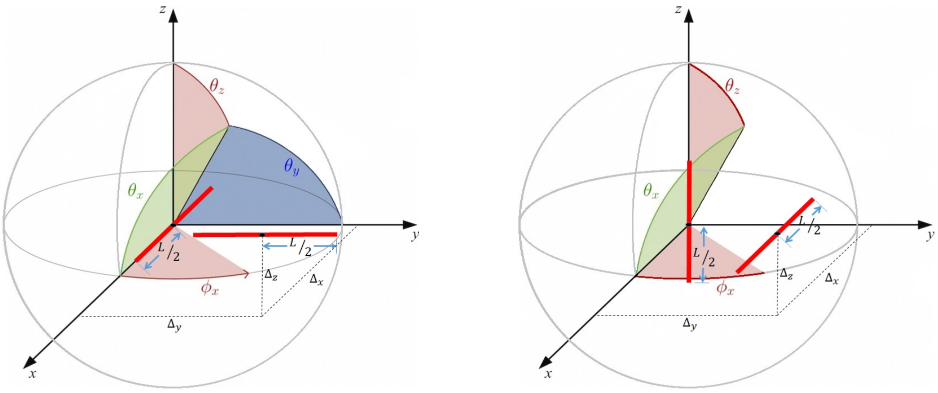

(a) The x-y dipole pair.

(b) The x-z dipole pair.

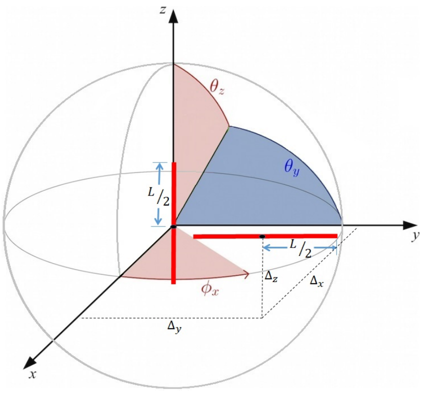

(c) The y-z dipole pair.

Fig. 5.1.: RMSE and $\sqrt{\text{CRB}}$ for $\hat{\theta}_z$ and $\hat{\phi}_x$ versus $\frac{L}{\lambda}$ using dipole triad.

Each aforementioned configuration would have its own 2×1 array manifold, but all three array manifolds may be expressed compactly through this one equation [97]:

$$\mathbf{a} \quad = \quad \overbrace{\begin{bmatrix} 1 & 0 \\ 0 & e^{j\chi} \end{bmatrix}}^{\mathbf{D} :=} \mathbf{S}\,\mathbf{e} \circ \overbrace{\begin{bmatrix} \ell_x^{(L)} \\ \ell_y^{(L)} \\ \ell_z^{(L)} \end{bmatrix} \circ \begin{bmatrix} \csc(\theta_x) \\ \csc(\theta_y) \\ \csc(\theta_z) \end{bmatrix}}^{\mathbf{a}^{(L)} :=} . \tag{5.5}$$

where S represents a 2×3 selection-matrix which has a "1" on each row but zeroes elsewhere, and $\circ$ denotes element-by-element multiplication.

A relationship exists between the x-z and the y-z configuration:

$$\mathbf{a}_{y,z}(\theta_z, \phi_x, \gamma, \eta) \quad = \quad \mathbf{a}_{x,z}\left(\theta_z, \phi_x - \frac{\pi}{2}, \gamma, \eta\right) . \tag{5.6}$$

5.3 The Polarization-Estimation Formulas for All 3 Orientation Configurations

The following presents one sample scenario where the incident source's direction-of-arrival is already known but only its polarization needs to be estimated. A high-resolution radar (HRR) system is in a "locked on" mode onto a target. Hence, the direction-of-arrival is approximately known to the radar receiver. The radar returns' polarization would aid (i) the classification of the target into specific categories (an F-16 jet versus an MiG jet versus others) based on prior polarimetric templates, or (ii) the estimation of the target's shape or material construction.

Eigen-based parameter-estimation algorithms typically involve an intermediate step, that estimates steering vector of each incident source, correct to within a complex-value scalar c which is unknown to the algorithm. That is, for each incident source[3], the estimate of $\hat{\mathbf{a}} \approx c\mathbf{a}$ is available, from which bivariate polarization (γ, η) is to be estimated. (Under noiseless or asymptotic cases, this approximation approaches equality.) Hence, there exist two scalar equations and two unknowns. The estimation formulas of $\hat{\gamma}$ and $\hat{\eta}$ can be obtained from algebraic manipulation of the two scalar equations. For example, consider the x-y crossed-dipole pair (i.e. configuration 1 of Table 5.1). The two scalar equations are the two rows of

$$\hat{\mathbf{a}} \;=\; c \begin{bmatrix} 1 & 0 \\ 0 & e^{j2\pi(\frac{\Delta x}{\lambda}\sin\theta_z \sin\phi_x + \frac{\Delta y}{\lambda}\sin\theta_z\cos\phi_x + \frac{\Delta z}{\lambda}\cos\theta_z)} \end{bmatrix} \begin{bmatrix} 1 & 0 & 0 \\ 0 & 1 & 0 \end{bmatrix} \mathbf{a}^{(L)}. \tag{5.7}$$

The two scalar unknowns are γ and η, but with $\frac{\Delta_x}{\lambda}, \frac{\Delta_y}{\lambda}, \frac{\Delta_z}{\lambda}, \frac{L}{\lambda}, \theta_z$, and ϕ_x already known.

Tables 5.1 and 5.2 lists the $\hat{\gamma}$ and $\hat{\eta}$ estimation formulas, respectively, for each of the 3 antenna configurations/orientations of Figure 5.1. These estimation-formulas, to the best knowledge, are new to the open literature. These formulas degenerate to those for the short dipoles in [125].

---

[3] This does NOT assume that only one source is incident upon the receiver. There could be many sources and these multiple incident sources could be broadband, cross-correlated, and/or time-varying.

Table 5.1.: Polarization (γ) Estimators of the 3 Dipole-Pair Configurations

Dipole Pair	$\hat{\gamma} =$
x-y	$\tan^{-1}\left\lvert \frac{1}{\cos(\theta_z)} \frac{\left[[\hat{\mathbf{a}}]_1 \ell_y^{(L)} \csc(\theta_y)\cos(\phi_x) + [\hat{\mathbf{a}}]_2 \ell_x^{(L)} \csc(\theta_x)\sin(\phi_x) e^{-j\chi}\right]}{\left[[\hat{\mathbf{a}}]_2 \ell_x^{(L)} \csc(\theta_x)\cos(\phi_x) e^{-j\chi} - [\hat{\mathbf{a}}_1] \ell_y^{(L)} \csc(\theta_y)\sin(\phi_x)\right]} \right\rvert$
x-z	$\tan^{-1}\left\lvert \frac{[\hat{\mathbf{a}}]_2 \ell_x^{(L)} \csc(\theta_x)\sin(\phi_x) e^{-j\chi}}{[\hat{\mathbf{a}}]_1 \ell_z^{(L)} \csc(\theta_z)\sin(\theta_z) + [\hat{\mathbf{a}}_2] \ell_x^{(L)} \csc(\theta_x)\cos(\phi_x)\cos(\theta_z) e^{-j\chi}} \right\rvert$
y-z	$\tan^{-1}\left\lvert \frac{-[\hat{\mathbf{a}}]_2 \ell_y^{L} \csc(\theta_y)\cos(\phi_x) e^{-j\chi}}{[\hat{\mathbf{a}}]_1 \ell_z^{(L)} \csc(\theta_z)\sin(\theta_z) + [\hat{\mathbf{a}}]_2 \ell_y^{L} \csc(\theta_y)\sin(\phi_x)\cos(\theta_z) e^{-j\chi}} \right\rvert$

These estimators are applicable for the entire validity-region of $\gamma \in [0, \frac{\pi}{2})$ and $\eta \in [-\pi, \pi)$, i.e. over the entire Poincare sphere. These estimators are also valid for $\theta \in [0, \pi]$ and $\phi \in [0, 2\pi]$ except $\theta_z = 90^\circ$ for the x-y pair, except $\phi_x = \{0^\circ, 180^\circ\}$ for the x-z pair, and except $\phi_x = \{90^\circ, 270^\circ\}$ for the y-z pair. These discrete values of the direction-of-arrival are excluded due to the underlying electromagnetics, not due to these algorithms themselves – if the emitter and the dipoles' axes are all coplanar, the two dipoles can only receive one component of the incident electric field, hence inviable to estimate this electric field's bivariate polarization. These validity regions also degenerate to those for the short dipoles in [125].

5.4 Cramér-Rao Bounds, CRB(γ) and CRB(η), for All 3 Antenna/Orientation Configurations of Section 5.3

To avoid unnecessary distraction from the present investigation on how a long electrical length would influence the cross-dipoles' polarization estimation performance, a simple statistical data model will be employed here for Cramér-Rao bound derivation. More complicated signal-and-noise scenarios can follow the approach here.

Table 5.2.: Polarization (η) Estimators of the 3 Dipole-Pair Configurations

Dipole Pair	$\hat{\eta} =$
x-y	$\angle \left\{ \frac{\begin{array}{c} [\hat{\mathbf{a}}]_1 \ell_y^{(L)} \csc(\theta_y) \cos(\phi_x) \cos(\chi) + [\hat{\mathbf{a}}]_2 \ell_x^{(L)} \csc(\theta_x) \sin(\phi_x) \\ +j [\hat{\mathbf{a}}]_1 \ell_y^{(L)} \csc(\theta_y) \cos(\phi_x) \sin(\chi) \end{array}}{\cos(\theta_z) \left(\begin{array}{c} [\hat{\mathbf{a}}]_2 \ell_x^{(L)} \csc(\theta_x) \cos(\phi_x) - [\hat{\mathbf{a}}]_1 \ell_y^{(L)} \csc(\theta_y) \sin(\phi_x) \cos(\chi) \\ -j [\hat{\mathbf{a}}]_1 \ell_y^{(L)} \csc(\theta_y) \sin(\phi_x) \sin(\chi) \end{array} \right)} \right\}$
x-z	$\angle \left\{ \frac{[\hat{\mathbf{a}}]_2 \ell_x^{(L)} \csc(\theta_x) \sin(\phi_x)}{\begin{array}{c} [\hat{\mathbf{a}}]_1 \ell_z^{(L)} \csc(\theta_z) \sin(\theta_z) \cos(\chi) + [\hat{\mathbf{a}}]_2 \ell_x^{(L)} \csc(\theta_x) \cos(\phi_x) \cos(\theta_z) \\ +j [\hat{\mathbf{a}}]_1 \ell_z^{(L)} \csc(\theta_z) \sin(\theta_z) \sin(\chi) \end{array}} \right\}$
y-z	$\angle \left\{ \frac{-[\hat{\mathbf{a}}]_2 \ell_y^{L} \csc(\theta_y) \cos(\phi_x)}{\begin{array}{c} [\hat{\mathbf{a}}]_1 \ell_z^{(L)} \csc(\theta_z) \sin(\theta_z) \cos(\chi) + [\hat{\mathbf{a}}]_2 \ell_y^{L} \csc(\theta_y) \sin(\phi_x) \cos(\theta_z) \\ +j [\hat{\mathbf{a}}]_1 \ell_z^{(L)} \csc(\theta_z) \sin(\theta_z) \sin(\chi) \end{array}} \right\}$

Here, the received signal $s(t) = \sigma_s e^{j(2\pi f_o t)}$ is a pure tone with a known amplitude of σ_s and a known frequency of f_o. At the mth time-instant of $t = mT_s$, the 2×1 collected data-vector by the dipole-pair is given by:

$$\mathbf{z}(mT_s) \quad = \quad \mathbf{a}s(mT_s) + \mathbf{n}(mT_s), \tag{5.8}$$

where T_s denotes the time-sampling period, $\mathbf{n}(t)$ symbolizes a 2×1 vector of spatio-temporally uncorrelated zero-mean Gaussian additive noise, with a deterministic covariance-matrix of $\mathbf{\Gamma}_0 = \mathrm{diag}\left(\sigma_n^2, \sigma_n^2\right)$, where σ_n^2 represents the prior known noise-variance at each dipole.

With M number of time-samples, the $2M \times 1$ collected data-set equals

$$\begin{aligned} \boldsymbol{\zeta} &= \left[(\mathbf{z}(T_s))^T, \cdots, (\mathbf{z}(MT_s))^T \right]^T \\ &= \overbrace{\mathbf{s} \otimes \mathbf{a}}^{\boldsymbol{\mu}:=} + \overbrace{\left[(\mathbf{n}(T_s))^T, \cdots, (\mathbf{n}(MT_s))^T \right]^T}^{\boldsymbol{\nu}:=}, \end{aligned} \tag{5.9}$$

where $\mathbf{s} := \sigma_s \left[e^{jT_s\omega}, e^{j2T_s\omega}, \cdots, e^{jMT_s\omega} \right]^T$, $\otimes$ symbolizes the Kronecker product, $\boldsymbol{\nu}$ represents a $2M \times 1$ noise vector with a spatio-temporal covariance matrix of $\mathbf{\Gamma} = \mathbf{I}_M \otimes \mathbf{\Gamma}_0$, and $\mathbf{I}_M$ denotes an $M \times M$ identity matrix. Therefore, $\boldsymbol{\zeta} \sim \mathcal{N}(\boldsymbol{\mu}, \mathbf{\Gamma})$, i.e. a Gaussian vector with mean $\boldsymbol{\mu}$ and covariance $\mathbf{\Gamma}$.

The to-be-estimated γ and η are modeled as deterministic. Collect them into a 2×1 vector of $\boldsymbol{\psi} = [\gamma, \eta]^T$. The resulting 2×2 Fisher information matrix (FIM),

$$\mathbf{J} = \begin{bmatrix} J_{\gamma,\gamma} & J_{\gamma,\eta} \\ J_{\eta,\gamma} & J_{\eta,\eta} \end{bmatrix}, \tag{5.10}$$

has its (p, q)th entry equal to (please see equation (8.34) in [66]):

$$\begin{aligned} [\mathbf{J}]_{p,q} &= 2\mathrm{Re}\left[\left(\frac{\partial \boldsymbol{\mu}}{\partial [\boldsymbol{\psi}]_p} \right)^H \boldsymbol{\Gamma}^{-1} \left(\frac{\partial \boldsymbol{\mu}}{\partial [\boldsymbol{\psi}]_q} \right) \right] \\ &\quad + \mathrm{Tr}\left[\boldsymbol{\Gamma}^{-1} \frac{\partial \boldsymbol{\Gamma}}{\partial [\boldsymbol{\psi}]_p} \boldsymbol{\Gamma}^{-1} \frac{\partial \boldsymbol{\Gamma}}{\partial [\boldsymbol{\psi}]_q} \right], \end{aligned} \tag{5.11}$$

where $\mathrm{Re}[.]$ denotes the real-value part of the entity inside $[.]$, $\mathrm{Tr}[.]$ represents the trace operator, and

$$\frac{\partial \boldsymbol{\mu}}{\partial \gamma} = \frac{\partial \mathbf{a}}{\partial \gamma} \otimes \mathbf{s}, \tag{5.12}$$

$$\frac{\partial \boldsymbol{\mu}}{\partial \eta} = \frac{\partial \mathbf{a}}{\partial \eta} \otimes \mathbf{s}, \tag{5.13}$$

$$\frac{\partial \mathbf{a}}{\partial \gamma} = \mathbf{DS} \left\{ \boldsymbol{\Theta} \begin{bmatrix} \cos\gamma e^{j\eta} \\ -\sin\gamma \end{bmatrix} \right\} \circ \begin{bmatrix} \ell_x^{(L)} \\ \ell_y^{(L)} \\ \ell_z^{(L)} \end{bmatrix} \circ \begin{bmatrix} \csc(\theta_x) \\ \csc(\theta_y) \\ \csc(\theta_z) \end{bmatrix}, \tag{5.14}$$

$$\frac{\partial \mathbf{a}}{\partial \eta} = \mathbf{DS} \left\{ \boldsymbol{\Theta} \begin{bmatrix} j\sin\gamma e^{j\eta} \\ 0 \end{bmatrix} \right\} \circ \begin{bmatrix} \ell_x^{(L)} \\ \ell_y^{(L)} \\ \ell_z^{(L)} \end{bmatrix} \circ \begin{bmatrix} \csc(\theta_x) \\ \csc(\theta_y) \\ \csc(\theta_z) \end{bmatrix}. \tag{5.15}$$

The elements of the Fisher information matrix equal

$$\begin{aligned} J_{\gamma,\gamma} &= 2M\frac{\sigma_s^2}{\sigma_n^2} \Bigg\{ \left[\left([\mathbf{S\Theta}]_{1,1} \ell_i^{(L)} \csc(\theta_i) \right)^2 + \left([\mathbf{S\Theta}]_{2,1} \ell_j^{(L)} \csc(\theta_j) \right)^2 \right] \cos^2(\gamma) \\ &\quad + \left[\left([\mathbf{S\Theta}]_{1,2} \ell_i^{(L)} \csc(\theta_i) \right)^2 + \left([\mathbf{S\Theta}]_{2,2} \ell_j^{(L)} \csc(\theta_j) \right)^2 \right] \sin^2(\gamma) \\ &\quad - \left[[\mathbf{S\Theta}]_{1,1} [\mathbf{S\Theta}]_{1,2} \left(\ell_i^{(L)} \csc(\theta_i) \right)^2 + [\mathbf{S\Theta}]_{2,1} [\mathbf{S\Theta}]_{2,2} \left(\ell_j^{(L)} \csc(\theta_j) \right)^2 \right] \\ &\quad \sin(2\gamma)\cos(\eta) \Bigg\} \\ &= 2M\frac{\sigma_s^2}{\sigma_n^2} \Big[c_1 \cos^2(\gamma) + c_2 \sin^2(\gamma) - c_3 \sin(2\gamma)\cos(\eta) \Big], \end{aligned} \tag{5.16}$$

$$
\begin{aligned}
J_{\eta,\eta} &= 2M\frac{\sigma_s^2}{\sigma_n^2}\left[\left([\mathbf{S\Theta}]_{1,1}\ell_i^{(L)}\csc(\theta_i)\right)^2+\left([\mathbf{S\Theta}]_{2,1}\ell_j^{(L)}\csc(\theta_j)\right)^2\right]\sin^2(\gamma) \\
&= 2M\frac{\sigma_s^2}{\sigma_n^2}c_1\sin^2(\gamma), \qquad (5.17)
\end{aligned}
$$

$$
\begin{aligned}
J_{\gamma,\eta} &= J_{\eta,\gamma} \\
&= 2M\frac{\sigma_s^2}{\sigma_n^2}\Bigg[[\mathbf{S\Theta}]_{1,1}[\mathbf{S\Theta}]_{1,2}\left(\ell_i^{(L)}\csc(\theta_i)\right)^2 \\
&\qquad +[\mathbf{S\Theta}]_{2,1}[\mathbf{S\Theta}]_{2,2}\left(\ell_j^{(L)}\csc(\theta_j)\right)^2\Bigg]\sin^2(\gamma)\sin(\eta) \\
&= 2M\frac{\sigma_s^2}{\sigma_n^2}c_3\sin^2(\gamma)\sin(\eta), \qquad (5.18)
\end{aligned}
$$

where

$$
\begin{aligned}
c_1 &= \left([\mathbf{S\Theta}]_{1,1}\ell_i^{(L)}\csc(\theta_i)\right)^2+\left([\mathbf{S\Theta}]_{2,1}\ell_j^{(L)}\csc(\theta_j)\right)^2, \\
c_2 &= \left([\mathbf{S\Theta}]_{1,2}\ell_i^{(L)}\csc(\theta_i)\right)^2+\left([\mathbf{S\Theta}]_{2,2}\ell_j^{(L)}\csc(\theta_j)\right)^2, \\
c_3 &= [\mathbf{S\Theta}]_{1,1}[\mathbf{S\Theta}]_{1,2}\left(\ell_i^{(L)}\csc(\theta_i)\right)^2+[\mathbf{S\Theta}]_{2,1}[\mathbf{S\Theta}]_{2,2}\left(\ell_j^{(L)}\csc(\theta_j)\right)^2
\end{aligned}
$$

with $[\cdot]_{p,q}$ symbolizing the (p,q)th entry of the matrix in $[\cdot]$ and $_i$ and $_j$ denote subscripts of the electric-field components in (6.16) captured by the dipole pair. For example, the x-y configuration has $i=x$ and $j=y$, and likewise for the other two configurations.

The polarization-estimation Cramér-Rao bounds equal

$$
\begin{aligned}
\text{CRB}(\gamma) &= \left[\mathbf{J}^{-1}\right]_{1,1} = \frac{J_{\eta,\eta}}{J_{\gamma,\gamma}J_{\eta,\eta}-(J_{\gamma,\eta})^2} \\
&= \frac{\sigma_n^2}{\sigma_s^2}\frac{1}{2M}\frac{c_1}{\left\{\begin{array}{c} c_1^2\cos^2(\gamma)+c_1c_2\sin^2(\gamma) \\ -c_1c_3\sin(2\gamma)\cos(\eta) \\ -c_3^2\sin^2(\gamma)\sin^2(\eta)\end{array}\right\}}, \qquad (5.19)
\end{aligned}
$$

$$
\begin{aligned}
\mathrm{CRB}(\eta) &= \left[\mathbf{J}^{-1}\right]_{2,2} = \frac{J_{\gamma,\gamma}}{J_{\gamma,\gamma}J_{\eta,\eta} - (J_{\gamma,\eta})^2} \\
&= \frac{\sigma_n^2}{\sigma_s^2}\frac{1}{2M}\frac{\csc^2(\gamma)\left\{\begin{array}{c} c_1\cos^2(\gamma) + c_2\sin^2(\gamma) \\ -c_3\sin(2\gamma)\cos(\eta) \end{array}\right\}}{\left\{\begin{array}{c} c_1^2\cos^2(\gamma) + c_1c_2\sin^2(\gamma) \\ -c_3c_1\sin(2\gamma)\cos(\eta) \\ -c_3^2\sin^2(\gamma)\sin^2(\eta) \end{array}\right\}}. \qquad (5.20)
\end{aligned}
$$

Tables 5.3 lists the new closed-form CRB(γ) and CRB(η), expressed explicitly in terms of the data-model parameters.

Some qualitative observations on the Cramér-Rao bounds derived above:

(A) These Cramér-Rao bounds would have the same numerical value regardless of the (prior known) spatial separation between the two dipoles. This spatial separation would affect χ, which is nonetheless canceled out in the derivation of the Fisher information matrix. However, the incident source's frequency does effect the effective lengths of the antennas; hence, the Cramér-Rao bounds would be changed by changing the frequency.

(B) Recall that any fully polarized signal may be decomposed as a sum of a *vertically* polarized component and an *horizontally* polarized component. Hence, only these two linear polarizations are shown in these figures.

(C) At $\gamma \to 0$, CRB(η) $\to \infty$, for all three configurations. The reason is as following: At $\gamma = 0$, the electric-field vector in (6.16) becomes functionally independent of η. Regardless of the value of η, $(\gamma = 0, \eta)$ would refer to one same point on the Poincare sphere (i.e. one same polarization). The circularly polarized cases' CRB(η) graphs would then look similar to that of the vertically polarized case.

For the x-y dipole-pair (i.e. configuration 1 in Table 5.1), Figure 5.2 plots $2M\left(\frac{\sigma_s}{\sigma_n}\right)^2$ CRB(γ) and $2M\left(\frac{\sigma_s}{\sigma_n}\right)^2$ CRB(η) versus the direction-of-arrival (θ_z, ϕ_x). Figure 5.3 plots these same Cramér-Rao bounds versus the bivariate polarization (γ, η). Below are qualitative observations specifically on the x-y dipole-pair's Cramér-Rao bounds:

(D) A four-fold symmetry exists along the ϕ_x-coordinates, in all x-y dipole-pair Cramér-Rao bounds. This is due to this dipole-pair's $90°$ rotational symmetry in ϕ_x on the x-y plane.

(E) A symmetry exists along the θ_z-coordinates, with respect to $\theta = 90°$ (i.e. at horizontal incidence) in all x-y dipole-pair Cramér-Rao bounds. This is due to this dipole-pairs symmetry between the upper versus the lower hemispheres.

(F) At vertical polarization (i.e. $\gamma = 90°$ and $\eta = 0°$), that part of the incident source's energy in e_z cannot be measured by either the x-dipole nor the y-dipole. This polarization mismatch explains why the graphs peak at $\theta_z = 90°$.

(G) At horizontal polarization (i.e. $\gamma = 0°$ and $\eta = 0°$), all incident energy is embedded in e_x and e_y, which are fully measured by the x-dipole and/or the y-dipole. Hence, the Cramér-Rao bounds vary with the two dipoles' radiation pattern over (θ_z, ϕ_x).

(H) At vertical incidence (i.e. $\theta_z = 0°, 180°$), the source always lie simultaneously in both main lobes of the x-dipole nor the y-oriented dipole; hence, CRB(γ) is small. At horizontal incidence (i.e. $\theta_z = 90°$), the source cannot lie simultaneously in both main lobes of the x-dipole nor the y-oriented dipole; hence, CRB(γ) is large.

For the x-z dipole-pair (i.e. configuration 2 in Table 5.1), Figure 5.4 plots $2M\left(\frac{\sigma_s}{\sigma_n}\right)^2$ CRB(γ) and $2M\left(\frac{\sigma_s}{\sigma_n}\right)^2$ CRB(η) versus the direction-of-arrival (θ_z, ϕ_x). Figure 5.5 plots these same Cramér-Rao bounds versus the bivariate polarization (γ, η). Below are the qualitative observations specifically on the x-z dipole-pair's Cramér-Rao bounds:

(I) A two-fold symmetry exists along the ϕ_x-coordinates, in all x-z dipole-pair Cramér-Rao bounds. This is due to this dipole-pair's $180°$ rotational symmetry in ϕ_x on the x-y plane.

(J) A symmetry exists along the θ_z-coordinates, with respect to $\theta_z = 90°$ (i.e. at horizontal incidence) in all x-z dipole-pair Cramér-Rao bounds. This is due to this dipole pair's symmetry between the left versus the right hemispheres.

(K) At vertical polarization (i.e. $\gamma = 90°$ and $\eta = 0°$) and $\phi_x = 0°, 180°$: e_{θ_z} lies perpendicular to the x-axis; the x-dipole consequentially cannot capture any incident energy; hence, the ridges appear.

(L) At vertical polarization (i.e. $\gamma = 90°$ and $\eta = 0°$) and at near-vertical incidence (i.e. $\theta_z \approx 0°, 180°$): the source lies in the z-dipole's null [4]regardless of the source's ϕ_x, but in the x-dipole's null [5]only for $\phi_x \approx 90°, 270°$; hence, CRB(γ) is large. This explains the spikes in Figure 5.4(a).

(M) Only z-dipole responds to e_{θ_z} if $\theta_z = 90°$. e_{θ_z} can only be detected by the x-dipole if $\theta_z = 0°, 180°$.

A relationship exists between the x-z dipole-pair (i.e. configuration 2 in Table 5.1), the y-z dipole-pair (i.e. configuration 3 in Table 5.1). The latter's Cramér-Rao bounds are obtainable by substituting $\phi_x - \frac{\pi}{2}$ for ϕ_x in the former's. Hence, the former's plots will not shown/discussed separately.

5.5 Monte Carlo Simulations

To verify the efficacy of the eigen-based estimators newly proposed in Section 5.3, Monte Carlo simulations are conducted in this section. The simulation results are presented in Figures 5.6-5.7, along with the corresponding deterministic Cramér-Rao bounds for comparison. Because the estimators in Table 5.1 need no prior information about σ_s and σ_n; the Cramér-Rao bounds plotted here will correspondingly allow σ_s and σ_n as nuisance parameters.

---

[4] Here, the electric field lies entirely on the x-y plane. Hence, the z-dipole receives no incident energy.

[5] Here, e_{ϕ_x} lies perpendicularly to the x-axis. Therefore, the x-dipole receives no incident energy.

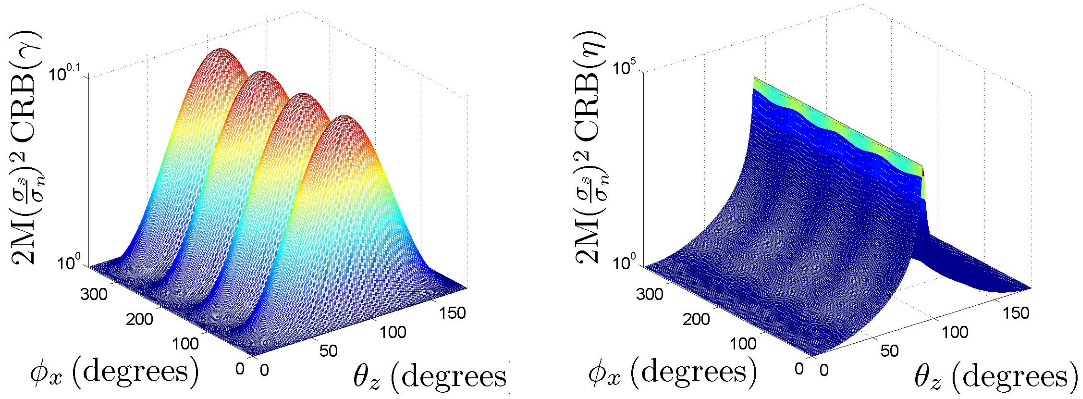

(a) The source impinges with a vertical polarization. i.e. $\gamma = 90°, \eta = 0°$.

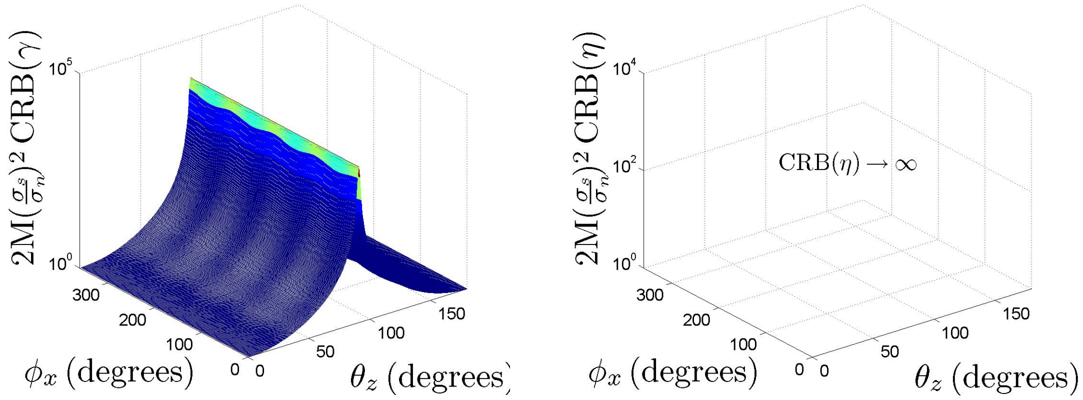

(b) The source impinges with a horizontal polarization. i.e. $\gamma = 0°, \eta = 0°$.

Fig. 5.2.: The x-y pair of $\frac{\lambda}{2}$ electrically long dipoles.

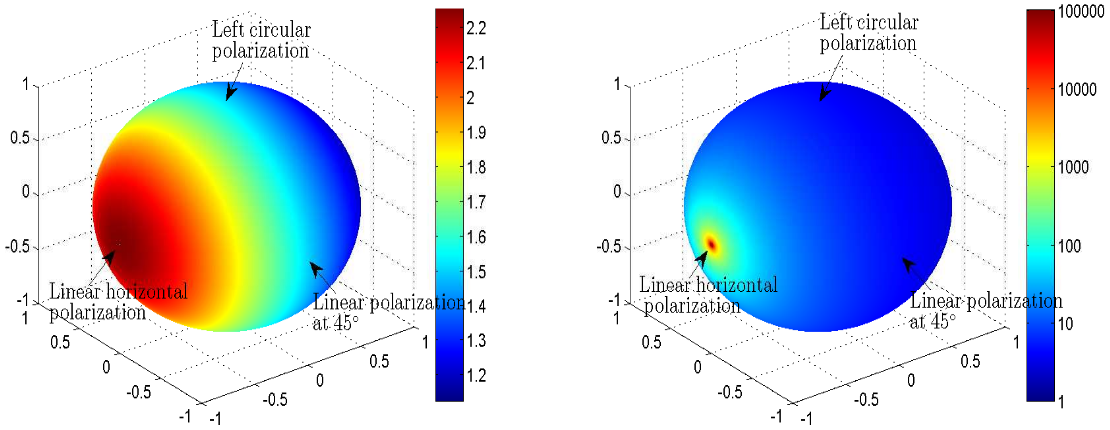

(a) $2M\left(\frac{\sigma_s}{\sigma_n}\right)^2$ CRB(γ) on Poincare sphere.

(b) $2M\left(\frac{\sigma_s}{\sigma_n}\right)^2$ CRB(η) on Poincare sphere.

Fig. 5.3.: The x-y pair of $\frac{\lambda}{2}$ electrically long dipoles, with a source impinging from a DOA of $\theta_z = 45°,\ \phi_x = 45°$.

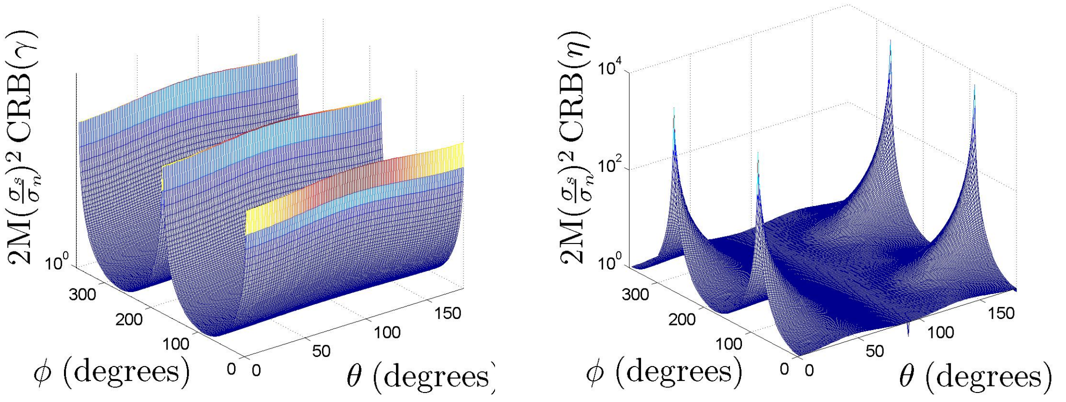

(a) The source impinges with a vertical polarization. i.e. $\gamma = 90°, \eta = 0°$.

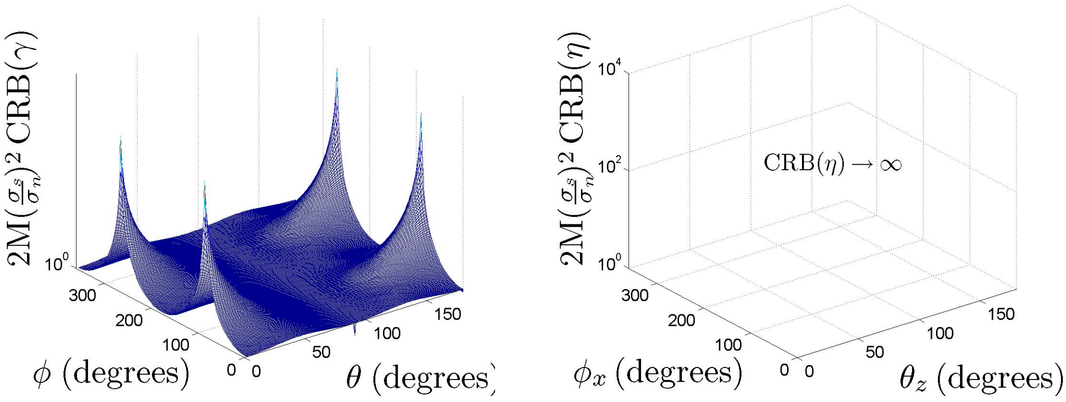

(b) The source impinges with a horizontal polarization. i.e. $\gamma = 0°, \eta = 0°$.

Fig. 5.4.: The x-z pair of $\frac{\lambda}{2}$ electrically long dipoles.

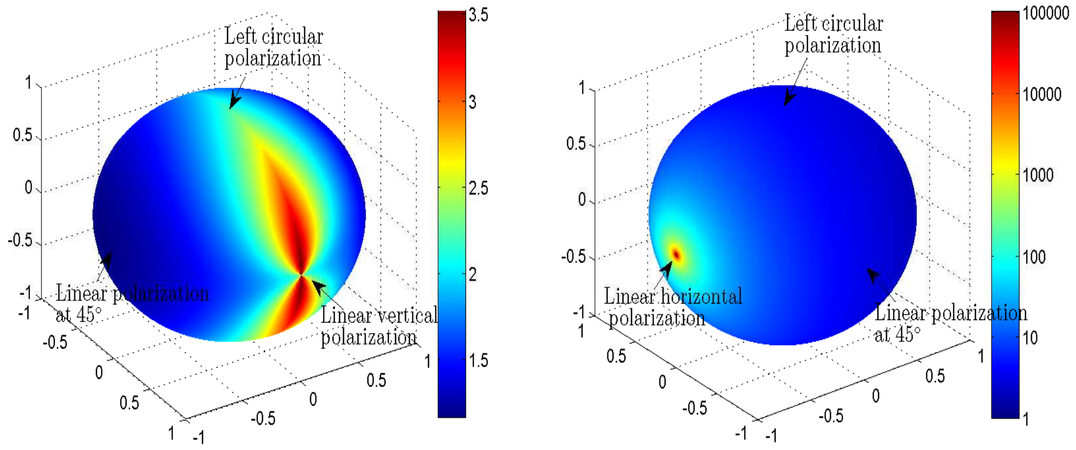

(a) $2M\left(\frac{\sigma_s}{\sigma_n}\right)^2 \mathrm{CRB}(\gamma)$ on Poincare sphere.

(b) $2M\left(\frac{\sigma_s}{\sigma_n}\right)^2 \mathrm{CRB}(\eta)$ on Poincare sphere.

Fig. 5.5.: The x-z pair of $\frac{\lambda}{2}$ electrically long dipoles, with a source impinging from a DOA of $\theta_z = 45°,\ \phi_x = 45°$.

Table 5.3.: Cramér-Rao Bounds of the Polarization Estimates for the 3 Dipole-Pair Configurations

Dipole Pair	CRB
x-y	$\mathrm{CRB}(\gamma)=\frac{\sigma_n^2}{\sigma_s^2}\frac{1}{2M}\frac{\left[\left(\ell_x\cos(\phi_x)\right)^2+\left(\ell_y\sin(\phi_x)\right)^2\right]}{\left\{\left[\left(\ell_x\cos(\phi_x)\right)^2+\left(\ell_y\sin(\phi_x)\right)^2\right]\left\{\left[\left(\ell_x\cos(\phi_x)\right)^2+\left(\ell_y\sin(\phi_x)\right)^2\right]\left(\cos(\theta_z)\cos(\gamma)\right)^2+\left[\left(\ell_x\sin(\phi_x)\right)^2+\left(\ell_y\cos(\phi_x)\right)^2\right]\sin^2(\gamma)+\left[\left(\ell_x^2-\ell_y^2\right)\cos(\eta)\sin(2\gamma)\sin(\phi_x)\cos(\theta_z)\cos(\phi_x)\right]\right\}-\left[\left(\ell_x^2-\ell_y^2\right)\cos(\phi_x)\cos(\theta_z)\sin(\phi_x)\sin(\gamma)\sin(\eta)\right]^2\right\}}$ $\mathrm{CRB}(\eta)=\frac{\sigma_n^2}{\sigma_s^2}\frac{1}{2M}\frac{\left\{\left[\left(\ell_x\cos(\phi_x)\right)^2+\left(\ell_y\sin(\phi_x)\right)^2\right]\left(\cos(\theta_z)\cos(\gamma)\right)^2+\left[\left(\ell_x\sin(\phi_x)\right)^2+\left(\ell_y\cos(\phi_x)\right)^2\right]\sin^2(\gamma)+\left(\ell_x^2-\ell_y^2\right)\sin(\phi_x)\cos(\theta_z)\cos(\phi_x)\cos(\eta)\sin(2\gamma)\right\}}{\left\{\left[\left(\ell_x\cos(\phi_x)\right)^2+\left(\ell_y\sin(\phi_x)\right)^2\right]\left\{\left[\left(\ell_x\cos(\phi_x)\right)^2+\left(\ell_y\sin(\phi_x)\right)^2\right]\left(\cos(\theta_z)\cos(\gamma)\right)^2+\left[\left(\ell_x\sin(\phi_x)\right)^2+\left(\ell_y\cos(\phi_x)\right)^2\right]\sin^2(\gamma)+\left[\left(\ell_x^2-\ell_y^2\right)\sin(\phi_x)\cos(\theta_z)\cos(\phi_x)\cos(\eta)\sin(2\gamma)\right]\right\}\left(\cos(\theta_z)\sin(\gamma)\right)^2-\left[\left(\ell_x^2-\ell_y^2\right)\cos(\phi_x)\cos(\theta_z)\sin(\phi_x)\sin^2(\gamma)\sin(\eta)\right]^2\right\}}$
x-z	$\mathrm{CRB}(\gamma)=\frac{\sigma_n^2}{\sigma_s^2}\frac{1}{2M}\frac{\left[\left(\ell_x\cos(\phi_x)\cos(\theta_z)\right)^2+\left(\ell_z\sin(\theta_z)\right)^2\right]}{\left\{\left[\left(\ell_x\cos(\phi_x)\cos(\theta_z)\right)^2+\left(\ell_z\sin(\theta_z)\right)^2\right]\left\{\left[\left(\ell_x\cos(\phi_x)\cos(\theta_z)\right)^2+\left(\ell_z\sin(\theta_z)\right)^2\right]\cos^2(\gamma)+\left(\ell_x\sin(\phi_x)\sin(\gamma)\right)^2+\ell_x^2\sin(\phi_x)\cos(\theta_z)\cos(\phi_x)\cos(\eta)\sin(2\gamma)\right\}-\left[\ell_x^2\sin(\phi_x)\cos(\theta_z)\cos(\phi_x)\sin(\gamma)\sin(\eta)\right]^2\right\}}$ $\mathrm{CRB}(\eta)=\frac{\sigma_n^2}{\sigma_s^2}\frac{1}{2M}\frac{\left[\left(\ell_x\cos(\phi_x)\cos(\theta_z)\right)^2+\left(\ell_z\sin(\theta_z)\right)^2\right]\cos^2(\gamma)+\left(\ell_x\sin(\phi_x)\sin(\gamma)\right)^2+\ell_x^2\sin(\phi_x)\cos(\theta_z)\cos(\phi_x)\cos(\eta)\sin(2\gamma)}{\left\{\left[\left(\ell_x\cos(\phi_x)\cos(\theta_z)\right)^2+\left(\ell_z\sin(\theta_z)\right)^2\right]\left\{\left[\left(\ell_x\cos(\phi_x)\cos(\theta_z)\right)^2+\left(\ell_z\sin(\theta_z)\right)^2\right]\cos^2(\gamma)+\left(\ell_x\sin(\phi_x)\sin(\gamma)\right)^2+\ell_x^2\sin(\phi_x)\cos(\theta_z)\cos(\phi_x)\cos(\eta)\sin(2\gamma)\right\}\sin^2(\gamma)-\left[\ell_x^2\sin(\phi_x)\cos(\theta_z)\cos(\phi_x)\sin^2(\gamma)\sin(\eta)\right]^2\right\}}$
y-z	$\mathrm{CRB}(\gamma)=\frac{\sigma_n^2}{\sigma_s^2}\frac{1}{2M}\frac{\left[\left(\ell_y\sin(\phi_x)\cos(\theta_z)\right)^2+\left(\ell_z\sin(\theta_z)\right)^2\right]}{\left\{\left[\left(\ell_y\sin(\phi_x)\cos(\theta_z)\right)^2+\left(\ell_z\sin(\theta_z)\right)^2\right]\left\{\left[\left(\ell_y\sin(\phi_x)\cos(\theta_z)\right)^2+\left(\ell_z\sin(\theta_z)\right)^2\right]\cos^2(\gamma)+\left[\left(\ell_y\cos(\phi_x)\sin(\gamma)\right)^2\right]-\left[\ell_y^2\cos(\phi_x)\cos(\theta_z)\sin(\phi_x)\cos(\eta)\sin(2\gamma)\right]\right\}-\left[\ell_y^2\sin(\phi_x)\cos(\theta_z)\cos(\phi_x)\sin(\gamma)\sin(\eta)\right]^2\right\}}$ $\mathrm{CRB}(\eta)=\frac{\sigma_n^2}{\sigma_s^2}\frac{1}{2M}\frac{\left[\left(\ell_y\sin(\phi_x)\cos(\theta_z)\right)^2+\left(\ell_z\sin(\theta_z)\right)^2\right]\cos^2(\gamma)+\left(\ell_y\cos(\phi_x)\sin(\gamma)\right)^2-\ell_y^2\sin(\phi_x)\cos(\theta_z)\cos(\phi_x)\cos(\eta)\sin(2\gamma)}{\left\{\left[\left(\ell_y\sin(\phi_x)\cos(\theta_z)\right)^2+\left(\ell_z\sin(\theta_z)\right)^2\right]\left\{\left[\left(\ell_y\sin(\phi_x)\cos(\theta_z)\right)^2+\left(\ell_z\sin(\theta_z)\right)^2\right]\cos^2(\gamma)+\left[\left(\ell_y\cos(\phi_x)\sin(\gamma)\right)^2\right]-\left[\ell_y^2\cos(\phi_x)\cos(\theta_z)\sin(\phi_x)\cos(\eta)\sin(2\gamma)\right]\right\}\sin^2(\gamma)-\left[\ell_y^2\sin(\phi_x)\cos(\theta_z)\cos(\phi_x)\sin^2(\gamma)\sin(\eta)\right]^2\right\}}$

In this table, $\ell_x=\ell_x^{(L)}\csc(\theta_x)$, $\ell_y=\ell_y^{(L)}\csc(\theta_y)$, $\ell_z=\ell_z^{(L)}\csc(\theta_z)$.

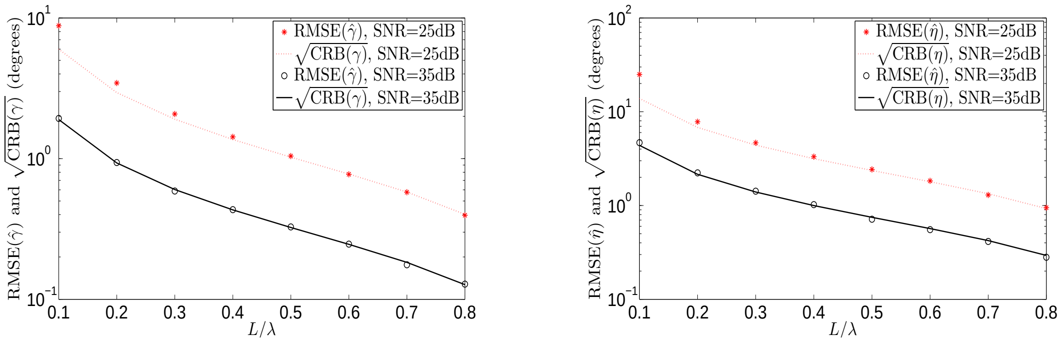

(a) for $\hat{\gamma}$

(b) for $\hat{\eta}$

Fig. 5.6.: An x-y pair of electrically long dipoles – their $\sqrt{\text{CRB}}$ and the RMSE for $\hat{\gamma}$ and $\hat{\eta}$.

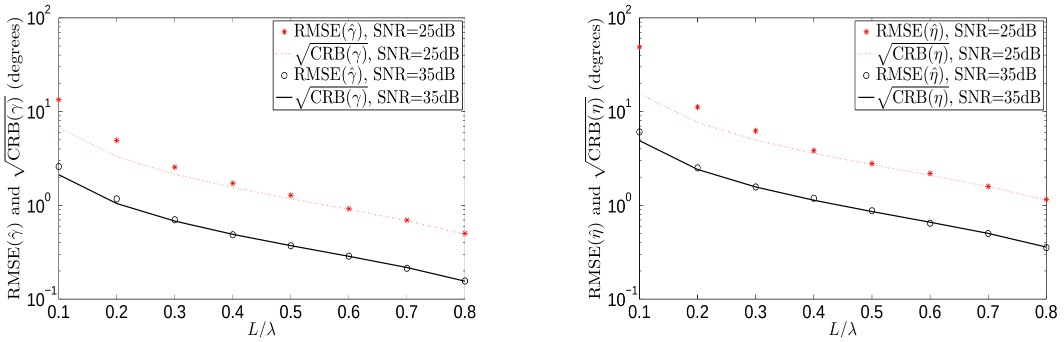

(a) for $\hat{\gamma}$

(b) for $\hat{\eta}$

Fig. 5.7.: An x-z pair of electrically long dipoles – their $\sqrt{\text{CRB}}$ and the RMSE for $\hat{\gamma}$ and $\hat{\eta}$.

All graphs here use these numerical settings: $M = 100$, $\phi_x = 30^o$, $\theta_z = 45^o$, $\gamma = 30^o$, $\eta = 60^o$, and a digital frequency $f_o = 0.3$. Each icon on every graph represents 1000 independent Monte Carlo experiments. These figures show $\frac{L}{\lambda}$ only up to 0.8, because the "effective length" expressions of (5.2)-(5.4) are invalid when the physical length is near integer-multiples of the wavelength.

Figures 5.6-5.7 indicate that the proposed estimators perform close to the Cramér-Rao bounds. Recall that the "effective length" affects the dipole's gain, nonlinearly and non-monotonically in (5.2)-(5.4), through sinusoidal functions. Figures 5.6-5.7 verify that the shorter the dipole, the less accurate the estimates would be.

5.6 Conclusion

For the first time in the open literature, electrically long dipole pair are investigated for polarization estimation. Newly proposed here are closed-form polarization-estimation formulas and the corresponding deterministic Cramér-Rao bounds. These new estimators offer error variances close to the Cramér-Rao lower bounds, according to Monte Carlo simulations.

6

Large Circular Loops in the Estimation of an Incident Emitter's Direction-of-Arrival or Polarization

6.1 Introduction

Please consider three magnetic loops: Spatially collocate them; and orient them perpendicularly among themselves as shown in Figure 6.1.

These loops' spatial collocation results in a physically compact array easy for transportation and deployment, whereas the three loops' orthogonal orientation facilitates the measurement of the incident magnetic-field vector by its three distinct Cartesian components.

For *small* loops, such a triad has already been considered in the open literature for estimating incident sources' azimuth-elevation directions-of-estimation and polarizations, for example in [28, 37, 62, 141]. Among these references, [28, 37, 62] offer closed-form algorithms. For such estimates' error variance, Cramér-Rao bounds and other lower bounds have been derived in closed forms in [72, 73]. Nonetheless, *all* aforementioned references implicitly presume the loops to be magnetically *small*, such that the loop-triad's 3×1 array manifold would simply equal the magnetic-field vector expressed in Cartesian coordinates. This simplifying assumption would indeed be approximately valid for circular loops with a radius of $R < \frac{\lambda}{20\pi}$.

Such a small loop is *in*effective as a radiator and is barely effective as a receiver, due to the small ratio of radiation-to-loss resistance [68, p. 231][1]. To be a practical antenna, the loop radius R should substantially exceeds $\frac{\lambda}{20\pi}$.

---

[1] Based on equations (2-90b), (5-24), and (5-64a) in [68], the radiation efficiency is only 4.5% for a loop with a circumference of $2\pi R = \frac{\lambda}{10}$, 42% if $2\pi R = \frac{\lambda}{4}$, 63% if $2\pi R = \frac{\lambda}{3}$, but 97% if $2\pi R = \lambda$.

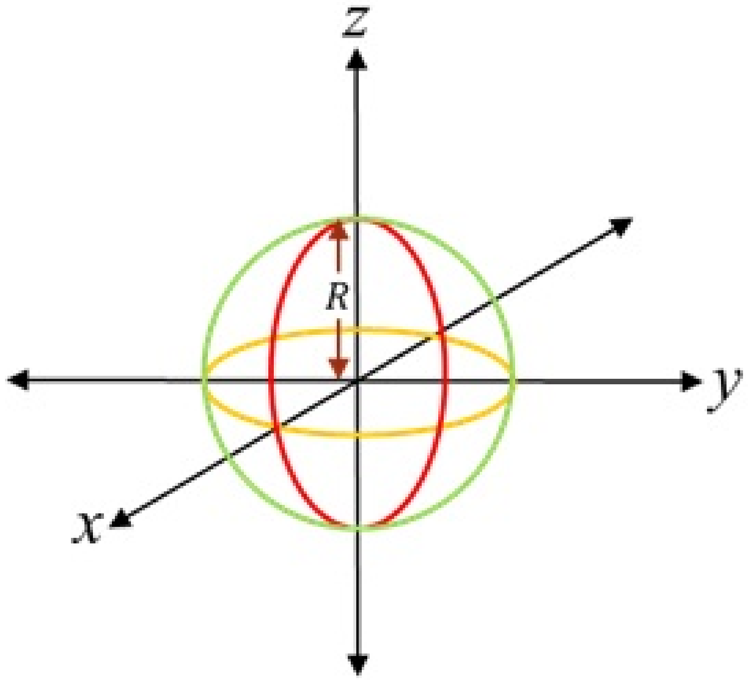

Fig. 6.1.: Collocated and orthogonally oriented loop triad.

Such magnetically *large* loops have been entirely overlooked by the signal-processing literature on direction finding or polarization estimation.

On the other hand, for any circular loop-antenna with a circumference of $2\pi R \geq 3.8317\lambda$ (3.8317 equals the smallest positive zero of the Bessel function of the first kind and order 1), the loop-antenna's beam-pattern would suffer from sidelobes [68, p. 249]. Indeed, for $2\pi\frac{R}{\lambda}$ near any zero of the Bessel function (like $2\pi\frac{R}{\lambda} \sim 3.8317$), a loop antenna would give a very small voltage, (i.e., would become electromagnetically inefficient), hence should be avoided.

Given the two preceding paragraphs' considerations on $\frac{R}{\lambda}$, real-world loop-antennas often have a wavelength-normalized circumference of $2\pi\frac{R}{\lambda}$ within the range of $(0.1, 3.8317)$.[2] For such magnetically “large" circular-loop antennas, this Chapter (i) will formulate a new array manifold for three

---

[2] A circular loop with circumference equal to one wavelength is commonly known as a resonant loop and is considered as fundamental as the half-wavelength dipole (pp. 249-250, Section 5.3.2 of [68]). Such a loop is classified as end-fire antenna, as the maximum radiation occur along the axis of loop, therefore making it useful in the design of directional antenna arrays, for example in Yagi-Uda arrays. The resonant loop is significant also because it's radiation resistance approximately equals 100Ω, which can be matched easily to a 50Ω or a 75Ω transmission line.

magnetically large circular loops that are arranged in collocation and orthogonal orientation, (ii) will pioneer closed-form signal-processing algorithms for the abovementioned triad to estimate the incident signal's azimuth-elevation direction-of-arrival and polarization, and (iii) will show that these newly proposed estimators can offer an error variance approaching the corresponding Cramér-Rao lower bounds.

The rest of this chapter is organized as follows: Section 6.2 will derive a magnetically large circular-loop antenna's “effective length", and will then formulate the loop-triad's array manifold. Section 6.3 will propose new eigen-based estimates of an incident source's arrival direction or polarization without any prior knowledge of the loops' radius or of the incident signal's wavelength. Section 6.4 will present Monte Carlo simulations to verify these new estimators' efficacy and statistical closeness to the Cramér-Rao lower bounds. Section 6.5 will conclude the entire Chapter.

6.2 The Newly Formulated Array Manifold of a Triad of Magnetically Large Loops

Consider a fully polarized plane-wave of unit power per unit area , with an auxiliary polarization angle of $\gamma \in \left[0, \frac{\pi}{2}\right]$ and a polarization phase difference of $\eta \in [-\pi, \pi)$. Suppose this electromagnetic wave impinges upon collocated and orthogonally oriented loop triad located at the Cartesian origin from a polar angle of $\theta_z \in [0, \pi]$ and an azimuth angle of $\phi_x \in [-\pi, \pi)$ as shown in Figure 6.2. The electric field for such a wave is given by equation (1.8) and the corresponding magnetic field is given by equation (1.9). The definition of spatial angles in Figure 6.2 and their trigonometric relationship are given in Section 1.2.

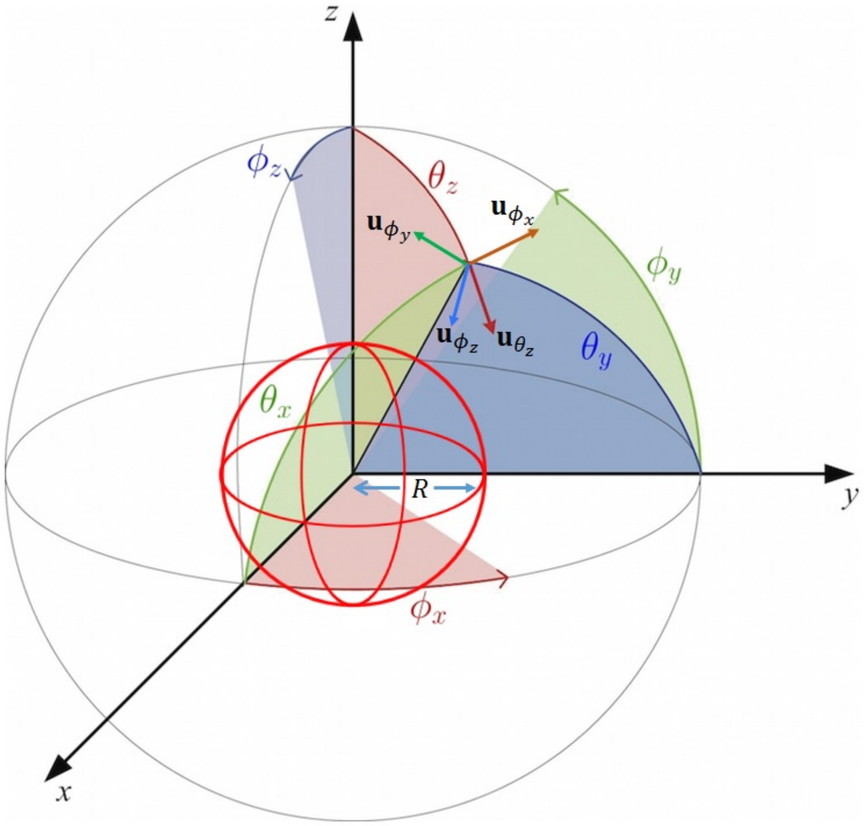

Fig. 6.2.: Different spatial angles inter-relationship.

6.2.1 The z-oriented loop-antenna's voltage

Consider a circular loop-antenna of radius R, lying on the x-y Cartesian plane, symmetrically about the Cartesian origin. This loop's normal vector points along the z-axis, thus labeled as the z-oriented loop. Onto this loop, suppose an electromagnetic wave impinges from the far field at a polar angle of θ_z and an azimuth angle of ϕ_x.

This loop-antenna's open-circuit voltage equals (see equation (4-20) of [64], or equation (2-93) of [68])

$$v_z \quad = \quad \mathbf{e} \cdot \boldsymbol{\ell}_z^{\left(\frac{R}{\lambda}\right)}(\theta_z, \phi_x), \tag{6.1}$$

where the *vector* $\boldsymbol{\ell}_z^{\left(\frac{R}{\lambda}\right)}(\theta_z, \phi_x)$ denotes the loop-antenna's “effective length" (a.k.a. the “effective height").

This “effective length", despite its name, is a 3×1 vector that varies non-monotonically with the loop’s physical size (R). This “effective length", also despite its name, varies with the incident signal’s direction-of-arrival (θ_z, ϕ_x); hence, the “effective length" is a property *not only* of the loop-antenna itself, but also depends on the incident source. Therefore, though the “effective length" has a unit in length, it is not a “length" per se and not a constant scalar, but a “pattern" to be multiplied in to the incident electric-field vector (as in (6.1)) to give the antenna’s voltage. The “effective length" for the loop could indeed be negative, which can be considered as a change of voltage polarity at the terminals.

If a uniform current[3] is achieved along a z-oriented circular loop, the “effective length" of (6.1) may be found by comparing (2-92) [68, p. 88] and (5-54b) in [68, p. 248], to give the vector,

$$\boldsymbol{\ell}_z^{\left(\frac{R}{\lambda}\right)}(\theta_z, \phi_x) \quad = \quad j2\pi R J_1\left(2\pi\frac{R}{\lambda}\sin(\theta_z)\right)\, \mathbf{u}_{\phi_x}, \tag{6.2}$$

where $J_1(.)$ represents the Bessel function of the first kind and order 1.

The “effective length" vector in (6.2) has these properties:

- The “effective length" is proportional to $J_1\left(2\pi\frac{R}{\lambda}\sin(\theta_z)\right)$, whereas $J_1(\kappa_\circ) = 0$ at $\kappa_\circ \in \{3.8317, 7.0156, 10.1735, 13.3237, 16.4706, ...\}$ [81, Section 2.7.2, p. 71]. Each $\kappa_\circ$ has its corresponding values of $\left(\frac{R}{\lambda}, \theta_z\right)$.

- The “effective length" becomes zero along the loop axis (i.e., the axis perpendicular to the plane on which the loop lies), irrespective of the loop radius R. This is because $\theta_z = 0$ implies that (6.2) degenerates to $j2\pi R J_1(0) = j2\pi R \times 0 = 0$.

---

[3] “Uniform" here means that the current’s magnitude and phase are constant along the length of the loop at any time instant. However, that magnitude and that phase may vary over time. Please refer to [74], [75], [76], [77], [78], [79], [80]. A uniform current can be achieved over the loop’s entire circumference, by subdividing the loop into sections/arcs and using different feed lines (fed from common feed source) to feed each section separately [68, p. 249].

Returning to the voltage v_z: (1.8), (6.1), and (6.2) together give

$$\begin{aligned} v_z &= j2\pi R\, J_1\left(2\pi\frac{R}{\lambda}\sin(\theta_z)\right)\,\cos(\gamma) \\ &= \ell_z^{\left(\frac{R}{\lambda}\right)}(\theta_z,\phi_x)\; h_z, \end{aligned} \tag{6.3}$$

with the scalar,

$$\ell_z^{\left(\frac{R}{\lambda}\right)}(\theta_z,\phi_x) \;:=\; j2\pi R\frac{J_1\left(2\pi\frac{R}{\lambda}\sin(\theta_z)\right)}{\sin(\theta_z)}. \tag{6.4}$$

6.2.2 The x-oriented loop-antenna's voltage

Consider a circular loop lying on the y-z plane, i.e. with a normal vector pointing along the x-axis. This loop's effective length vector equals

$$\boldsymbol{\ell}_x^{\left(\frac{R}{\lambda}\right)}(\theta_z,\phi_x) \;=\; j2\pi R J_1\left(2\pi\frac{R}{\lambda}\sin(\theta_x)\right)\mathbf{u}_{\phi_y}, \tag{6.5}$$

where

$$\mathbf{u}_{\phi_y} := [0, -\sin(\phi_y), \cos(\phi_y)]^T. \tag{6.6}$$

This loop's corresponding voltage is

$$v_x \;=\; \mathbf{e}\cdot\boldsymbol{\ell}_x^{\left(\frac{R}{\lambda}\right)}(\theta_z,\phi_x) \;=\; \ell_x^{\left(\frac{R}{\lambda}\right)}(\theta_z,\phi_x)\; h_x, \tag{6.7}$$

with the scalar,

$$\ell_x^{\left(\frac{R}{\lambda}\right)}(\theta_z,\phi_x) \;:=\; j2\pi R\frac{J_1\left(2\pi\frac{R}{\lambda}\sqrt{\sin^2(\theta_z)\sin^2(\phi_x)+\cos^2(\theta_z)}\right)}{\sqrt{\sin^2(\theta_z)\sin^2(\phi_x)+\cos^2(\theta_z)}}. \tag{6.8}$$

6.2.3 The y-oriented loop-antenna's voltage

Consider a circular loop lying on the x-z plane, i.e. with a normal vector pointing along the y-axis. This loop's effective length vector is

$$\boldsymbol{\ell}_y^{\left(\frac{R}{\lambda}\right)}(\theta_z, \phi_x) \quad = \quad j2\pi R J_1\left(2\pi \frac{R}{\lambda} \sin(\theta_y)\right) \mathbf{u}_{\phi_z}, \tag{6.9}$$

where

$$\mathbf{u}_{\phi_z} := [\cos(\phi_z), 0, -\sin(\phi_z)]^T. \tag{6.10}$$

This loop's corresponding voltage is

$$v_y \quad = \quad \mathbf{e} \cdot \boldsymbol{\ell}_y^{\left(\frac{R}{\lambda}\right)}(\theta_z, \phi_x) \quad = \quad \ell_y^{\left(\frac{R}{\lambda}\right)}(\theta_z, \phi_x)\, h_y, \tag{6.11}$$

with the scalar,

$$\ell_y^{\left(\frac{R}{\lambda}\right)}(\theta_z, \phi_x) \quad := \quad j2\pi R \frac{J_1\left(2\pi \frac{R}{\lambda} \sqrt{\sin^2(\theta_z)\cos^2(\phi_x) + \cos^2(\theta_z)}\right)}{\sqrt{\sin^2(\theta_z)\cos^2(\phi_x) + \cos^2(\theta_z)}}. \tag{6.12}$$

6.2.4 The loop-triad's new 3×1 array manifold

Sections 6.2.1 to 6.2.3 have derived the voltage of a magnetically large loop at various Cartesian orientations.

Now, consider a triad of such large loops, all with a radius R, co-centered, but orthogonally oriented relative to each other as in Figure 6.2. Such a triad has a 3×1 array manifold of

$$\mathbf{a}^{\left(\frac{R}{\lambda}\right)}(\theta_z, \phi_x, \gamma, \eta) \quad := \quad \begin{bmatrix} \ell_x^{\left(\frac{R}{\lambda}\right)}(\theta_z, \phi_x) \\ \ell_y^{\left(\frac{R}{\lambda}\right)}(\theta_z, \phi_x) \\ \ell_z^{\left(\frac{R}{\lambda}\right)}(\theta_z, \phi_x) \end{bmatrix} \circ \mathbf{h}(\theta_z, \phi_x, \gamma, \eta), \tag{6.13}$$

where $\circ$ denotes element-by-element multiplication.

6.2.5 The Special Case of Magnetically “Small" Loops

The label “small loops" is applied to circular loops with a wavelength-normalized circumference of $2\pi\frac{R}{\lambda} < \frac{1}{10}$. (Please see [68], Section 5.1 and p. 231)[4]

For such magnetically “small" loops: (6.3), (6.7), and (6.11) can be simplified as follows: The argument inside $J_1(\cdot)$ becomes

$$2\pi\frac{R}{\lambda}\sin(\theta) \;<\; \frac{1}{10}\sin(\theta) \;\leq\; \frac{1}{10} \;\ll\; \sqrt{2}, \forall\theta \in [0,\pi].$$

However, for any positive $\kappa \ll \sqrt{2}$ ([98, p. 360]), $J_0'(\kappa) = J_1(\kappa) \approx \frac{\kappa}{2}$. Hence,

$$\begin{aligned}
\boldsymbol{\ell}_x^{\left(\frac{R}{\lambda}<\frac{1}{20\pi}\right)}(\theta_z,\phi_x) &\approx j\frac{2\pi^2R^2}{\lambda}\sin(\theta_x)\,\mathbf{u}_{\phi_y},\\
\boldsymbol{\ell}_z^{\left(\frac{R}{\lambda}<\frac{1}{20\pi}\right)}(\theta_z,\phi_x) &\approx j\frac{2\pi^2R^2}{\lambda}\sin(\theta_z)\,\mathbf{u}_{\phi_x},\\
\boldsymbol{\ell}_y^{\left(\frac{R}{\lambda}<\frac{1}{20\pi}\right)}(\theta_z,\phi_x) &\approx j\frac{2\pi^2R^2}{\lambda}\sin(\theta_y)\,\mathbf{u}_{\phi_z}.
\end{aligned}$$

Using the above results for $R \leq \frac{\lambda}{20\pi}$,

$$\mathbf{a}^{\left(\frac{R}{\lambda}\leq\frac{1}{20\pi}\right)}(\theta,\phi,\gamma,\eta) \;=\; j\frac{2\pi^2R^2}{\lambda}\begin{bmatrix} h_x \\ h_y \\ h_z \end{bmatrix}, \tag{6.14}$$

with an “effective length" of $[1,1,1]^T$.

This (6.14) agrees with [47, 62]. This (6.14) has been used in most signal-processing references for direction finding or polarization estimation, thereby assuming (sometimes only implicitly) that the loops are magnetically “small", despite being electrically *in*efficient. In contrast, the earlier Sections 6.2.1 to 6.2.4 address magnetically large loops that are electrically efficient.

---

[4] Such a magnetically small loop’s radiation pattern is independent of the loop’s shape. Hence, the “effective length" would remain the same for any non-circular shape (like square, elliptical) and would depend only on the loop’s enclosed area [68, p. 231].

6.3 New Closed-Form Estimates of an Incident Source's Azimuth-Elevation Direction-of-Arrival or Polarization

Eigen-based direction-finding algorithms characteristically involve an intermediate step, that estimates each incident source's steering vector, but correct only to within a complex-value scalar c, which is unknown to the algorithm. That is, available is the 3×1 estimate

$$\hat{\mathbf{a}} \;\approx\; c\mathbf{a}^{\left(\frac{R}{\lambda}\right)}(\theta_z, \phi_x, \gamma, \eta), \tag{6.15}$$

from which the direction-of-arrival or the polarization of the impinging electromagnetic wave are to be estimated. (This approximation becomes equality in noiseless or asymptotic cases.)

The unknown complex phase ($\angle c$), can be eliminated from the third entry of $\hat{\mathbf{a}}$ as follows:

$$\begin{aligned}
\bar{\mathbf{a}} \;&:=\; \hat{\mathbf{a}}e^{-j\angle[\hat{\mathbf{a}}]_3} \\
&\approx\; |c| \left\{ \begin{bmatrix} |\ell_x^{\left(\frac{R}{\lambda}\right)}(\theta_z, \phi_x)| \\ |\ell_y^{\left(\frac{R}{\lambda}\right)}(\theta_z, \phi_x)| \\ |\ell_z^{\left(\frac{R}{\lambda}\right)}(\theta_z, \phi_x)| \end{bmatrix} \right. \\
&\quad \left. \odot \begin{bmatrix} -\sin(\phi_x)\sin(\gamma)\cos(\eta) - \cos(\phi_x)\cos(\theta_z)\cos(\gamma) \\ \cos(\phi_x)\sin(\gamma)\cos(\eta) - \sin(\phi_x)\cos(\theta_z)\cos(\gamma) \\ \sin(\theta_z)\cos(\gamma) \end{bmatrix} \right\} \\
&\quad + j|c| \left\{ \begin{bmatrix} |\ell_x^{\left(\frac{R}{\lambda}\right)}(\theta_z, \phi_x)| \\ |\ell_y^{\left(\frac{R}{\lambda}\right)}(\theta_z, \phi_x)| \\ |\ell_z^{\left(\frac{R}{\lambda}\right)}(\theta_z, \phi_x)| \end{bmatrix} \odot \begin{bmatrix} -\sin(\phi_x)\sin(\gamma)\sin(\eta) \\ \cos(\phi_x)\sin(\gamma)\sin(\eta) \\ 0 \end{bmatrix} \right\}.
\end{aligned} \tag{6.16}$$

Here, (6.16) provides 5 real-value constraints from which the bivariate direction-of-arrival or the bivariate polarization can be estimated. There are 5 real-value constraints, because there exist three non-zero components in the real-value part of (6.16) and there exist two non-zero components in the imaginary-value part of (6.16).

6.3.1 Estimation of the Incident Source's Azimuth-Elevation Direction-of-Arrival, (θ_z, ϕ_x)

The following new algorithm estimates an incident source's direction-of-arrival (θ_z, ϕ_x), assuming that the incident source's polarization is prior known.

From (6.16), define

$$\begin{aligned} \alpha_x &:= \frac{\Im\{[\bar{\mathbf{a}}]_1\}}{\Re\{[\bar{\mathbf{a}}]_1\}\sin(\eta) - \Im\{[\bar{\mathbf{a}}]_1\}\cos(\eta)} && (6.17) \\ &= \frac{\tan(\phi_x)\tan(\gamma)}{\cos(\theta_z)}, && (6.18) \end{aligned}$$

$$\begin{aligned} \alpha_y &:= \frac{\Im\{[\bar{\mathbf{a}}]_2\}}{\Im\{[\bar{\mathbf{a}}]_2\}\cos(\eta) - \Re\{[\bar{\mathbf{a}}]_2\}\sin(\eta)} && (6.19) \\ &= \frac{\cot(\phi_x)\tan(\gamma)}{\cos(\theta_z)}, && (6.20) \end{aligned}$$

where $\Re\{.\}$ refers to the real-value part and $\Im\{.\}$ symbolizes the imaginary-value part of the entity inside the curly bracket.

The incident source's bivariate direction-of-arrival may then be estimated as

$$\hat{\phi}_x = \begin{cases} \arctan\left(\left|\frac{\alpha_x}{\alpha_y}\right|^{1/2}\right), & \text{if} \quad \phi_x \in [0, \frac{\pi}{2}), \\ \pi + \arctan\left(-\left|\frac{\alpha_x}{\alpha_y}\right|^{1/2}\right), & \text{if} \quad \phi_x \in [\frac{\pi}{2}, \pi), \\ \pi + \arctan\left|\frac{\alpha_x}{\alpha_y}\right|^{1/2}, & \text{if} \quad \phi_x \in [\pi, \frac{3\pi}{2}), \\ 2\pi + \arctan\left(-\left|\frac{\alpha_x}{\alpha_y}\right|^{1/2}\right), & \text{if} \quad \phi_x \in [\frac{3\pi}{2}, 2\pi); \end{cases} \qquad (6.21)$$

$$\hat{\theta}_z = \arccos\left(\frac{\tan(\gamma)\tan(\hat{\phi}_x)}{\alpha_x}\right). \qquad (6.22)$$

No prior knowledge is needed of the radius R or λ in these new estimation formulas.

6.3.2 Estimation of the Incident Source's Polarization, (γ, η)

The new algorithm below estimates an impinging source's bivariate polarization (γ, η), presuming that the incident source's direction-of-arrival (θ_z, ϕ_x) is prior known.

Taking the ratio of the real and imaginary parts of the first entry of (6.16) gives

$$\frac{\Re\{[\bar{\mathbf{a}}]_1\}}{\Im\{[\bar{\mathbf{a}}]_1\}} = \frac{\cos(\theta_z)}{\tan(\phi_x)\tan(\gamma)\sin(\eta)} + \frac{1}{\tan(\eta)}. \tag{6.23}$$

Taking the ratio of the real and imaginary parts of the second entry of (6.16) gives

$$\frac{\Re\{[\bar{\mathbf{a}}]_2\}}{\Im\{[\bar{\mathbf{a}}]_2\}} = -\frac{\tan(\phi_x)\cos(\theta_z)}{\tan(\gamma)\sin(\eta)} + \frac{1}{\tan(\eta)}. \tag{6.24}$$

Next, relate (6.23) and (6.24) as follows, in order to retain only the one unknown of η,

$$\frac{\Re\{[\bar{\mathbf{a}}]_1\}}{\Im\{[\bar{\mathbf{a}}]_1\}}\tan(\phi_x) + \frac{\Re\{[\bar{\mathbf{a}}]_2\}}{\Im\{[\bar{\mathbf{a}}]_2\}}\cot(\phi_x) = \frac{1}{\tan(\eta)}(\tan(\phi_x) + \cot(\phi_x)). \tag{6.25}$$

As the direction-of-arrival angle ϕ_x has been assumed as prior known, η may be estimated from (6.25) as

$$\hat{\eta} = \arctan\left\{\frac{\tan(\phi_x) + \cot(\phi_x)}{\frac{\Re\{[\bar{\mathbf{a}}]_1\}}{\Im\{[\bar{\mathbf{a}}]_1\}}\tan(\phi_x) + \frac{\Re\{[\bar{\mathbf{a}}]_2\}}{\Im\{[\bar{\mathbf{a}}]_2\}}\cot(\phi_x)}\right\}. \tag{6.26}$$

From the ratios of the real and imaginary parts of the first and second entries of (6.16), one additional constraint can be obtained:

$$\frac{\Re\{[\bar{\mathbf{a}}]_1\}}{\Im\{[\bar{\mathbf{a}}]_1\}} - \frac{\Re\{[\bar{\mathbf{a}}]_2\}}{\Im\{[\bar{\mathbf{a}}]_2\}} = \frac{\cos(\theta_z)}{\tan(\gamma)\sin(\eta)}(\cot(\phi_x) + \tan(\phi_x)). \tag{6.27}$$

As η is already estimated, multiply $\sin(\hat{\eta})$ to both sides of (6.27), in order to obtain

$$\sin(\hat{\eta})\left(\frac{\Re\{[\bar{\mathbf{a}}]_1\}}{\Im\{[\bar{\mathbf{a}}]_1\}}-\frac{\Re\{[\bar{\mathbf{a}}]_2\}}{\Im\{[\bar{\mathbf{a}}]_2\}}\right) = \frac{\cos(\theta_z)}{\tan(\gamma)}[\cot(\phi_x)+\tan(\phi_x)]. \tag{6.28}$$

With θ_z and ϕ_x presumed known, γ can be estimated from (6.28) as

$$\hat{\gamma} = \arctan\left\{\frac{[\cot(\phi_x)+\tan(\phi_x)]\cos(\theta_z)}{\sin(\hat{\eta})\left[\frac{\Re\{[\bar{\mathbf{a}}]_1\}}{\Im\{[\bar{\mathbf{a}}]_1\}}-\frac{\Re\{[\bar{\mathbf{a}}]_2\}}{\Im\{[\bar{\mathbf{a}}]_2\}}\right]}\right\}. \tag{6.29}$$

No prior knowledge of R nor λ is needed by these estimators.

6.4 Monte Carlo Simulations

To verify the efficacy of the eigen-based estimators proposed in Section 6.3, Monte Carlo simulations are conducted in this section.

To focus on the influence of the loop-antenna's physical radius R, a simple data model will be used below: A zero-mean complex-value Gaussian noise signal $s(m)$, impinges upon a triad of large loops, which have been described earlier. At the mth time-instant, the triad collects the 3×1 data-vector,

$$\mathbf{z}(m) = \mathbf{a}^{\left(\frac{R}{\lambda}\right)}(\theta_z,\phi_x,\gamma,\eta)s(m)+\mathbf{n}(m). \tag{6.30}$$

Moreover, the additive noise $\mathbf{n}(m)$ denotes a 3×1 vector of zero-mean complex-value Gaussian noise of a prior known variance of σ_n^2, circularly symmetric in distribution on the complex plane, spatio-temporally uncorrelated over time and across the loops, while statistically independent from all other entities, hence with a deterministic covariance matrix of $\mathbf{\Gamma}_0 = \mathrm{diag}\left(\sigma_n^2,\sigma_n^2,\sigma_n^2\right)$, where σ_n^2 represents the noise variance at each loop.

With M number of time-samples, the $3M\times 1$ collected data-set equals

$$\boldsymbol{\zeta} = \left[(\mathbf{z}(1))^T,\cdots,(\mathbf{z}(M))^T\right]^T. \tag{6.31}$$

In all subsequent numerical examples: $M = 100$, $\phi_x = 45^o$, $\theta_z = 60^o$, $\gamma = 45^o$, and $\eta = 60^o$. Each icon on every graph represents $1,000$ independent Monte Carlo experiments.

6.4.1 Estimation of the Incident Source's Azimuth-Elevation Direction-of-Arrival, (ϕ_x, θ_z)

Using the new algorithm proposed earlier in Section 6.3.1 for direction finding, Monte Carlo simulation results are presented in Figures 6.3a- 6.3b, along with the corresponding Cramér-Rao bounds (CRB) for comparison. These Cramér-Rao bounds have been derived in Appendix A. (Recall that the Cramér-Rao bound lower-bounds the estimation error variance of any unbiased estimator; and the Cramér-Rao bound itself is independent of the specific estimator employed.) Figures 6.3a-6.3b indicate that the estimation method proposed in Section 6.3.1 performs close to the Cramér-Rao bounds.

Recall that the "effective length" affects the loop's gain, nonlinearly and non-monotonically in (6.2-6.9), through Bessel functions. Figures 6.3a-6.3b further suggest that the larger the loop, the more accurate the estimates would be.

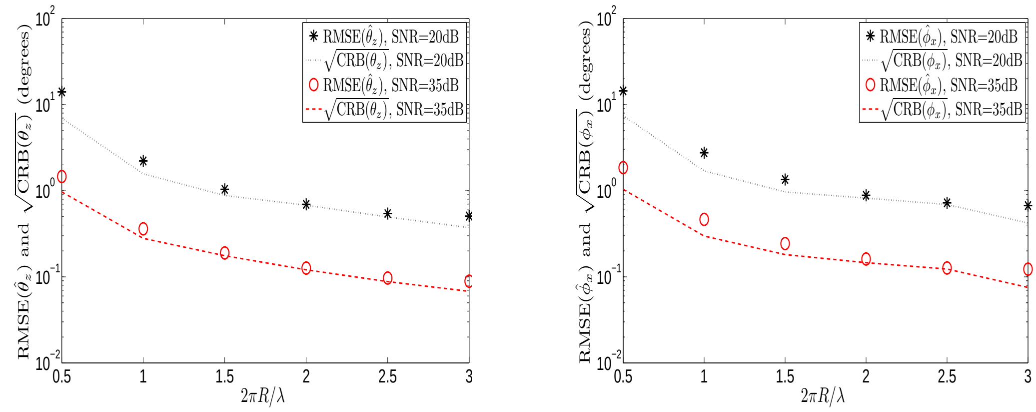

(a) RMSE and $\sqrt{\text{CRB}}$ for $\hat{\theta}_z$, at SNR $= 20, 35$dB.

(b) RMSE and $\sqrt{\text{CRB}}$ for $\hat{\phi}_x$, at SNR $= 20, 35$dB.

Fig. 6.3.: RMSE and $\sqrt{\text{CRB}}$ for $\hat{\theta}_z$ and $\hat{\phi}_x$ versus $\frac{R}{\lambda}$ using loop triad.

6.4.2 Estimation of the Incident Source's Polarization, (γ, η)

Using the new algorithms proposed earlier in Section 6.3.2 for polarization estimation, Monte Carlo simulation results are presented in Figures 6.4a-6.4b, along with the corresponding Cramér-Rao bounds (CRB) for comparison. These Cramér-Rao bounds have been derived in Appendix B.

Figures 6.4a-6.4b indicate that the estimation method proposed in Section 6.3.2 is close to the Cramér-Rao bounds. These figures also reinforce the point that the larger the loop, the more accurate the estimates would be.

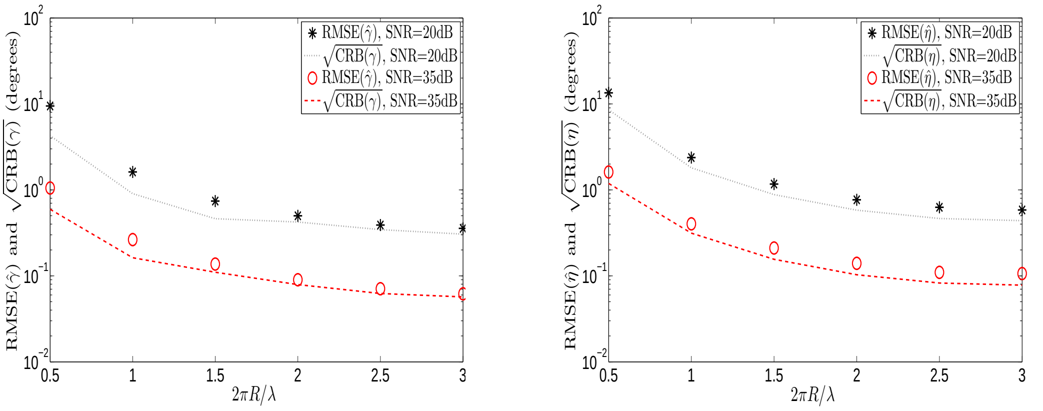

(a) RMSE and $\sqrt{\mathrm{CRB}}$ for $\hat{\gamma}$, at SNR $= 20, 35$dB.

(b) RMSE and $\sqrt{\mathrm{CRB}}$ for $\hat{\eta}$, at SNR $= 20, 35$dB.

Fig. 6.4.: RMSE and $\sqrt{\mathrm{CRB}}$ for $\hat{\gamma}$ and $\hat{\eta}$ versus $\frac{R}{\lambda}$ using loop triad.

6.5 Conclusion

Magnetically large loops are considered for the first time in the open literature (to the present authors' best knowledge) to develop signal-processing algorithms to estimate incident emitters' direction-of-arrival or polarization without any prior knowledge of the loop's radius or of the incident signal's wavelength. Despite that the magnetically large loops' gain pattern involves the Bessel function, closed-form estimation algorithms are developed here, not requiring any iterative search. These proposed algorithms can approach the Cramér-Rao lower bound.

Conclusion

7

Electrically "short" dipoles have very small input impedances, rendering them to be poor radiators. Practical dipoles, with an physical length of $L \in [0.1, 1]\lambda$, have notably larger input impedances, hence making them better radiators. Similarly electrically "small" loops have very small input impedances, whereas practical loops with circumference of $2\pi R \in [0.1, 1]\lambda$ have larger input impedances making them relatively much better radiators. Despite that the electrically "long" dipoles and "large" loops have better radiation efficiencies, the focus of research in antenna array signal-processing algorithm development has been on electrically "short" dipoles and "small" loops. This study was an attempt to investigate the estimation of bivariate polar-azimuth direction-of-arrival and bivariate polarization using electrically "long" dipoles and "large" loops.

The concept of "effective length" was used here to relate an electrically "long" dipole's directional-polarizational pattern to the incident electric field to establish the measurement model (i.e. array manifold) of such practical dipoles, as a triad that is collocated in space and orthogonal in orientation. Closed-form algorithms were developed using a triad of electrically "long" dipoles to estimate incident sources' bivariate azimuth-elevation directions-of-arrival and bivariate polarizations.

The triad's collocation gives a point-like spatial aperture, limiting the dipole-array's spatial resolution. To realize a large spatial aperture, electrically long dipoles can be positioned sparsely on a circular circumference, with each dipole oriented radially (or tangentially), to allow a rotational invariance with respect to the circle's origin. For such a circular array of sparsely spaced and differently oriented dipoles, this thesis also developed the measurement model using the concept of "effective length" and pioneered closed-form algorithms to estimate incident sources' bivariate azimuth-elevation directions-of-arrival and bivariate polarizations.

For two electrically long dipoles, this thesis also pioneered signal-processing algorithms in closed forms, to estimate the polarizations of impinging sources. This is unlike the vast literature on crossed-dipoles polarimetry, restricted to electrically short dipoles. In this thesis, the two long dipoles are perpendicularly oriented, but may be collocated or may be separated by a known displacement. Using such a pair of electrically long dipoles for polarization estimation, this thesis proposed new closed-form formulas, and derived the associated Cramér-Rao bounds.

This thesis also established a similar array manifold's generalization of a triad of large loops, collocated and orthogonal in orientation. Then for such a triad of large loops, this thesis pioneered closed-form signal processing algorithms to estimate the incident signals azimuth-elevation directions-of-arrival and polarizations.

Monte Carlo experiments show that the estimation performed using dipoles have significantly better performance at a longer electrical length and a larger signal-to-noise ratio. A similar trend is observed when estimation is performed using loop antennas. It is also observed that the proposed estimators can closely approach the Cramér-Rao bounds.

Appendices

A

The Cramér-Rao Bound for Direction Finding

Define $\mathbf{a}$ to be the array manifold of the triad ($\mathbf{a} := \mathbf{a}^{(\frac{R}{\lambda})}$ for loop triad and $\mathbf{a} := \mathbf{a}^{(L)}$ for dipole triad). A zero-mean complex-value Gaussian noise signal $\mathbf{s}(m)$, impinges upon the triad. At mth time-instant, the triad collects the 3×1 data-vector,

$$\mathbf{z}(m) \quad = \quad \mathbf{a}s(m) + \mathbf{n}(m). \tag{A.1}$$

Moreover, the additive noise $\mathbf{n}(m)$ denotes a 3×1 vector of zero-mean complex-value Gaussian additive noise, spatio-temporally uncorrelated over time and across the antennas, while statistically independent from all other entities, hence with a deterministic covariance matrix of $\mathbf{\Gamma}_0 = \mathrm{diag}\left(\sigma_n^2, \sigma_n^2, \sigma_n^2\right)$, where σ_n^2 representing the noise variance at each antenna.

With M number of time-samples, the $3M \times 1$ collected data-set equals

$$\boldsymbol{\zeta} \quad = \quad \mathbf{s} \otimes \mathbf{a} + \underbrace{\left[(\mathbf{n}(M))^T, \cdots, (\mathbf{n}(M))^T\right]^T}_{=\boldsymbol{\nu}}, \tag{A.2}$$

where s is an $M \times 1$ vector with entries that are complex-value zero-mean Gaussian, with a covariance matrix of $\mathbf{\Gamma}_s = \sigma_s^2 \mathbf{I}_M$, and statistically independent of each other. Here, $\mathbf{I}_M$ denotes an $M \times M$ identity matrix, and $\otimes$ represents the Kronecker product. Moreover, $\boldsymbol{\nu}$ symbolizes a $3M \times 1$ noise vector having a spatio-temporal covariance matrix of $\mathbf{\Gamma}_n = \mathbf{I}_M \otimes \mathbf{\Gamma}_0$.

Recall that both the direction-finding formulas in Section 3.4.1 for the dipole case and Section 6.3.1 for the loop case require no prior information on electrical length κ, and σ_n^2. $\kappa := \frac{L}{\lambda}$ for dipole case and $\kappa := \frac{L}{\lambda}$ for loop case. To match these statistical models of the data, the Fisher information matrix (FIM) is 4×4 in size:

$$\mathbf{J} \quad = \quad \begin{bmatrix} J_{\theta_z,\theta_z} & J_{\theta_z,\phi_x} & J_{\theta_z,\kappa} & J_{\theta_z,\sigma_n^2} \\ J_{\phi_x,\theta_z} & J_{\phi_x,\phi_x} & J_{\phi_x,\kappa} & J_{\phi_x,\sigma_n^2} \\ J_{\kappa,\theta_z} & J_{\kappa,\phi_x} & J_{\kappa,\kappa} & J_{\kappa,\sigma_n^2} \\ J_{\sigma_n^2,\theta_z} & J_{\sigma_n^2,\phi_x} & J_{\sigma_n^2,\kappa} & J_{\sigma_n^2,\sigma_n^2} \end{bmatrix}, \tag{A.3}$$

whose (i,j)th entry can be derived using (see equation (8.34) of [66]):

$$[\mathbf{J}]_{i,j} \;=\; \mathrm{Tr}\left(\boldsymbol{\Gamma}^{-1}\frac{\partial\boldsymbol{\Gamma}}{\partial[\boldsymbol{\psi}]_i}\boldsymbol{\Gamma}^{-1}\frac{\partial\boldsymbol{\Gamma}}{\partial[\boldsymbol{\psi}]_j}\right), \tag{A.4}$$

where $\mathrm{Tr}(\cdot)$ represents the trace operator and $[\boldsymbol{\psi}]_i$ and $[\boldsymbol{\psi}]_j$ represent corresponding subscripts. That equation (8.34) may be used, because the collected data vector, $\boldsymbol{\zeta}$, has entries here that are Gaussian, zero-mean, and with a covariance matrix of $\boldsymbol{\Gamma} = \mathbf{I}_M \otimes \sigma_s^2\mathbf{a}\mathbf{a}^H + \mathbf{I}_M \otimes \boldsymbol{\Gamma}_0$.

The inverse of the above Fisher information matrix gives

$$\begin{aligned}\mathrm{CRB} \;=\; &\left[\begin{bmatrix} J_{\theta_z,\theta_z} & J_{\theta_z,\phi_x} \\ J_{\phi_x,\theta_z} & J_{\phi_x,\phi_x}\end{bmatrix} - \begin{bmatrix} J_{\theta_z,\kappa} & J_{\theta_z,\sigma_n^2} \\ J_{\phi_x,\kappa} & J_{\phi_x,\sigma_n^2}\end{bmatrix}\right.\\ &\left.\begin{bmatrix} J_{\kappa,\kappa} & J_{\kappa,\sigma_n^2} \\ J_{\sigma_n^2,\kappa} & J_{\sigma_n^2,\sigma_n^2}\end{bmatrix}^{-1}\begin{bmatrix} J_{\kappa,\theta_z} & J_{\kappa,\phi_x} \\ J_{\sigma_n^2,\theta_z} & J_{\sigma_n^2,\phi_x}\end{bmatrix}\right]^{-1},\end{aligned} \tag{A.5}$$

where

$$\begin{aligned}
J_{\theta_z,\theta_z} &= M\mathrm{Tr}\left(\left[\boldsymbol{M}_1^{-1}\boldsymbol{M}_2\right]^2\right), \\
J_{\theta_z,\phi_x} &= J^*_{\phi_x,\theta_z} \\
&= M\mathrm{Tr}\left(\boldsymbol{M}_1^{-1}\boldsymbol{M}_2\boldsymbol{M}_1^{-1}\boldsymbol{M}_3\right), \\
J_{\theta_z,\kappa} &= J^*_{\kappa,\theta_z} \\
&= M\mathrm{Tr}\left(\boldsymbol{M}_1^{-1}\boldsymbol{M}_2\boldsymbol{M}_1^{-1}\boldsymbol{M}_4\right), \\
J_{\theta_z,\sigma_n^2} &= J^*_{\sigma_n^2,\theta_z} \\
&= M\mathrm{Tr}\left(\boldsymbol{M}_1^{-1}\boldsymbol{M}_2\boldsymbol{M}_1^{-1}\right) \\
J_{\phi_x,\phi_x} &= M\mathrm{Tr}\left(\left[\boldsymbol{M}_1^{-1}\boldsymbol{M}_3\right]^2\right), \\
J_{\phi_x,\kappa} &= J^*_{\kappa,\phi_x} \\
&= M\mathrm{Tr}\left(\boldsymbol{M}_1^{-1}\boldsymbol{M}_3\boldsymbol{M}_1^{-1}\boldsymbol{M}_4\right), \\
J_{\phi_x,\sigma_n^2} &= J^*_{\sigma_n^2,\phi_x} \\
&= M\mathrm{Tr}\left(\boldsymbol{M}_1^{-1}\boldsymbol{M}_3\boldsymbol{M}_1^{-1}\right), \\
J_{\kappa,\kappa} &= M\mathrm{Tr}\left(\left[\boldsymbol{M}_1^{-1}\boldsymbol{M}_4\right]^2\right), \\
J_{\kappa,\sigma_n^2} &= J^*_{\sigma_n^2,\kappa} \\
&= M\mathrm{Tr}\left(\boldsymbol{M}_1^{-1}\boldsymbol{M}_4\boldsymbol{M}_1^{-1}\right), \\
J_{\sigma_n^2,\sigma_n^2} &= M\mathrm{Tr}\left(\boldsymbol{M}_1^{-2}\right).
\end{aligned} \tag{A.6}$$

In the above, the superscript * denotes complex conjugation and

$$\begin{aligned}
\mathbf{M}_1 &:= \mathbf{\Gamma}_0 + \sigma_s^2 \mathbf{a}\mathbf{a}^H, \\
\mathbf{M}_2 &:= \tfrac{\partial}{\partial \theta_z} \left(\sigma_s^2 \mathbf{a}\mathbf{a}^H \right), \\
\mathbf{M}_3 &:= \tfrac{\partial}{\partial \phi_x} \left(\sigma_s^2 \mathbf{a}\mathbf{a}^H \right), \\
\mathbf{M}_4 &:= \tfrac{\partial}{\partial \kappa} \left(\sigma_s^2 \mathbf{a}\mathbf{a}^H \right).
\end{aligned} \tag{A.7}$$

B

The Cramér-Rao Bound for Polarization Estimation

Equation (A.2) in Appendix A remains valid here. FIM here is also 4×4 in size to match the estimation formulas in Section 3.4.2 for dipole triad and Section 6.3.2 for loop triad as no prior information on κ, σ_n^2 is required:

$$\mathbf{J} = \begin{bmatrix} J_{\gamma,\gamma} & J_{\gamma,\eta} & J_{\gamma,\kappa} & J_{\gamma,\sigma_n^2} \\ J_{\eta,\gamma} & J_{\eta,\eta} & J_{\eta,\kappa} & J_{\eta,\sigma_n^2} \\ J_{\kappa,\gamma} & J_{\kappa,\eta} & J_{\kappa,\kappa} & J_{\kappa,\sigma_n^2} \\ J_{\sigma_n^2,\gamma} & J_{\sigma_n^2,\eta} & J_{\sigma_n^2,\kappa} & J_{\sigma_n^2,\sigma_n^2} \end{bmatrix}, \tag{B.1}$$

has its (i,j)th entry as given by (A.4). Therefore,

$$\begin{aligned} \text{CRB} &= \left[\begin{bmatrix} J_{\gamma,\gamma} & J_{\gamma,\eta} \\ J_{\eta,\gamma} & J_{\eta,\eta} \end{bmatrix} - \begin{bmatrix} J_{\gamma,\kappa} & J_{\gamma,\sigma_n^2} \\ J_{\eta,\kappa} & J_{\eta,\sigma_n^2} \end{bmatrix} \right. \\ & \left. \begin{bmatrix} J_{\kappa,\kappa} & J_{\kappa,\sigma_n^2} \\ J_{\sigma_n^2,\kappa} & J_{\sigma_n^2,\sigma_n^2} \end{bmatrix}^{-1} \begin{bmatrix} J_{\kappa,\gamma} & J_{\kappa,\eta} \\ J_{\sigma_n^2,\gamma} & J_{\sigma_n^2,\eta} \end{bmatrix} \right]^{-1}, \end{aligned} \tag{B.2}$$

where

$$\begin{aligned} J_{\gamma,\gamma} &= M\mathrm{Tr}\left(\left[\boldsymbol{M}_1^{-1} \boldsymbol{M}_5 \right]^2 \right), \\ J_{\gamma,\eta} &= J^*_{\eta,\gamma} \\ &= M\mathrm{Tr}\left(\boldsymbol{M}_1^{-1} \boldsymbol{M}_5 \boldsymbol{M}_1^{-1} \boldsymbol{M}_6 \right), \\ J_{\gamma,\kappa} &= J^*_{\kappa,\gamma} \\ &= M\mathrm{Tr}\left(\boldsymbol{M}_1^{-1} \boldsymbol{M}_5 \boldsymbol{M}_1^{-1} \boldsymbol{M}_4 \right), \\ J_{\gamma,\sigma_n^2} &= J^*_{\sigma_n^2,\gamma} \\ &= M\mathrm{Tr}\left(\boldsymbol{M}_1^{-1} \boldsymbol{M}_5 \boldsymbol{M}_1^{-1} \right), \\ J_{\eta,\eta} &= M\mathrm{Tr}\left(\left[\boldsymbol{M}_1^{-1} \boldsymbol{M}_6 \right]^2 \right), \\ J_{\eta,\kappa} &= J^*_{\kappa,\eta} \\ &= M\mathrm{Tr}\left(\boldsymbol{M}_1^{-1} \boldsymbol{M}_6 \boldsymbol{M}_1^{-1} \boldsymbol{M}_4 \right), \\ J_{\eta,\sigma_n^2} &= J^*_{\sigma_n^2\eta} \\ &= M\mathrm{Tr}\left(\boldsymbol{M}_1^{-1} \boldsymbol{M}_6 \boldsymbol{M}_1^{-1} \right), \end{aligned} \tag{B.3}$$

the expression for $\boldsymbol{M}_1$ is given by (A.7), and

$$\begin{aligned} \boldsymbol{M}_5 &:= \tfrac{\partial}{\partial \gamma}\left(\sigma_s^2 \mathbf{a}\mathbf{a}^H\right), \\ \boldsymbol{M}_6 &:= \tfrac{\partial}{\partial \eta}\left(\sigma_s^2 \mathbf{a}\mathbf{a}^H\right). \end{aligned} \tag{B.4}$$

C

The Deterministic Cramér-Rao Bound for Simultaneous DoA and Polarization Estimation

For the simultaneous direction finding and polarization estimation using dipole triad, consider the data model to be the same as in Appendix A but now $\mathbf{s} = \sigma_s \left[e^{jf_d}, e^{j2f_d}, \cdots, e^{jMf_d} \right]^T$. Here, the $3M \times 1$ dataset may still be represented by equation (A.2) but now $\boldsymbol{\zeta} \sim \mathcal{N}(\boldsymbol{\mu}, \boldsymbol{\Gamma})$, i.e. a $3M \times 1$ Gaussian vector with a $3M \times 1$ mean of $\boldsymbol{\mu}$ and a $3M \times 3M$ covariance of $\boldsymbol{\Gamma}$.

Collect all deterministic unknown entities into a 4×1 vector of $\boldsymbol{\psi} = [\theta_z, \phi_x, \gamma, \eta]^T$ to match the statistical data model in Section 3.5. The resulting 4×4 Fisher information matrix equals

$$\mathbf{J} = \begin{bmatrix} J_{\theta_z,\theta_z} & J_{\theta_z,\phi_x} & J_{\theta_z,\gamma} & J_{\theta_z,\eta} \\ J_{\phi_x,\theta_z} & J_{\phi_x,\phi_x} & J_{\phi_x,\gamma} & J_{\phi_x,\eta} \\ J_{\gamma,\theta_z} & J_{\gamma,\phi_x} & J_{\gamma,\gamma} & J_{\gamma,\eta} \\ J_{\eta,\theta_z} & J_{\eta,\phi_x} & J_{\eta,\gamma} & J_{\eta,\eta} \end{bmatrix}, \tag{C.1}$$

whose (i, j)th entry equals (see equation (8.34) of [66]):

$$\begin{aligned} [\mathbf{J}]_{i,j} &= 2\Re\left\{ \left(\frac{\partial \boldsymbol{\mu}}{\partial [\boldsymbol{\psi}]_i} \right)^H \boldsymbol{\Gamma}^{-1} \left(\frac{\partial \boldsymbol{\mu}}{\partial [\boldsymbol{\psi}]_j} \right) \right\} \\ &\quad + \mathrm{Tr}\left[\boldsymbol{\Gamma}^{-1} \frac{\partial \boldsymbol{\Gamma}}{\partial [\boldsymbol{\psi}]_i} \boldsymbol{\Gamma}^{-1} \frac{\partial \boldsymbol{\Gamma}}{\partial [\boldsymbol{\psi}]_j} \right], \end{aligned} \tag{C.2}$$

where

$$\frac{\partial \boldsymbol{\mu}}{\partial \theta_z} = \frac{\partial \mathbf{a}^{(L)}}{\partial \theta_z} \otimes \mathbf{s}, \tag{C.3}$$

$$\frac{\partial \boldsymbol{\mu}}{\partial \phi_x} = \frac{\partial \mathbf{a}^{(L)}}{\partial \phi_x} \otimes \mathbf{s}, \tag{C.4}$$

$$\frac{\partial \boldsymbol{\mu}}{\partial \gamma} = \frac{\partial \mathbf{a}^{(L)}}{\partial \gamma} \otimes \mathbf{s}, \tag{C.5}$$

(C.6)

$$\frac{\partial \boldsymbol{\mu}}{\partial \eta} = \frac{\partial \mathbf{a}^{(L)}}{\partial \eta} \otimes \mathbf{s}, \tag{C.7}$$

$$\frac{\partial \boldsymbol{\Gamma}}{\partial [\boldsymbol{\psi}]_i} = \mathbf{0}, \quad \forall i = \{1, 2, 3, 4\}. \tag{C.8}$$

Further mathematical manipulations would give

$$[\mathbf{J}]_{i,j} = 2M \left(\frac{\sigma_s}{\sigma_n}\right)^2 \Re \left\{ \left[\frac{\partial \mathbf{a}^{(L)}}{\partial [\boldsymbol{\psi}]_i}\right]^H \frac{\partial \mathbf{a}^{(L)}}{\partial [\boldsymbol{\psi}]_j} \right\}. \tag{C.9}$$

Hence, $\mathbf{J} \propto M \left(\frac{\sigma_s}{\sigma_n}\right)^2$ for $\forall \frac{L}{\lambda}, \theta_z, \phi_x, \gamma, \eta$. Consequentially, CRB is inversely proportional to the number (M) of snapshots and to the signal-to-noise power ratio (SNR) of $\left(\frac{\sigma_s}{\sigma_n}\right)^2$.

D

Cramér-Rao Bounds of Unbiased Estimation of a Source's DoA and Polarization

Consider a uniform circular array of I number of electrically long dipoles with array manifold given by $\mathbf{a}$. A zero-mean complex-value Gaussian noise signal $\mathrm{s}(m)$, impinges upon the UCA. At mth time-instant, the UCA collects the $I \times 1$ data-vector,

$$\mathbf{z}(m) \quad = \quad \mathbf{a}s(m) + \mathbf{n}(m). \tag{D.1}$$

Moreover, the additive noise $\mathbf{n}(m)$ denotes an $I \times 1$ vector of zero-mean complex-value Gaussian additive noise, spatio-temporally uncorrelated over time and across the dipoles, while statistically independent from all other entities, hence with a deterministic covariance matrix of $\mathbf{\Gamma}_0 = \sigma_n^2 \boldsymbol{I}_I$, where σ_n^2 representing the noise variance at each dipole and $\boldsymbol{I}_I$ is an $I \times I$ identity matrix.

With M number of time-samples, the $I \times M$ space-time data matrix represented by $\mathbf{Z}$ in Section 4.3 can be arranged as an $IM \times 1$ vector

$$\boldsymbol{\zeta} \quad = \quad \left[(\mathbf{z}(1))^T, \cdots, (\mathbf{z}(M))^T\right]^T \tag{D.2}$$

or

$$\boldsymbol{\zeta} \quad = \quad \mathbf{s} \otimes \mathbf{a} + \underbrace{\left[(\mathbf{n}(1))^T, \cdots, (\mathbf{n}(M))^T\right]^T}_{=\boldsymbol{\nu}} \tag{D.3}$$

where s is an $M \times 1$ vector with entries that are complex-value zero-mean Gaussian, statistically independent of each other and with a covariance matrix of $\mathbf{\Gamma}_s = \sigma_s^2 \mathbf{I}_M$. Here, $\mathbf{I}_M$ denotes an $M \times M$ identity matrix, $\otimes$ symbolizes the Kronecker product, and superscript ^{T} denotes the transpose operator. Moreover, $\boldsymbol{\nu}$ represents an $IM \times 1$ noise vector with a spatio-temporal covariance matrix of $\mathbf{\Gamma}_n = \sigma_n^2 \mathbf{I}_M \otimes \boldsymbol{I}_I$. Lastly, $\mathbf{a} := \mathbf{a}_{\mathrm{r}}$ for the array configuration in Figure 4.1 and $\mathbf{a} := \mathbf{a}_{\text{tn}}$ for the array configuration of Figure 4.2.

Define a 6×1 vector of $\boldsymbol{\psi} = [\theta_z, \phi_x, \gamma, \eta, \sigma_n^2, \sigma_s^2]^T$. Since the simultaneous direction finding and polarization estimation in Section 4.4 do not require prior knowledge of σ_n^2 and σ_s^2, the Fisher information matrix (FIM) is to be 6×6 in size:

$$\mathbf{J} = \begin{bmatrix} J_{\theta_z,\theta_z} & J_{\theta_z,\phi_x} & J_{\theta_z,\gamma} & J_{\theta_z,\eta} & J_{\theta_z,\sigma_n^2} & J_{\theta_z,\sigma_s^2} \\ J_{\phi_x,\theta_z} & J_{\phi_x,\phi_x} & J_{\phi_x,\gamma} & J_{\phi_x,\eta} & J_{\phi_x,\sigma_n^2} & J_{\phi_x,\sigma_s^2} \\ J_{\gamma,\theta_z} & J_{\gamma,\phi_x} & J_{\gamma,\gamma} & J_{\gamma,\eta} & J_{\gamma,\sigma_n^2} & J_{\gamma,\sigma_s^2} \\ J_{\eta,\theta_z} & J_{\eta,\phi_x} & J_{\eta,\gamma} & J_{\eta,\eta} & J_{\eta,\sigma_n^2} & J_{\eta,\sigma_s^2} \\ J_{\sigma_n^2,\theta_z} & J_{\sigma_n^2,\phi_x} & J_{\sigma_n^2,\gamma} & J_{\sigma_n^2,\eta} & J_{\sigma_n^2,\sigma_n^2} & J_{\sigma_n^2,\sigma_s^2} \\ J_{\sigma_s^2,\theta_z} & J_{\sigma_s^2,\phi_x} & J_{\sigma_s^2,\gamma} & J_{\sigma_s^2,\eta} & J_{\sigma_s^2,\sigma_n^2} & J_{\sigma_s^2,\sigma_s^2} \end{bmatrix} \tag{D.4}$$

whose (i, j)th entry equals (see equation (8.34) of [66])[1]

$$[\mathbf{J}]_{i,j} = \text{Tr}\left(\boldsymbol{\Gamma}^{-1}\frac{\partial\boldsymbol{\Gamma}}{\partial[\boldsymbol{\psi}]_i}\boldsymbol{\Gamma}^{-1}\frac{\partial\boldsymbol{\Gamma}}{\partial[\boldsymbol{\psi}]_j}\right), \tag{D.5}$$

where $\text{Tr}(\cdot)$ represents the trace operator. Using simple mathematical manipulations,

$$\begin{aligned} [\mathbf{J}]_{i,j} &= J_{[\boldsymbol{\psi}]_i,[\boldsymbol{\psi}]_j} \\ &= \left(\frac{\sigma_s}{\sigma_n}\right)^4 M\,\text{Tr}\left(\left[\mathbf{M}^{-1}\mathbf{M}_{[\boldsymbol{\psi}]_i}\mathbf{M}^{-1}\mathbf{M}_{[\boldsymbol{\psi}]_j}\right]\right) \end{aligned} \tag{D.6}$$

and

$$\begin{aligned} \mathbf{M} &:= \mathbf{I}_I + \left(\frac{\sigma_s}{\sigma_n}\right)^2 \mathbf{a}\mathbf{a}^H, \\ \mathbf{M}_{\theta_z} &:= \frac{\partial}{\partial\theta_z}\left(\mathbf{a}\mathbf{a}^H\right), \\ \mathbf{M}_{\phi_x} &:= \frac{\partial}{\partial\phi_x}\left(\mathbf{a}\mathbf{a}^H\right), \\ \mathbf{M}_{\gamma} &:= \frac{\partial}{\partial\gamma}\left(\mathbf{a}\mathbf{a}^H\right), \\ \mathbf{M}_{\eta} &:= \frac{\partial}{\partial\eta}\left(\mathbf{a}\mathbf{a}^H\right), \\ \mathbf{M}_{\sigma_n^2} &:= \frac{1}{\sigma_s^2}\mathbf{I}_I, \\ \mathbf{M}_{\sigma_s^2} &:= \frac{1}{\sigma_s^2}\mathbf{a}\mathbf{a}^H. \end{aligned}$$

---

[1] That equation (8.34) may be used, because the collected data vector, $\boldsymbol{\zeta}$, has entries here that are Gaussian, zero-mean, and with a covariance matrix of $\boldsymbol{\Gamma} = \mathbf{I}_M \otimes \left(\boldsymbol{\Gamma}_0 + \sigma_s^2\mathbf{a}\mathbf{a}^H\right)$.

From (D.4),

$$\begin{bmatrix} \text{CRB}(\theta_z) & * & * & * \\ * & \text{CRB}(\phi_x) & * & * \\ * & * & \text{CRB}(\gamma) & * \\ * & * & * & \text{CRB}(\eta) \end{bmatrix}$$

$$= \left[\begin{bmatrix} J_{\theta_z,\theta_z} & J_{\theta_z,\phi_x} & J_{\theta_z,\gamma} & J_{\theta_z,\eta} \\ J_{\phi_x,\theta_z} & J_{\phi_x,\phi_x} & J_{\phi_x,\gamma} & J_{\phi_x,\eta} \\ J_{\gamma,\theta_z} & J_{\gamma,\phi_x} & J_{\gamma,\gamma} & J_{\gamma,\eta} \\ J_{\eta,\theta_z} & J_{\eta,\phi_x} & J_{\eta,\gamma} & J_{\eta,\eta} \end{bmatrix} - \begin{bmatrix} J_{\theta_z,\sigma_n^2} & J_{\theta_z,\sigma_s^2} \\ J_{\phi_x,\sigma_n^2} & J_{\phi_x,\sigma_s^2} \\ J_{\gamma,\sigma_n^2} & J_{\gamma,\sigma_s^2} \\ J_{\eta,\sigma_n^2} & J_{\eta,\sigma_s^2} \end{bmatrix} \begin{bmatrix} J_{\sigma_n^2,\sigma_n^2} & J_{\sigma_n^2,\sigma_s^2} \\ J_{\sigma_s^2,\sigma_n^2} & J_{\sigma_s^2,\sigma_s^2} \end{bmatrix} \right.$$

$$\left. \times \begin{bmatrix} J_{\sigma_n^2,\theta_z} & J_{\sigma_n^2,\phi_x} & J_{\sigma_n^2,\gamma} & J_{\sigma_n^2,\eta} \\ J_{\sigma_s^2,\theta_z} & J_{\sigma_s^2,\phi_x} & J_{\sigma_s^2,\gamma} & J_{\sigma_s^2,\eta} \end{bmatrix} \right]^{-1} . \quad \text{(D.7)}$$

In the above, the $*$ entries are not of interest to the present investigation.

Bibliography

[1] T. S. Rappaport, *Wireless Communications: Principles and Practice*, 2 edition. Upper Saddle River, N.J: Prentice Hall, 2002.

[2] L. C. Godara, “Application of antenna arrays to mobile communications. II. Beam-forming and direction-of-arrival considerations”, *Proceedings of the IEEE*, vol. 85, no. 8, pp. 1195-1245, Aug. 1997.

[3] B. D. V. Veen and K. M. Buckley, “Beamforming: a versatile approach to spatial filtering”, *IEEE ASSP Magazine*, vol. 5, no. 2, pp. 4-24, Apr. 1988.

[4] L. C. Godara, “Limitations and capabilities of directions-of-arrival estimation techniques using an array of antennas: a mobile communications perspective,” in *IEEE International Symposium on Phased Array Systems and Technology*, pp. 327-333, 1996.

[5] G. Mao, B. Fidan, and B. D. O. Anderson, “Wireless sensor network localization techniques”, *Computer Networks*, vol. 51, no. 10, pp. 2529-2553, Jul. 2007.

[6] T. Basikolo and H. Arai, “APRD-MUSIC Algorithm DOA Estimation for Reactance Based Uniform Circular Array”, *IEEE Transactions on Antennas and Propagation*, vol. 64, no. 10, pp. 4415-4422, Oct. 2016.

[7] Y. H. Ko, Y. J. Kim, H. I. Yoo, W. Y. Yang, and Y. S. Cho, “2-D DoA Estimation with Cell Searching for a Mobile Relay Station with Uniform Circular Array”, *IEEE Transactions on Communications*, vol. 58, no. 10, pp. 2805-2809, Oct. 2010.

[8] J. C. Liberti and T. S. Rappaport, “A geometrically based model for line-of-sight multipath radio channels”, in *Proceedings of Vehicular Technology Conference*, vol. 2, pp. 844-848, 1996.

[9] F. Shang, “Parameter estimation algorithms for impulse radio UWB localization systems”, Dissertations McGill University, 2013.

[10] L. Wan, G. Han, L. Shu, S. Chan, and T. Zhu, “The Application of DOA Estimation Approach in Patient Tracking Systems with High Patient Density”, *IEEE Transactions on Industrial Informatics*, vol. 12, no. 6, pp. 2353-2364, Dec. 2016.

[11] H. Lehpamer, *Microwave Transmission Networks*, 2nd edition. New York: McGraw-Hill Education, 2010.

[12] A. F. Molisch, *Wireless Communications*, 2nd edition. Chichester, West Sussex, U.K: Wiley, 2010.

[13] A. S. Narayanan and S. K. Saha, *Waves and Oscillations in Nature: An Introduction*. CRC Press, 2015.

[14] H. Krim and M. Viberg, “Two decades of array signal processing research: the parametric approach,” *Signal Processing Magazine, IEEE*, vol. 13, no. 4, pp. 67âĂŞ94, 1996.

[15] M. S. Babtlett, “Smoothing Periodograms from Time-Series with Continuous Spectra,” *Nature*, vol. 161, no. 4096, pp. 686âĂŞ687, May 1948.

[16] J. Capon, “High-resolution frequency-wavenumber spectrum analysis,” *Proceedings of the IEEE*, vol. 57, no. 8, pp. 1408âĂŞ1418, Aug. 1969.

[17] R. O. Schmidt, “Multiple emitter location and signal parameter estimation,” *IEEE Transactions on Antennas and Propagation*, vol. 34, no. 3, pp. 276âĂŞ280, Mar. 1986.

[18] A. Barabell, “Improving the resolution performance of eigenstructure-based direction-finding algorithms,” in *Acoustics, Speech, and Signal*

Processing, IEEE International Conference on ICASSP '83., 1983, vol. 8, pp. 336âĂŞ339.

[19] S. V. Schell, R. A. Calabretta, W. A. Gardner, and B. G. Agee, "Cyclic MUSIC algorithms for signal-selective direction estimation," in , *1989 International Conference on Acoustics, Speech, and Signal Processing, 1989. ICASSP-89*, 1989, pp. 2278âĂŞ2281 vol.4.

[20] R. Roy and T. Kailath, "ESPRIT-estimation of signal parameters via rotational invariance techniques," *IEEE Transactions on Acoustics, Speech and Signal Processing*, vol. 37, no. 7, pp. 984âĂŞ995, Jul. 1989.

[21] B. Ottersten, M. Viberg, and T. Kailath, "Performance analysis of the total least squares ESPRIT algorithm," *IEEE Transactions on Signal Processing*, vol. 39, no. 5, pp. 1122âĂŞ1135, May 1991.

[22] L. C. Godara, "Limitations and capabilities of directions-of-arrival estimation techniques using an array of antennas: a mobile communications perspective," in *Phased Array Systems and Technology, 1996., IEEE International Symposium on*, 1996, pp. 327âĂŞ333.

[23] M. Wax and T. Kailath, "Optimum localization of multiple sources by passive arrays," *IEEE Transactions on Acoustics, Speech and Signal Processing*, vol. 31, no. 5, pp. 1210âĂŞ1217, Oct. 1983.

[24] K.-C. Ho, K.-C. Tan, and B. T. G. Tan, "Linear dependence of steering vectors associated with tripole arrays," *IEEE Transactions on Antennas and Propagation*, vol. 46, no. 11, pp. 1705-1711, Nov. 1998.

[25] T. Ratnarajah, "An H^∞ approach to multi-source tracking," in *IEEE International Conference on Acoustics, Speech and Signal Processing*, vol. 4, pp. 2205-2208, 1998.

[26] E. L. Afraimovich, V. V. Chernukhov, V. A. Kobzar, and K. S. Palamartchouk, "Determining polarization parameters and angles of arrival of HF radio signals using three mutually orthogonal antennas," *Radio Science*, vol. 34, no. 5, pp. 1217-1225, Sep. 1999.

[27] E. N. Onggosanusi, B. D. V. Veen, and A. M. Sayeed, "Space-time polarization signaling for wireless communications," in *IEEE Sensor Array and Multichannel Signal Processing Workshop*, pp. 188-192, 2000.

[28] K. T. Wong, "Direction finding / polarization estimation — dipole and/or loop triad(s)," *IEEE Transactions on Aerospace and Electronic Systems*, vol. 37, no. 2, pp. 679-684, April 2001.

[29] Y. Xu and Z. Liu, "Adaptive Quasi-Cross-Product Algorithm for Uni-Tripole Tracking of Moving Source," *International Conference on Communication Technology*, pp. 1-4, 2006.

[30] S. Appadwedula and C. M. Keller, "Direction-Finding Results for a Vector Sensor Antenna on a Small UAV," *IEEE Sensor Array and Multichannel Signal Processing Workshop*, pp. 74-78, 2006.

[31] D. Li, Z. Feng, J. She and Y. Cheng, "Unique Steering Vector Design of Cross-Dipole Array with Two Pairs," *Electronic Letters*, vol. 43, no. 15, pp. 796-797, 19th July 2007.

[32] C.-Y. Chiu, J.-B. Yan and R. D. Murch, "Compact Three-Port Orthogonally Polarized MIMO Antennas," *IEEE Antennas and Wireless Propagation Letter*, vol. 6, pp. 619- 622, 2007.

[33] N. Honma, R. Kudo, K. Nishimori, Y. Takatori, A. Ohta and S. Kubota, "Antenna Selection Method for Terminal Antennas Employing Orthogonal Polarizations and Patterns in Outdoor Multiuser MIMO System," *IEICE Transactions on Communications*, vol. E91-B, no. 6, pp. 1752-1759, June 2008.

[34] X. Zhang, Y. Shi and D. Xu, "Novel Blind Joint Direction of Arrival and Polarization Estimation for Polarization-Sensitive Uniform Circular Array," *Progress In Electromagnetics Research*, vol. 86, pp. 19-37, 2008.

[35] Y. Xu, Z. Liu and S. Fu, "Polarimetric Smoothing Revisited: Applicability to Randomly Polarized Sources and to Incomplete Electromag-

netic Vector-Sensors," *International Conference on Signal Processing*, pp. 328-331, 2008.

[36] S. H. Zainud-Deen, H. A. Malhat, K. H. Awadalla and E. S. El-Hadad, "Direction of Arrival and State of Polarization Estimation Using Radial Basis Function Neural Network (RBFNN)," *National Radio Science Conference*, pp. B10-1 to B10-8, 2008.

[37] J. He and Z. Liu, "Computationally Efficient 2D Direction Finding and Polarization Estimation with Arbitrarily Spaced Electromagnetic Vector Sensors at Unknown Locations Using the Propagator Method," *Digital Signal Processing*, vol. 19, no. 3, pp. 491-503, May 2009.

[38] X. Gong, Z.-W. Liu, Y.-G. Xu and M. I. Ahmad, "Direction-of-Arrival Estimation via Twofold Mode-Projection," *Signal Processing*, vol. 89, no. 5, pp. 831-842, May 2009.

[39] X. Gao, X. Zhang, Z. Sun, W. Chen and Y. Shi, "On Multilinear-based Approaches of Blind Receiver for Polarization Sensitive Uniform Square Array", *International Conference on Wireless Networks and Information Systems*, pp. 338-342, 2009.

[40] L. K. S. Daldorff, D. S. Turaga, O. Verscheure and A. Biem, "Direction of Arrival Estimation Using Single Tripole Radio Antenna," *IEEE International Conference on Acoustics, Speech and Signal Processing*, pp. 2149-2152, 2009.

[41] X. Gong, Z.-W. Liu and Y.-G. Xu, "Direction Finding via Biquaternion Matrix Diagonalization with Vector-Sensors," *Signal Processing*, vol. 91, no. 4, pp. 821-831, April 2011.

[42] Y. Huang, G. Friedman and A. Nehorai, "Balancing Magnetic and Electric Responses of Vector-Sensing Antenna," *IEEE Antennas and Propagation Society International Symposium*, vol. 4, pp. 212-215, 2001.

[43] C. K. Au Yeung and K. T. Wong, "CRB: Sinusoid-Sources' Estimation using Collocated Dipoles/Loops," *IEEE Transactions on Aerospace and Electronic Systems*, vol. 45, no. 1, pp. 94-109, January 2009.

[44] G. Sinclair, “The transmission and reception of elliptically polarized waves,” *Proceedings of the I. R. E.*, vol. 38, no. 2, pp. 148-151, February 1950.

[45] J. Li and R. T. Compton, Jr., “Angle and polarization estimation using ESPRIT with a polarization sensitive array,” *IEEE Transactions on Antennas and Propagation*, vol. 39, no. 9, pp. 1376-1383, September 1991.

[46] R. C. Johnson, Editor, *Antenna Engineering Handbook*, Third Edition, New York, U.S.A.: McGraw-Hill, Inc., 1993.

[47] J. Li, “Direction and polarization estimation using arrays with small loops and short dipoles,” *IEEE Transactions on Antennas and Propagation*, vol. 41, no. 3, pp. 379-387, March 1993.

[48] A. Belouchrani, K. Abed-Meraim, J.-F. Cardoso and E. Moulines, “A blind source separation technique based on second order statistics,” *IEEE Transactions on Signal Processing*, vol. 45, no. 2, pp. 434-444, February 1997.

[49] K. T. Wong and M. D. Zoltowski, “Uni-vector-sensor ESPRIT for multi-source azimuth, elevation, and polarization estimation,” *IEEE Transactions on Antennas and Propagation*, vol. 45, no. 10, pp. 1467-1474, October 1997.

[50] T. Svantesson, “The effects of mutual coupling using a linear array of thin dipoles of finite length,” *IEEE Workshop on Statistical Signal and Array Processing*, pp. 232-235, 1998.

[51] T. Svantesson, “Modeling and estimation of mutual coupling in a uniform linear array of dipoles,” *IEEE International Conference on Acoustics, Speech, and Signal Processing*, vol. 5, pp. 2961-2964, 1999.

[52] K. T. Wong and M. D. Zoltowski, “Closed-form direction-finding with arbitrarily spaced electromagnetic vector-sensors at unknown locations,” *IEEE Transactions on Antennas and Propagation*, vol. 48, no. 5, pp. 671-681, May 2000.

[53] M. D. Zoltowski and K. T. Wong, "ESPRIT-based 2D direction finding with a sparse array of electromagnetic vector-sensors," *IEEE Transactions on Signal Processing*, vol. 48, no. 8, pp. 2195-2204, August 2000.

[54] M. D. Zoltowski and K. T. Wong, "Closed-form eigenstructure-based direction finding using Arbitrary but Identical subarrays on a sparse uniform rectangular array grid," *IEEE Transactions on Signal Processing*, vol. 48, no. 8, pp. 2205-2210, August 2000.

[55] K. T. Wong and M. D. Zoltowski, "Self-initiating MUSIC direction finding and polarization estimation in spatio-polarizational beamspace," *IEEE Transactions on Antennas and Propagation*, vol. 48, no. 8, pp. 1235-1245, August 2000.

[56] T. Svantesson, " Mutual coupling compensation using subspace fitting," *IEEE Sensor Array and Multichannel Signal Processing Workshop*, pp. 494-498, 2000.

[57] H. L. Van Trees, *Detection, Estimation, and Modulation Theory, Part IV: Optimum Array Processing*, New York, U.S.A.: Wiley, 2002.

[58] J. Lundback and S. Nordebo, "On polarization estimation using tripole arrays," *IEEE Antennas and Propagation Society International Symposium*, vol. 1, pp. 65-68, 2003.

[59] J Lundback and S. Nordebo, "Analysis of a tripole array for polarization and direction of arrival estimation," *IEEE Sensor Array and Multichannel Signal Processing Workshop*, pp. 284-288, 2004.

[60] C. A. Balanis, *Antenna Theory: Analysis and Design*, Hoboken, New Jersey, U.S.A.: Wiley-Interscience, 3rd edition, 2005.

[61] B. K. Lau and J. B. Andersen, "Direction-of-arrival estimation for closely coupled arrays with impedance matching," *International Conference on Information, Communications Signal Processing*, 2007.

[62] X. Yuan, K. T. Wong, Z. Xu and K. Agrawal, "Various triad compositions of collocated dipoles/loops, for direction finding and polariza-

tion estimation," *IEEE Sensors Journal*, vol. 12, no. 6, pp. 1763-1771, June 2012.

[63] M. Abramowitz and I. A. Stegun, *Handbook of Mathematical Functions: With Formulas, Graphs, and Mathematical Tables*, Courier Corporation, 1964.

[64] R. C. Johnson, *Antenna Engineering Handbook*, McGraw-Hill Professional, 1992.

[65] J. Li, "Direction and polarization estimation using arrays with small loops and short dipoles," *IEEE Transactions on Antennas and Propagation*, vol. 41, no. 3, pp. 379-387, 1993.

[66] H. L. Van Trees, *Detection, Estimation, and Modulation Theory, Part IV: Optimum Array Processing*, New York, U.S.A.: Wiley, 2002.

[67] J. C. Whitaker, *The RF Transmission Systems Handbook*, CRC Press, 2002.

[68] C. A. Balanis, *Antenna Theory: Analysis and Design*, Hoboken, New Jersey, U.S.A.: Wiley-Interscience, 3rd edition, 2005.

[69] F.-J. Chen, S. Kwong, and C.-W. Kok, "Two-dimensional angle and polarization estimation using ESPRIT without pairing," *IEEE International Symposium on Circuits and Systems*, pp. 1063-1066, 2006.

[70] K. E. Lonngren, S. V. Savov, and R. J. Jost, *Fundamentals of Electromagnetics with MATLAB*. SciTech Publishing, 2007.

[71] M. Golio and J. Golio, *RF and Microwave Passive and Active Technologies*, CRC Press, 2007.

[72] C. K. Au Yeung and K. T. Wong, "CRB: Sinusoid-Sources' Estimation using Collocated Dipoles/Loops," *IEEE Transactions on Aerospace and Electronic Systems*, vol. 45, no. 1, pp. 94-109, January 2009.

[73] D. M. Kitavi, K. T. Wong, M. Zou, and K. Agrawal, "A lower bound of the estimation error of an emitter's direction-of-arrival / polarization,

for a collocated triad of orthogonal dipoles/loops that fail randomly," accepted to appear in *IET Microwaves, Antennas & Propagation*.

[74] B. Shrestha, A. Elsherbeni, and L. Ukkonen, "UHF RFID reader antenna for near-field and far-field operations", *IEEE Antennas and Wireless Propagation Letters*, vol. 10, pp. 1274-1277, 2011.

[75] X. Qing, C. K. Goh, and Z. N. Chen, "Segmented loop antenna for UHF near-field RFID applications", *Electronics Letters*, vol. 45, no. 17, pp. 872-873, 2009.

[76] M. Mark, T. BjÃűrninen, L. Ukkonen, L. SydÃďnheimo, and J. M. Rabaey, "SAR reduction and link optimization for mm-size remotely powered wireless implants using segmented loop antennas", in *IEEE Topical Conference on Biomedical Wireless Technologies, Networks, and Sensing Systems*, pp. 7-10, 2011.

[77] D. Foster, "Loop antennas with uniform current", *Proceedings of the IRE*, vol. 32, no. 10, pp. 603-607, 1944.

[78] Z. N. Chen, C. K. Goh, and X. Qing, "Loop antenna for UHF near-field RFID reader", *Proceedings of the Fourth European Conference on Antennas and Propagation*, 2010.

[79] J. Shi, X. Qing, Z. N. Chen, and C. K. Goh, "Electrically large dual-loop antenna for UHF near-field RFID reader", *IEEE Transactions on Antennas and Propagation*, vol. 61, no. 3, pp. 1019-1025, Mar. 2013.

[80] Y. S. Ong, X. Qing, C. K. Goh, and Z. N. Chen, "A segmented loop antenna for UHF near-field RFID", *IEEE Antennas and Propagation Society International Symposium*, 2010.

[81] D. G. Fang, *Antenna Theory and Microstrip Antennas*, Beijing, China: Science Press, 2011.

[82] R. Boyer, "Analysis of the COLD uniform linear array", *IEEE Workshop on Signal Processing Advances in Wireless Communications*, pp. 563-567, 2009.

[83] R. Boyer, “Analysis of the COLD uniform linear array,” *IEEE 10th Workshop on Signal Processing Advances in Wireless Communications*, pp. 563-567, 2009.

[84] L. Sun, C. Li, Y. Lu, and G. Ou, “Distributed vector sensor cross product added with MUSIC for direction of arrival estimation,” *Asia-Pacific International Symposium on Electromagnetic Compatibility*, pp. 1354-1357, 2010.

[85] M. N. El Korso, R. Boyer, A. Renaux, and S. Marcos, “Statistical resolution limit: Application to passive polarized source localization,” *Detection, Architecture and Technology Workshop*, 2011

[86] M. N. El Korso, R. Boyer, A. Renaux, and S. Marcos, “Statistical resolution limit of the uniform linear cocentered orthogonal loop and dipole array,” *IEEE Transactions on Signal Processing*, vol. 59, no. 1, pp. 425-431, January 2011.

[87] D. T. Vu, A. Renaux, R. Boyer, and S. Marcos, “Weiss-Weinstein bound and SNR threshold analysis for DOA estimation with a cold array,” *IEEE Statistical Signal Processing Workshop* , pp. 13-16, 2011.

[88] W. L. Stutzman and G. A. Thiele, *Antenna Theory and Design*, John Wiley and Sons, 2012.

[89] H. J. Kramer, *Observation of the Earth and Its Environment: Survey of Missions and Sensors*. Springer Science and Business Media, 2012.

[90] X. Jin and M. Ali, “A novel 3D cubic loop antenna with nearly isotropic pattern,” *Microwave and Optical Technology Letters*, vol. 56, no. 7, pp. 1511-1513, July 2014.

[91] E. W. Weisstein, ‘Bessel Function Zeros’. [Online]. Available: http://mathworld.wolfram.com/BesselFunctionZeros.html. [Accessed: 31-Aug-2016].

[92] X. Yuan, K. T. Wong, and K. Agrawal, “Polarization estimation with a dipole-dipole pair, a dipole-loop pair, or a loop-loop pair of various

orientations”, *IEEE Transactions on Antennas and Propagation*, vol. 60, no. 5, pp. 2442-2452, May 2012.

[93] D. M. Kitavi, K. T. Wong, M. Zou & K. Agrawal, “A lower bound of the estimation error of an emitter’s direction-of-arrival / polarization, for a collocated triad of orthogonal dipoles/loops that fail randomly," *IET Microwaves, Antennas & Propagation*, vol. 11, no. 7, pp. 961-970, June 2017.

[94] F. T. Ulaby & C. Elachi, *Radar Polarimetry for Geoscience Applications*, Boston, U.S.A.: Artech House Publishers, 1990.

[95] S. R. Best & A. D. Yaghjian, “The lower bounds on Q for lossy electric and magnetic dipole antennas," *IEEE Antennas and Wireless Propagation Letters*, vol. 3, no. 1, pp. 314-316, December 2004.

[96] A. Nehorai & E. Paldi, “Vector-sensor array processing for electromagnetic source localization," *IEEE Transactions on Signal Processing*, vol. 42, no. 2, pp. 376-398, February 1994.

[97] K. T. Wong, Y. Song, C. J. Fulton, S. Khan, and W. Y. Tam, “Electrically “Long” Dipoles in a Collocated/Orthogonal Triad – for Direction Finding and Polarization Estimation,” *IEEE Transactions on Antennas and Propagation*, vol. 65, no. 11, pp. 6057-6067, Nov. 2017.

[98] M. Abramowitz and I. A. Stegun, *Handbook of Mathematical Functions: With Formulas, Graphs, and Mathematical Tables*, North Chelmsford, Massachusetts, U.S.A.: Courier Corporation, 1964.

[99] A. M. Elbir, “Direction finding in the presence of direction-dependent mutual coupling,” *IEEE Antennas and Wireless Propagation Letters*, vol. 16, pp. 1541-1544, 2017.

[100] M. Wu, J. Huang, X. Zhang, and N. Yuan, “Direction finding of coherent non-circular signals for conformal array using geometric algebra,” *IET Microwaves, Antennas & Propagation*, vol. 11, no. 10, pp. 1456-1461, Aug. 2017.

[101] J. He, Z. Zhang, T. Shu, and W. Yu, “Direction finding of multiple partially polarized signals with a nested cross-dipole array,” *IEEE Antennas and Wireless Propagation Letters*, vol. 16, pp. 1679-1682, 2017.

[102] J. Zhao and H. Tao, “Quaternion based joint DOA and polarization parameters estimation with stretched three-component electromagnetic vector sensor array,” *Journal of Systems Engineering and Electronics*, vol. 28, no. 1, pp. 1-9, Feb. 2017.

[103] X. Yu, M. Liang, and H. Xin, “Performance evaluation of wideband microwave direction-of-arrival estimation using Luneburg lens,” *IEEE Antennas and Wireless Propagation Letters*, vol. 16, pp. 2453-2456, 2017.

[104] P. Rocca, M. A. Hannan, M. Salucci, and A. Massa, “Single-snapshot DoA estimation in array antennas with mutual coupling through a multiscaling BCS strategy,” *IEEE Transactions on Antennas and Propagation*, vol. 65, no. 6, pp. 3203-3213, Jun. 2017.

[105] M. Akcakaya, C. H. Muravchik, and A. Nehorai, “Biologically Inspired Coupled Antenna Array for Direction-of-Arrival Estimation,” *IEEE Transactions on Signal Processing*, vol. 59, no. 10, pp. 4795-4808, Oct. 2011.

[106] M. Lin and L. Yang, “Blind Calibration and DOA Estimation With Uniform Circular Arrays in the Presence of Mutual Coupling,” *IEEE Antennas and Wireless Propagation Letters*, vol. 5, pp. 315-318, 2006.

[107] T. Meng, M. Wu, and N. Yuan, “DOA Estimation of Noncircular Signals Using Quaternions,” *International Journal of Antennas and Propagation*, vol. 2017, pp. 1-6, 2017.

[108] G. Byun, H. Choo, and H. Ling, “Optimum Placement of DF Antenna Elements for Accurate DOA Estimation in a Harsh Platform Environment,” *IEEE Transactions on Antennas and Propagation*, vol. 61, no. 9, pp. 4783-4791, Sep. 2013.

[109] R. Goossens, H. Rogier, and S. Werbrouck, “UCA Root-MUSIC With Sparse Uniform Circular Arrays,” *IEEE Transactions on Signal Processing*, vol. 56, no. 8, pp. 4095-4099, Aug. 2008.

[110] P. Ioannides and C. A. Balanis, “Uniform circular arrays for smart antennas,” *IEEE Antennas and propagation magazine*, vol. 47, no. 4, pp. 192-206, 2005.

[111] T. Su, K. Dandekar, and H. Ling, “Simulation of mutual coupling effect in circular arrays for direction-finding applications,” *Microw. Opt. Technol. Lett.*, vol. 26, pp. 331-336, Sep. 2000.

[112] M. Sato and T. Takayama, “A Novel Directional Borehole Radar System Using Optical Electric Field Sensors,” *IEEE Transactions on Geoscience and Remote Sensing*, vol. 45, no. 8, pp. 2529-2535, Aug. 2007.

[113] K. H. Sadeghi and M. Emadi, “Coupling compensation for unmatched circular arrays in high-frequency applications,” *IET Radar, Sonar & Navigation*, vol. 6, no. 8, pp. 774-780, Oct. 2012.

[114] S. Akkar, F. Harabi, and A. Gharsallah, “Directions of arrival estimation with planar antenna arrays in the presence of mutual coupling,” *International Journal of Electronics*, vol. 100, no. 6, pp. 818-836, Jun. 2013.

[115] T. Aksoy and T. E. Tuncer, “Measurement reduction for mutual coupling calibration in DOA estimation,” *Radio Science*, vol. 47, no. 3, p. n/a-n/a, Jun. 2012.

[116] T. Aksoy and T. Engin Tuncer, “Sectorized approach and measurement reduction for mutual coupling calibration of non-omnidirectional antenna arrays,” *Radio Science*, vol. 48, no. 2, pp. 102-110, Mar. 2013.

[117] Z. Huang and C. A. Balanis, “The MMSE Algorithm and Mutual Coupling for Adaptive Arrays,” *IEEE Transactions on Antennas and Propagation*, vol. 56, no. 5, pp. 1292-1296, May 2008.

[118] W. Du, D. Su, S. Xie, and H. T. Hui, "A fast calculation method for the receiving mutual impedances of uniform circular arrays," *IEEE Antennas and Wireless Propagation Letters*, vol. 11, pp. 893-896, 2012.

[119] R. Goossens and H. Rogier, "A hybrid UCA-RARE/Root-MUSIC approach for 2-D direction of arrival estimation in uniform circular arrays in the presence of mutual coupling," *IEEE Transactions on Antennas and Propagation*, vol. 55, no. 3, pp. 841-849, Mar. 2007.

[120] E. Kornaros, S. Kabiri, and F. De Flaviis, "A novel model for direction finding and phase center with practical considerations," *IEEE Transactions on Antennas and Propagation*, vol. 65, no. 10, pp. 5475-5491, Oct. 2017.

[121] H. Rogier and E. Bonek, "Analytical spherical-mode-based compensation of mutual coupling in uniform circular arrays for direction-of-arrival estimation," *AEU - International Journal of Electronics and Communications*, vol. 60, no. 3, pp. 179-189, Mar. 2006.

[122] S. Liu, L. Yang, S. Yang, Q. Jiang, and H. Wu, "Blind direction-of-arrival estimation with uniform circular array in presence of mutual coupling," *International Journal of Antennas and Propagation*, vol. 2016, pp. 1-7, 2016.

[123] B. R. Jackson, S. Rajan, B. J. Liao, and S. Wang, "Direction of arrival estimation using directive antennas in uniform circular arrays," *IEEE Transactions on Antennas and Propagation*, vol. 63, no. 2, pp. 736-747, Feb. 2015.

[124] V. Inghelbrecht, J. Verhaevert, T. Van Hecke, H. Rogier, M. Moeneclaey, and H. Bruneel, "Stochastic framework for evaluating the effect of displaced antenna elements on DOA estimation," *IEEE Antennas and Wireless Propagation Letters*, vol. 16, pp. 262-265, 2017.

[125] X. Yuan, K. T. Wong, and K. Agrawal, "Polarization estimation with a dipole-dipole pair, a dipole-loop pair, or a loop-loop pair of various

orientations," *IEEE Transactions on Antennas and Propagation*, vol. 60, no. 5, pp. 2442-2452, May 2012.

[126] J. Li and R. T. Compton, "Angle and polarization estimation using ESPRIT with a polarization sensitive array," *IEEE Transactions on Antennas and Propagation*, vol. 39, no. 9, pp. 1376-1383, Sep. 1991.

[127] J. Li and R. T. Compton, "Angle estimation using a polarization sensitive array," *IEEE Transactions on Antennas and Propagation*, vol. 39, no. 10, pp. 1539-1543, Oct. 1991.

[128] J. Li and R. T. Compton, "Two-dimensional angle and polarization estimation using the ESPRIT algorithm," *IEEE Transactions on Antennas and Propagation*, vol. 40, no. 5, pp. 550-555, May 1992.

[129] J. Li and R. T. Compton, "Angle and polarization estimation in a coherent signal environment," *IEEE Transactions on Aerospace and Electronic Systems*, vol. 29, no. 3, pp. 706-716, Jul. 1993.

[130] J. Li and P. Stoica, "Efficient parameter estimation of partially polarized electromagnetic waves," *IEEE Transactions on Signal Processing*, vol. 42, no. 11, pp. 3114-3125, Nov. 1994.

[131] Q. Cheng and Y. Hua, "Performance analysis of the MUSIC and Pencil-MUSIC algorithms for diversely polarized array," *IEEE Transactions on Signal Processing*, vol. 42, no. 11, pp. 3150-3165, Nov. 1994.

[132] Q. Cheng and Y. Hua, "Further study of the Pencil-MUSIC algorithm," *IEEE Transactions on Aerospace and Electronic Systems*, vol. 32, no. 1, pp. 284-299, Jan. 1996.

[133] J. E. F. del Rio and M. F. Catedra-Perez, "The matrix pencil method for two-dimensional direction of arrival estimation employing an L-shaped array," *IEEE Transactions on Antennas and Propagation*, vol. 45, no. 11, pp. 1693-1694, Nov. 1997.

[134] J. E. F. del Rio and M. F. Catedra, "Efficient Configurations of the Matrix Pencil with Data Provided by Two Orthogonal Linear Arrays

of Electrically Small Dipoles," *Digital Signal Processing*, vol. 8, no. 2, pp. 103-113, Apr. 1998.

[135] P. Chevalier and A. Ferreol, "On the virtual array concept for the fourth-order direction finding problem," *IEEE Transactions on Signal Processing*, vol. 47, no. 9, pp. 2592-2595, Sep. 1999.

[136] X. Wang and T. Chen, "Performance analysis for joint estimation of frequency, 2D AOA and polarization under array error," in *IEEE International Conference on Communications, Circuits and Systems and West Sino Expositions*, 2002, vol. 2, pp. 1021-1024.

[137] X. Zhenhai, W. Xuesong, X. Shunping, and Z. Zhaowen, "Joint spectrum estimation of polarization and space," in *International Conference on Neural Networks and Signal Processing*, 2003, vol. 2, pp. 1285-1289.

[138] B. A. Obeidat, Y. Zhang, and M. G. Amin, "Range and DOA estimation of polarized near-field signals using fourth-order statistics," in *IEEE International Conference on Acoustics, Speech, and Signal Processing*, 2004, vol. 2, p. ii-97-100.

[139] Y. Wu, H. C. So, C. Hou, and J. Li, "Passive localization of near-field sources with a polarization sensitive array," *IEEE Transactions on Antennas and Propagation*, vol. 55, no. 8, pp. 2402-2408, Aug. 2007.

[140] Y. Shi and X. Zhang, "Quadrilinear decomposition-based blind signal detection for polarization sensitive uniform square array," *Progress In Electromagnetics Research*, vol. 87, pp. 263-278, 2008.

[141] Y. Xu, Z. Liu, and S. Fu, "Polarimetric smoothing revisited: Applicability to randomly polarized sources and to incomplete electromagnetic vector-sensors," in *9th International Conference on Signal Processing*, 2008, pp. 328-331.

[142] L. Shuai, Q. Xiaolin, and J. Ming, "Joint polarization-DOA estimation using sparse antenna array," in *9th International Conference on Signal Processing*, 2008, pp. 353-357.

[143] X. Gong, Y. Xu, and Z. Liu, “Quaternion ESPRIT for direction finding with a polarization sensitive array,” in *9th International Conference on Signal Processing*, 2008, pp. 378-381.

[144] X. Gong, Z. Liu, Y. Xu, and M. Ishtiaq Ahmad, “Direction-of-arrival estimation via twofold mode-projection,” *Signal Processing*, vol. 89, no. 5, pp. 831-842, May 2009.

[145] J. Liang, D. Liu, and J. Zhang, “Joint frequency, 2-D DOA, and polarization estimation using parallel factor analysis,” *Sci. China Ser. F-Inf. Sci.*, vol. 52, no. 10, pp. 1891-1904, Oct. 2009.

[146] W. Li-Guo, W. Ke, and S. Xiao-Ying, “Joint estimation method of azimuth, elevation, range and polarization for near field sources based on MP algorithm,” *J. Jilin Univ. (Eng. Technol. Edition)*, vol. 40, no. 3, pp. 842-847, May 2010.

[147] L. Wang and K. Wang, “A joint estimation method of azimuth, elevation, range and polarization for near field sources without pairing parameters,” in *International Conference on Computer, Mechatronics, Control and Electronic Engineering*, 2010, vol. 3, pp. 325-328.

[148] H. Jiang, D.-F. Wang, and C. Liu, “Estimation of DOD and 2D-DOA and polarizations for bistatic MIMO radar,” in *The 19th Annual Wireless and Optical Communications Conference (WOCC 2010)*, 2010, pp. 1-5.

[149] A. Manikas and J. W. P. Ng, “Crossed-dipole arrays for asynchronous DS-CDMA systems,” *IEEE Transactions on Antennas and Propagation*, vol. 52, no. 1, pp. 122-131, Jan. 2004.

[150] Y. Ravinder and V. M. Pandharipande, “Real valued minimum mean square error approach for polarization diversity adaptive arrays,” in *Proc. Asia-Pacific Conf. Applied Electromagn.*, 2007.

[151] S. H. Zainud-Deen, H. A. Malhat, K. H. Awadalla, and E. S. El-Hadad, “Direction of arrival and state of polarization estimation using Radial Basis Function Neural Network (RBFNN),” in *National Radio Science Conference*, 2008, pp. 1-8.

[152] V. Dehghanian, J. Nielsen, and G. Lachapelle, “Merger of polarization and spatial diversity by moving a pair of orthogonally polarized dipoles,” in *Canadian Conference on Electrical and Computer Engineering*, 2010, pp. 1-6.

[153] R. Goossens and H. Rogier, “2-D direction of arrival estimation combining UCA-RARE and MUSIC for uniform circular arrays subject to mutual coupling,” *Proceedings of the Joint 9th International Conference on Electromagnetics in Advanced Applications and the 11th European Electromagnetic Structures Conference*, 2005, pp. 791-794.

[154] R. Goossens and H. Rogier, “2-d direction-of-arrival estimation in the presence of mutual coupling by exploiting the symmetry in a uniform circular array,” *IEEE Antennas and Propagation Society International Symposium*, 2007, pp. 5283-5286.

[155] J. Xie, Z. He, H. Li, and J. Li, “2D DOA estimation with sparse uniform circular arrays in the presence of mutual coupling,” *EURASIP Journal on Advances in Signal Processing*, vol. 2011, no. 1, p. 127, 2011.

[156] J. Xie, Z.-S. He, and H.-Y. Li, “A fast DOA estimation algorithm for uniform circular arrays in the presence of unknown mutual coupling,” *Progress In Electromagnetics Research C*, vol. 21, pp. 257-271, 2011.

[157] G.-J. Jiang, X.-P. Mao, and Y.-T. Liu, “Decoupled 2d DOA estimation with a small number of elements in UCAs,” *CIE International Conference on Radar*, 2016, pp. 1-4.

[158] H. Gazzah, “Direction finding antenna arrays with improved accuracy and reduced complexity and size,” *Sensor Signal Processing for Defence*, pp. 1-5, 2016.

[159] B. Friedlander and A. J. Weiss, “Direction finding in the presence of mutual coupling,” *IEEE Transactions on Antennas and Propagation*, vol. 39, no. 3, pp. 273-284, 1991.

[160] M. Pesavento and J. F. Bohme, “Direction of arrival estimation in uniform circular arrays composed of directional elements,” *Sensor*

Array and Multichannel Signal Processing Workshop Proceedings, 2002, pp. 503-507.

[161] H. Gazzah, J. P. Delmas, and S. M. J. Larsys, “Direction-finding arrays of directional sensors for randomly located sources,” *IEEE Transactions on Aerospace and Electronic Systems*, vol. 52, no. 4, pp. 1995-2003, Aug. 2016.

[162] C. Chang, T. Cheng, and H. Lin, “Fast direction finding algorithm for circular array based on directional antenna,” *International Workshop on Microwave and Millimeter Wave Circuits and System Technology*, 2012, pp. 1-4.

[163] B. Liao, K.-M. Tsui, and S.-C. Chan, “Frequency invariant uniform concentric circular arrays with directional elements,” *IEEE Transactions on Aerospace and Electronic Systems*, vol. 49, no. 2, pp. 871-884, 2013.

[164] K.-H. Chen and J.-F. Kiang, “Highly accurate direction-of-arrival estimation with a uniform circular array,” *International Symposium on Antennas and Propagation*, 2014, pp. 371-372.

[165] A. N. Lemma, A.-J. Van der Veen, and E. F. Deprettere, “Multiresolution ESPRIT algorithm,” *IEEE Transactions on Signal Processing*, vol. 47, no. 6, pp. 1722-1726, 1999.

[166] H. Gazzah and J. P. Delmas, “On isotropic circular arrays of anisotropic sensors,” *IEEE Signal Processing and Information Technology International Symposium*, 2015, pp. 95-99.

[167] F. E. D. Raimondi and P. Comon, “Tensor DoA estimation with directional elements,” *IEEE Signal Processing Letters*, vol. 24, no. 5, pp. 648-652, 2017.

[168] B. K. Lau, Yee, Y. Liu, and K. L. Teo, “Transformations for nonideal uniform circular arrays operating in correlated signal environments,” *IEEE Transactions on Signal Processing*, vol. 54, no. 1, pp. 34-48, Jan. 2006.

[169] R. Goossens, H. Rogier, and S. Werbrouck, “UCA Root-MUSIC with sparse uniform circular arrays,” *IEEE Transactions on Signal Processing*, vol. 56, no. 8, pp. 4095-4099, Aug. 2008.